

**OPTOELECTRONIC DEVICE SIMULATION:  
OPTICAL MODELING FOR SEMICONDUCTOR OPTICAL  
AMPLIFIERS AND SOLID STATE LIGHTING**

A Dissertation  
Presented to  
The Academic Faculty

by

Dong-Xue (Michael) Wang

In Partial Fulfillment  
of the Requirements for the Degree  
Doctor of Philosophy in the  
School of Electrical & Computer Engineering

Georgia Institute of Technology  
May 2006

Copyright 2006 by Dongxue (Michael) Wang

**OPTOELECTRONIC DEVICE SIMULATION:  
OPTICAL MODELING FOR SEMICONDUCTOR OPTICAL  
AMPLIFIERS AND SOLID STATE LIGHTING**

Approved by:

Dr. Ian T. Ferguson, Advisor  
School of Electrical & Computer Engineering  
*Georgia Institute of Technology*

Dr. Christopher Summers  
School of Electrical & Computer Engineering  
*Georgia Institute of Technology*

Dr. John A. Buck, Co-Advisor  
School of Electrical & Computer Engineering  
*Georgia Institute of Technology*

Dr. Gee-Kung Chang  
School of Electrical & Computer Engineering  
*Georgia Institute of Technology*

Dr. W. Russell Callen Jr.  
School of Electrical & Computer Engineering  
*Georgia Institute of Technology*

Dr. Vikram Krishnamurthy  
Chief Technology Officer  
VT Silicon, Inc.  
Atlanta, GA 30308

Date Approved: April 10, 2006

In memory of my grandmother  
Zengxian Cui,  
In memory of my father  
Guifen Wang,

Dedicated to my mother  
Fenghua Wang.

## ACKNOWLEDGEMENTS

I would like to thank my dissertation advisors, Professor Ian T. Ferguson and Professor John A. Buck for their guidance and support during my graduate studies. I have always been grateful for their valuable advice and insight. I would not have finished this thesis without their support and encouragement. I owe a debt of gratitude to my former advisor, Professor Kevin F. Brennan, who first brought me to Georgia Tech, for his financial and spiritual support. I would also like to thank Professor Callen and Professor Summers, for their service on my dissertation reading committee.

I must thank my grandmother, Zengxian Cui for her great love and endless patience. She educated me in a unique way during my childhood. This early education has been valuable to my entire life. I highly appreciate my parents, Guifen Wang and Fenghua Wang, my brothers, Zhenxue Wang, Kexue Wang, my sisters, Ruiying Wang, Yueshuang Wang, for their love and support. Without guidance and encouragement from them, I would not have gone through the international journey of my graduate study. I would like to thank my wife, Ye Guan, for her endless support and patience during the past seven years. I also cherish the happy atmosphere that my two sets of twins, a five-year-old and a six-month-old, have brought to my family. The late night cries from my little twins always accompany me to write my thesis.

# TABLE OF CONTENTS

ACKNOWLEDGEMENTS	iv
LIST OF TABLES	vii
LIST OF FIGURES	viii
SUMMARY	xi
<b>CHAPTER 1 Introduction to Semiconductor Amplifiers</b>	<b>1</b>
1.1 Optical Amplifiers for Optical Communications	1
1.2 Fiber Amplifiers: EDFA and Raman Amplifier	1
1.3 Semiconductor Optical Amplifier	3
<b>CHAPTER 2 Theory of Semiconductor Optical amplifiers</b>	<b>14</b>
2.1 Theory of Semiconductor Optical Amplifiers	14
2.2 Numerical Modeling for SOAs	26
2.3 Simplified Analytical Solution to SOA	31
<b>CHAPTER 3 Wavelength Conversion Through Cross-Gain Modulation in Semiconductor Optical Amplifiers</b>	<b>36</b>
3.1 Introduction	36
3.2 Different Gain Coefficient Models	37
3.3 Steady State Numerical Model for SOA Based Wavelength Converters	39
3.4 Numerical Solution Using the Finite Difference Method in Spatial Domain	43
3.5 Conclusions	57
<b>CHAPTER 4 High Brightness LED and Solid State Lighting</b>	<b>59</b>
4.1 Introduction to Solid State Lighting	59

4.2 High Brightness LED Design and Fabrication	60
<b>CHAPTER 5 Theory of Optical Modeling for High Brightness LEDs</b>	<b>64</b>
5.1 Introduction to Optical Modeling	64
5.2 Theory of Optical Ray Tracing	66
5.3 Optical Modeling Based on Electronics Dipole Emissions	71
<b>CHAPTER 6 Optical Modeling for High Brightness LED</b>	<b>80</b>
6.1 Introduction	80
6.2 Guided Wave Approach on LED Modeling	80
6.3 Improve Light Extraction Using a Back Reflector and Thick Substrates	87
6.4 Optimizing LED Die Geometries to Increase Light Extraction Efficiency	88
6.5 Utilizing Reflection Grating to Increase Light Extraction Efficiency	90
<b>CHAPTER 7 Optical Modeling for a Dual Wavelength LED</b>	<b>94</b>
7.1 Dual Wavelength LED Device Structure	94
7.2 Overview of Tunnel Tunction for GaN Based LEDs	98
7.3 Distributed Bragg Reflection Grating for High Brightness LED	100
7.4 Optical Simulations for A Dual Wavelength LED	107
7.5 Summary	119
<b>CHAPTER 8 Conclusions and Future Work</b>	<b>121</b>
8.1 Semiconductor Optical Amplifiers and Wavelength Converters	121
8.2 High Brightness LED and Solid State Lighting	122
8.3 Future Work and new trends	123
8.4 Publications and Patents Based on This Research Work	125
REFERENCES	127

## LIST OF TABLES

Table 1: Large signal gain comparison for long and short SOA wavelength converters	48
Table 2: Light extraction efficiency (LEE) for different die shapes of LEDs	90
Table 3: Refractive indices of GaN, InGaN and AlGaN for simulations	110
Table 4: Refractive indices and absorption coefficients for optical simulations	118

## LIST OF FIGURES

Figure 2.1: Sketch of an SOA	20
Figure 2.2: Sub-section j of an SOA in numerical simulations	27
Figure 2.3: Gain plot for an SOA	28
Figure 2.4: Signal and noise output for different input powers	29
Figure 2.5: Signal gain versus inputs	29
Figure 2.6: Signal gain versus bias current	30
Figure 2.7: Optical spectrum of the SOA output for both signal and ASE	31
Figure 3.1: Gain coefficient plots versus wavelengths	39
Figure 3.2: Schematics of an SOA wavelength converter	40
Figure 3.3: Large signal simulation results for the long SOA up converter: (a) pump power (line) and probe power (dot), (b) carrier density (line) and internal loss (dot)	44
Figure 3.4: Large signal simulation results for the long SOA down converter: (a) pump power (line) and probe power (dot), (b) carrier density (line) and internal loss (dot)	45
Figure 3.5: Large signal simulation results for the short SOA up converter: (a) pump power (line) and probe power (dot), (b) carrier density (line) and internal loss (dot)	46
Figure 3.6: Large signal simulation results for the short SOA down converter: (a) pump power (line) and probe power (dot), (b) carrier density (line) and internal loss (dot)	47
Figure 3.7: Small signal simulation results for the long SOA converter: (a) pump power (line) and probe power (dot) for up conversion at 6GHz modulation (b) pump power (line) and probe power (dot) for down conversion at 5GHz modulation	49
Figure 3.8: Small signal simulation for the short SOA converter at 1GHz modulation: (a) pump power (line) and probe power (dot) for up conversion, (b) pump power (solid) and probe power (dot) for down conversion	50

Figure 3.9: Small signals of carrier density versus different modulation frequency: (a) the Long SOA (b), the Short SOA.	51
Figure 3.10: A Long SOA down converter efficiency comparisons: our modeling results (blue), simulation results (green) and experimental data (red) in Ref.17	53
Figure 3.11: Normalized converter efficiency plots of down-converters, the 1250 $\mu\text{m}$ SOA (solid line), and the 450 $\mu\text{m}$ SOA (circles)	54
Figure 3.12: Down (blue) and Up conversion (green )for the 1250 $\mu\text{m}$ SOA	55
Figure 3.13: Normalized conversion efficiency, down (blue) and Up conversion (green ) for the 1250 $\mu\text{m}$ SOA	55
Figure 3.14: Down (blue) and Up conversion (green ) comparison for the 450 $\mu\text{m}$ SOA	56
Figure 4.1: The GaN LED die structure	61
Figure 4.2: 3-D plot of LED with electrode contacts	62
Figure 5.1: Three levels of optical modeling	65
Figure 5.2: A binary tree of rays	66
Figure 5.3: The propagation direction calculation	67
Figure 5.4: Picture of Ray scattering	69
Figure 5.5: Dipole orientations	72
Figure 5.6: Sketch of multi-layers for transfer matrices	73
Figure 5.7: Diagram of a multi-layer structure	78
Figure 5.8: Light in-plane propagation	79
Figure 6.1: Waveguide structure of a GaN LED	81
Figure 6.2: Geometrical ray tracing of a LED die	87
Figure 6.3: Light forward propagation and backward propagation in a LED	87
Figure 6.4: Decomposition of 3-D wave guide into slab wave guides	89

Figure 6.5: Dimension of square die and rhombus die	89
Figure 6.6: Reflective binary phase grating	91
Figure 6.7: Blazed reflection grating	92
Figure 6.8: LED light coupling: (a) with a back reflector, (b) with a reflection grating	92
Figure 7.1: Structure of a Dual wavelength LED	95
Figure 7.2: A Tunnel junction	96
Figure 7.3: A micro-cavity for a Dual wavelength LED	97
Figure 7.4: Potential barrier for a TJ	98
Figure 7.5: A DBR diagram	102
Figure 7.6: (a) Reflections of AlGaIn/GaN DBR with normal incident light from air (b) Reflections of AlGaIn/GaN DBR with normal incident light from GaN	104
Figure 7.7: Reflections of AlGaIn/GaN DBR with slanted incident light from GaN the Blue curve represents normal incident; the Green curve, 5 degree slanted incident; the Red curve, 10 degree slanted incident	105
Figure 7.8: DBR reflection versus the number of pairs. Red curve represents 20 pairs Green curve, 35 pairs ; Blue curve, 50 pairs	106
Figure 7.9: Reflection plot for an AlN/GaN DBR	106
Figure 7.10: Optical spectrum plot for a dual wavelength LED	107
Figure 7.11: Refractive index plots (a) GaN (b) Al <sub>0.3</sub> Ga <sub>0.7</sub> N and (c) In <sub>0.1</sub> Ga <sub>0.9</sub> N	109
Figure 7.12: Level 2 ray split of optical ray tracing	111
Figure 7.13: Light extraction efficiency collection configuration	112
Figure 7.14: 3-D diagram of a dual wavelength LED	113
Figure 7.15: 2-D plot of ray tracing diagram	113
Figure 7.16: Top LED Light extraction efficiency versus the refractive index variation of InGaIn active region	114

Figure 7.17: Top LED Light extraction efficiency versus the absorption coefficient of InGaN active region	114
Figure 7.18: Bottom LED Light extraction efficiency versus the refractive index variation of InGaN active region	116
Figure 7.19: Bottom LED Light extraction efficiency versus the absorption coefficient of its InGaN active region	116
Figure 7.20: Optical spectrum for 400/460 nm emissions	117

## SUMMARY

Recent advances in optoelectronic devices require sophisticated optical simulation and modeling. These tiny semiconductor device structures, such as semiconductor lasers and light emitting diodes (LED), not only need detailed electrical computation, such as band structure, carrier transportation, and electron-hole recombination under different external voltages, but also require comprehensive optical modeling, such as photon generation and propagation.

Optical modeling also includes waveguide structure calculations, guided mode and leakage mode identification, as well far-field pattern prediction using optical ray tracing. In modeling semiconductor lasers, light emission and propagation can be treated using the single mode of wave optics, the so-called photon propagation equation coupled with carrier transport equations. These differential equations can be numerically solved using the Finite Difference Method (FDM). In the LED modeling, the main tools are based on optical ray tracing, and photons are treated as light emissions with random directions and polarizations. Optical waveguide theory is used to qualitatively analyze photon emissions inside a LED chip, and helps to design the LED device structure.

One important area of semiconductor laser modeling is the optical simulation of the wavelength converter based on semiconductor optical amplifiers (SOA). This wavelength converter is a critical device in optical communication, and it can copy information from one wavelength to another through cross-gain modulation. Some numerical methods have been developed to model the wavelength conversion. In these methods, solutions are found by solving differential equations in the time domain using FDM. In all previous models, the waveguide internal loss is assumed uniform across the cavity of the SOA, or the gain coefficient is based on the polynomial approximation method, i.e., the gain coefficient is assumed proportional to the difference between the carrier and transparency carrier densities; the differential gain is assumed constant accordingly. This assumption is only valid for wavelengths close to the gain peak wavelength. As a result, high accuracy for wideband wavelength conversion is not guaranteed. We proposed a steady state numerical model of wavelength converters based

on cross-gain modulation in semiconductor optical amplifiers. In this model, a new model of the gain coefficient developed by Connelly was applied, which also includes the internal loss variation with the electron carrier density. Each physical variable, such as the carrier density, gain coefficient, differential gain, and internal loss, spatially varies across the SOA cavity and is numerically calculated throughout the device. This model can predict wavelength-dependent characteristics of a wavelength converter of the SOA in both large and small signal regimes. Some key performance factors of SOA wavelength converters, such as selection of pump and probe wavelengths and power, length of SOA cavities, conversion efficiency and bandwidth, system performance difference between up and down conversions can be modeled and optimized using this numerical model.

Most LED modeling techniques are based on optical ray tracing to predict the light extraction efficiency, and the light extraction efficiency is a critical parameter to evaluate LEDs. Here, we proposed a hybrid method to simulate the lighting efficiency of LED chips, where both guided wave theory and geometric optical ray tracing are applied. Guided wave optics is used to identify guided modes and leakage modes inside the LED active layer, and its device structure can be optimized to increase leakage modes so that the lighting extraction efficiency is improved. On the other hand, Monte Carlo optical ray tracing is used to quantitatively determine optical extraction efficiency. Moreover, this method can model the light distribution and far-field illumination pattern. Both single wavelength LEDs and dual-wavelength LEDs can be simulated using our method.

Based on our research work, we proposed several solutions to improve the light extraction efficiency of LEDs and solid state lighting. A back reflector at the bottom of the LED substrate was first applied. The back reflector method does improve the light extraction efficiency; however, the reflected light will undergo re-absorption at the active region and at the p-contact of the LED. The reflection grating with the blazing effect was proposed to overcome this problem. The diffraction effect can shift the majority of light into higher orders, which will be coupled out of the LED sidewalls without re-entering the LED structure. The light extraction efficiency can be increased accordingly. Different kinds of LED die shapes can be optimized using our method. Accordingly, the die shape with maximum lighting extraction efficiency can be identified

# CHAPTER 1

## INTRODUCTION TO SEMICONDUCTOR OPTICAL AMPLIFIER

### 1.1 Optical Amplifiers for Optical Communications

Amplifiers play an important role in the long haul optical communication. Use of electrical amplifier needs the conversion of optical (O) to electrical (E) signal, and back optical signal again. This O to E and E to O dual process add an extra technical complexity and more noise in overall optical communication links. It is difficult to apply to Wavelength Division Multiplexing (WDM) technology because the E to O process can not keep the wavelength information, and this information can not be recovered in the E-O conversion following the O-E process. Optical amplifiers offer the advantages of direct optical to optical amplification without E-O/O-E conversion. Recently, tremendous progresses have been made in the developments of optical amplifiers [1]. The commercialization of Erbium doped fiber amplifiers at early ninety is the main driving force to advance optical communications. The success of EDFA plays vital roles in long haul optical communications.

### 1.2 Fiber Amplifier: EDFA and Raman Amplifier

The most popular optical amplifier has been an Erbium Doped fiber amplifier (EDFA)[2]. EDFAs typically operate in a saturation mode at the 1.55 $\mu$ m window because it has low saturation power, in the order of hundreds of microwatts. It is long lifetime of Er ion at its metastable level, which is about 10ms, that causes the lower saturation power. This lifetime time is quite long compared to the signal bit period in optical communication. As a result, the gain of EDFA is determined by the average power of signal and its immunity to inter symbol noise and interchannel cross talk in optical

communication system using WDM. Other advantage of EDFA is its low Noise figure (NF), which is defined as the ratio of SNR of input signal to the SNR of amplified output signal. A NF below 5 dB is routinely achievable, which is close to its quantum limit of 3dB.

Depending on different applications, EDFAs can be designed to operate in various modes, such as, constant gain mode, constant output power mode by programming their 980 nm or 1480 nm optical pump power [3]. There two problems inherent to EDFA. The first problem is uneven gain across its optical amplification bandwidth. This uneven gain characteristic of EDFA causes a severe problem in WDM application, and more power is given to channels at and close to the gain peak wavelength. This problem becomes even worse when several stages of EDFAs are cascaded in an optical communication link. One approach to solve this problem is a gain flatten filter. The gain flatten filter can be designed using a fiber Bragg grating or thin film technology. In general, a dual-stage EDFA configuration is applied; the gain flatten filter is inserted between the two stages. The first stage is pump by a 980 nm laser diode, and the second one by 1480 nm pump. The gain can be flattened with 1dB across 1530-1560 nm wavelengths. In the meantime, a NF can be controlled within 5dB. The second problem associated to an EDFA is its narrow optical amplification bandwidth, about 50 nm only. This bandwidth is much smaller than the bandwidth of the optical fiber. This type of bandwidth limits the number of WDM channels about 20.

Raman Amplifier offers some advantages for fiber optics communication system with its large optical amplification bandwidth. No special amplification medium other than standard single mode fiber is needed. In Raman amplification, a photon is scattered to create an optical phonon and a lower frequency photon, a Stoke photon. Optical gain is achieved at the Stokes frequency. The gain peak can be tuned by changing the pump wavelength. The distributed Raman amplification also provides high gain and low noise figure. To properly model Raman amplifier, several physical mechanism need to be taken

into account, including spontaneous Raman amplification, stimulated Raman amplification and Rayleigh scattering. To ensure large flattened amplification bandwidth, multiple high power pumps with different pump wavelengths are required[4].

### **1.3 Semiconductor Optical Amplifier**

Semiconductor Optical amplifiers (SOA) with low cost and compactness offer a good solution to optical amplifications in some applications. The SOA is simply a semiconductor laser with antireflection-coated facets in its cavity, in which a traveling signal wave is amplified. The structure of the semiconductor optical amplifier is almost identical to that of the semiconductor laser except for a special designed cavity with polarization-independent gain and antireflection (AR) coated facets. Among its main advantages are low cost and photonic integration with most optoelectronic components, and large amplification bandwidth. The bandwidth of InGaAsP-based SOAs extends from 1.2 to 1.6  $\mu\text{m}$ . The amplification bandwidth of SOAs is quite large, compared to only a 40 nm amplification bandwidth from regular EDFAs [1].

The problem with an SOAs is the short lifetime of its electron carriers, about several hundreds of pico-seconds. This short lifetime causes several nonlinear effects in SOA applications: cross gain modulation (XGM). Other nonlinear effects include cross phase modulation (XPM) and four-wave mixing (FWM), which will cause interchannel cross-talk and intersymbol interference (ISI). A strong signal at one wavelength will modulate the gain for another wavelength because the short lifetime of carriers make the gain response fast. This is physics behind XGM. Some techniques have been developed to minimize the ISI in WDM systems [2]. On the other hand, the nonlinearity of SOAs can be applied to many other areas, such as, wavelength conversions, and optical switch. For example, the XGM is very useful for SOA-based wavelength converters, where the modulated information from one optical wavelength can be copied into another one.

Wavelength conversion can improve traffic controls of wavelength routers in optical communications [1-2].

### 1.3.1 Optical Amplification

In this section, linear application of an SOA to a single wavelength system is first considered, followed by its linear application in WDM systems. Applications of SOAs for both cases in an optical multi-Gigabit system have been demonstrated [5]

An SOA amplifying a single wavelength can be used as an optical gain compensator to recover the loss from coupling, splitting or add-drop module. In general, the unsaturated gain of an SOA is about 20-30 dB, and the corresponding output power is between 5 to 10 dBm. The input power of the SOA should be below -15dBm to avoid an SOA saturation [6]. An SOA can also perform optical amplifications as an optical preamplifier. An SOA is positioned right before a receiver, such as a pin diode (with sensitivity about -15dBm), or an APD (with sensitivity about -25dBm) to improve the signal quality. An optical filter is generally used to between this optical amplifier and receiver to filter out parts of amplified spontaneous emission (ASE) outside the spectrum of optical signal. The noise figure (NF) is used to characterize a preamplifier, which is defined as:

$$NF = \frac{(SNR)_{in}}{(SNR)_{out}} \quad (1.1)$$

If assuming the input SNR is shot noise limited, the NF can be described as [3]:

$$NF = 2n_{sp} \frac{G-1}{G} + \frac{1}{G} = \frac{P_{ASE}}{h\nu\Delta\nu} + \frac{1}{G} \quad (1.2)$$

where  $n_{sp}$  is an inversion factor of an SOA,  $P_{ASE}$  is the power of ASE,  $h\nu$  is energy of photon,  $\Delta\nu$  represents spectrum of ASE;  $G$  is the gain of an SOA. The gain of an SOA used as a preamplifier is about 20dB, and its corresponding NF is about 7dB. Since an SOA can be integrated with other photonic devices, the preamplifier module with an SOA has the size advantage over other solutions, such as an EDFA. Special cares are needed to achieve better system performance. The SOA should be operated away from saturation state because signal pulse shape/waveform may be distorted by a saturated SOA. Saturation power of SOAs is around 10dBm with a gain of 20dB. To avoid saturation of SOA, the input power to an SOA should be below -15dBm. For an SOA with a 20dB gain, the output power for an input with -25dBm is -5dBm, which is far away from the saturation point, and well above the detector sensitivity of -15dBm. For this single wavelength system, crosstalk is not a problem. In general, an optical filter following the SOA is used to minimize the noise from amplified spontaneous emissions (ASE), and the bandwidth of this filter is about 10nm.

Because an SOA general have large saturation power of 10dBm, it is possible to use an SOA to do the job of optical inline amplifier. Since inline amplifiers usually handle relative large optical input signals, the noise at an output end is mainly determined by signal-spontaneous beat noise. Accordingly, the SNR at the output end of an amplifier is given by [3]:

$$SNR = \frac{S}{Noise_{s-sp}} = \frac{GP_{in}}{4h\nu N_{sp} (BW)_E (G-1)} \quad (1.3)$$

For a large gain, this SNR is only affected by input power and the inversion factor of an SOA. This indicates that large input and inversion factor are preferred. For an SOA, the typical value of the inversion factor is about 1.5. A large input will saturate the SOA. For example, an input of -10dBm can easily saturate the SOA. As a result, the inline SOA

should be at a reasonable distance away from the transmitter end of the system. For a optical link, with 0dBm power of a transmitter, and a optical fiber with attenuation of 0.25dB/Km. The SOA should be placed more than 5km away from the transmitter to avoid saturation.

Other possible application of SOA could be a power amplifier, or booster amplifier, which amplifies the optical power directly from a transmitter. A power amplifier can tolerant relative high noise figure. The noise figure of SOAs can meet power amplifier requirement. In general, the power from a transmitter is on the order of -10dBm to 0dBm. Such high power can transmit signal to long distance, or split the signal into multiple channels. This high input power will saturate an SOA quite easily. Also, XGM and other nonlinear problems become more severe with high power applications. Without help of some special techniques, an SOA is not a good candidate in power applications.

The optical switch is another application area of SOAs. The switch application takes advantage of electrical pump property of an SOA and its fast response time. When driven by a high current, An SOA amplifies light. With a low drive current, the SOA absorbs light. By increasing or decreasing the driving current of an SOA, the SOA can be programmed as a switch with a fast response, which can be integrated with other photonic devices.

To operate an SOA in WDM systems, more cares should be taken to avoid crosstalks among multiple wavelengths. Similar to the single wavelength case, An SOA can be used as either a preamplifier or an inline amplifier. For inline amplifier applications, there is trade-off between SNR and XGM induced crosstalks. As we see in a single wavelength application, the SNR is mainly determined by the input power and an inversion factor; The higher the input power, the better the SNR. Without special care, this high input power definitely saturates the SOA, and causes XGM. As a result, XGM induces interchannel cross talk and intersymbol interference (ISI). Another problem from

an SOA in WDM systems is its unflattened gain across different wavelength, so called a gain tilt. This gain tilt problem can be solved by increasing input power.

One approach to reduce XGM is operating an SOA in a low saturation mode to balance bit error rate (BER) and waveform distortion, and meet overall system performance [6]. For an SOA operated in a regular or deep saturation mode, there are two methods to reduce XGM[7-8]. One approach is to add a cw beam with a medium power, so called a reservoir to saturate an SOA. By doing so, the effective gain on modulated signals is reduced, which reduces interchannel XGM. The second approach is two utilizing intensity modulated beams. These two beams are also complemented each other so that they are equivalent to a single cw beam.

### **1.3.2 Optical Nonlinearity and Wavelength Conversion**

The short carrier lifetime of an SOA is responsible for cross gain modulation (XGM), which is unique to an SOA. In addition to XGM, other optical nonlinear effects common to optical communications include cross phase modulation (XPM) and four wave mixing (FWM). Here we briefly go over XPM and FWM, and mainly focus on XGM and its applications

In general, the refractive index of optical medium is dependent upon optical beam intensity. The origin of XPM is the refractive index of one optical wavelength in an SOA is not only affected by its own intensity but also by the intensity of other wavelengths propagation through this SOA. This intensity dependence of the refractive index introduce nonlinear phase shift. This XPM in an SOA can be used in interferometer based wavelength converters, where modulated information is transferred from one wavelength to another. XMP working with a Mach-Zehnder interferometer can demonstrate some characteristics of optical switches. FWM generates new additional optical frequencies from two original optical frequencies. Both XGM and XPM contribute FWM because a

phase-match condition is critical for FWM. If FWM occurs inside an SOA, this SOA will generate an idler optical frequency, which is the beat between a doubled pump frequency and the signal frequency. This phenomenon can be used to implement wavelength conversion [1].

In XGM, fast intensity variation of an optical beam can modulate the carrier density due to the short lifetime of carriers. The carrier density will change the gain of an SOA. As a result, the intensity modulation of one beam can change the amplification gain of other beams. For a WDM system, XGM from an SOA introduces interchannel crosstalk. This problem become even worse when an SOA is operated in high output power, a saturated mode. As described above XGM induced crosstalk causes lots problems in a linear optical amplification using an SOA. However, this nonlinearity can be applied to wavelength conversions. Assuming two optical beams are launched into an SOA. The first beam is modulated, and the second beam is a continuous wave (cw) beam. The information from the first beam can be complementally copied into the second beam by XGM. The first beam is the pump signal, and the cw beam is called a probe signal. Based on the propagation directions, there are two types of wavelength conversions, co-propagation and counter-propagation. In general, the co-propagation offers a relative large bandwidth, lower noise; however, it requires an optical filter to filter out the original signal. Wavelength converters based on XGM have been experimentally realized up to 40Gb/s [9].

Optical packet switches and wavelength routers are two major areas in optical communications requiring SOA based wavelength converters. WDM based systems put high demands on new technologies of photonic switch development. New types of optical switches will be transparent to optical nodes so that there is no need to convert and process optical signal at a node level. In all optical networks, both payload and headers in a packet should transmit all optically from a source node to a destination node. However, the limitation of optical buffers causes problems for all-optical network developments. A

main issue of optical switch is the so called contention resolution. The contention resolution is caused by two or more packets compete for one output node at the same time. This contention can be solved electronically by electrical buffers. The lack of efficient optical buffers makes it difficult to resolve the contention optically. As an alternative, optical wavelength conversion is an efficient way to handle the contention. The basics behind this method are that packets at a specific wavelength targeted to the same port are converted into different wavelength by optical wavelength converter, such as an SOA wavelength converter based on XGM. To improve the efficiency of utilize wavelength converters, several photonic switch architectures, share per node, share per output link, share per input link have been proposed.

WDM based optical networks include multiple optical fiber links connected through wavelength routers. An end to end optical path is required to be established prior to talks between routers. In general, the same wavelength is dedicated to the entire optical path. Multiple optical paths requests may cause blocks if no free wavelength is available. SOA based wavelength converters can overcome these problems [10].

### **1.3.3 Theoretical Models of SOAs and Wavelength Conversion**

We first begin with models for SOAs. Although an SOA is similar to a semiconductor laser, its mathematical models are different. Semiconductor lasers are generally analyzed using a set of rate equations governing photon and electron densities temporal variations in the laser cavity. Since high reflectivity mirrors are employed in the laser cavity, the photon and electron densities can be considered as constants throughout the laser cavity. However, this is not true for modeling of SOA. In an SOA, the photon and electron densities strongly vary throughout the SOA cavity. These variations are strongly dependent on optical input power and a drive current. As a result, the photon and electron densities inside an SOA need to be modeled as both time and space

dependent variables. Moreover, the photon density is described by a traveling wave equation [11].

There are two types of optical power associated with SOAs: the amplified signal, and amplified spontaneous emissions (ASE) noise. The incoherent ASE is modeled by traveling wave power equations. The optical signal is usually analyzed by a coherent traveling wave amplitude equation when facets of an SOA cavity have finite reflectivity, and by a traveling wave power equation when the SOA end faces are coated with antireflection coatings, i.e., with near zero reflectivity. There are several parameters are critical to the theory of SOAs. The material gain coefficient model, waveguide internal loss, the electron carrier lifetime of spontaneous emissions and the fraction of total spontaneous emissions coupled into the signal and further amplified by an SOA.

The material gain coefficient determines the amplification capability of an optical amplifier. It depends on the density of electron carriers, amplification wavelengths for both signal and ASE. It can be determined by Fermi-Dirac distributions of electrons and holes in the active region of an SOA. The slope of gain verse the carrier density denotes the differential gain of an amplifier. The waveguide internal loss include two components: carrier independent loss and carrier-dependent absorption loss. The former is the intrinsic material loss, and latter results from intervalence band absorption. Both material gain and internal loss change the overall gain of an SOA.

The carrier lifetime is determined by the recombination rate  $R$ , with  $R = R_1N + R_2N^2 + R_3N^3$ , the first two terms represent nonradiative recombination and spontaneous emission; the last term represents Auger recombination. These coefficients are difficult to be determined to a high degree of accuracy. In general, this recombination rate is assumed to be linearly proportional to the carrier density, with  $R = N/\tau$ . The  $\tau$  is the carrier lifetime of spontaneous emissions. This spontaneous carrier lifetime depends on optical power inside an SOA, and is affected by the stimulated emission [12]

The fraction of ASE coupled into the guided modes in an optical amplifier can be estimated from an ideal amplifier [11]. An ideal amplifier has the following characteristics: no gain saturation, which means that the carrier density is independent upon the spatial position of throughout the amplifier; no internal loss and zero facet reflectivity. The quantum limit of noise density from this ideal amplifier is a function of its single pass gain, and wavelengths. On the other hand, this amount of noise can be obtained by solving a traveling power equation for ASE. Accordingly, the fraction of spontaneous emission coupled into the guide modes of the amplifier can be determined from these two equations.

In addition to an amplifier gain, the saturation power of an optical amplifier is an important parameter to evaluate performances of amplifiers. In the saturation state, the carrier density of electrons fails to provide enough electrons required by large input signal which causes carrier depletions. The saturation state of an amplifier is defined when a single pass gain of amplifier is a 3dB below the small signal gain. The density of this saturation power is inversely proportional to a product of the carrier lifetime and the differential gain. Large saturation power is preferred when an SOA is applied to linear amplification. The ASE can be reasonably neglected when an SOA is operated with large saturation power, and some nonlinear phenomena occur when an SOA is driven into deep saturation.

The polarization of the input signal usually influences the gain of an SOA because the confinement factors are different for TE and TM waves. The confinement factor determines how much amplified power is restrained within the active region of the amplifier. This gain polarization dependence can be solved by proper designing the cavity of an SOA. In addition, temperature variations also affect the gain of an SOA. Since the temperature changes Fermi distribution of carriers, high temperature causes a decrease in the gain. In a wavelength of 1.5  $\mu\text{m}$ , a 3dB gain decrease of a 500  $\mu\text{m}$  long SOA is attributed to the temperature decrease by about 5°C. Finally, the residual facet

reflectivity of SOAs decrease the saturation power, and cause gain resonance and ripples. An SOA with nonzero facets reflective can amplify backward signals and spontaneous emission. In general, this reflectivity of faces needs to be less than  $10^{-5}$ [13].

In general, SOA based wavelength converters can be implemented using either XGM, XPM or FWM. XGM based wavelength conversion is simple to implement and widely accepted. We will focus modeling of XGM based wavelength conversions. Several analytical solutions have been reported. All these models use the gain model with polynomial approximations, and the pump and probe wavelengths are indistinguishable in these models [13-15]. Moreover, both carrier densities, internal loss are constant throughout an SOA cavity in some models. These simplifications reduce these traveling wave equations for amplifiers to simple form. As a result, analytical solutions for these simplified equations are obtainable. These methods quantitatively explain the unusual large modulation frequency up to several tens of GHz of signal conversion observed in SOA based wavelength conversion, also the resonance peak of modulation frequency. One method notices that modulation bandwidth does not directly relate to the internal loss of SOAs [14] because a constant gain is assumed in this method. Mecozzi proposed a more accurate method [15], in which the material gain of an SOA is characterized by total optical power traveling through an SOA. Since the total power inside this SOA depends on the spatial position along the SOA cavity, the spatial dependence of the material gain of this SOA is included in this model. It was found out that the frequency response of the XGM of SOA based wavelength converters is strongly dependent on the internal loss of an SOA. A Transfer function approach is also proposed to solve SOA based wavelength conversion [16]. It is shown that the probe channel close to the input end acts as a low-pass filter, characterized by the effective carrier lifetime. The pump channel, however, is a high-pass filter. The interact between the pump and probe signals may cause modulation resonance peak for co-propagation wavelength length converters with a finite internal loss.

There several methods to implement numerical simulations of SOA based wavelength converters [12, 17-19]. In one method, the internal loss of SOAs is included in effective coupling loss. It also used an averaged carrier density to calculate the SOA gain, and a polynomial approximation is used to calculate the gain [12]. The most comprehensive numerical modeling of SOA based wavelength converters has been presented in Ref. 17, in which a matrix method in quantum mechanics is applied to calculate the material gain of SOAs. In all these numerical methods, the internal loss is taken as a constant throughout the SOA. Also, their gain models are either a simple polynomial approximation or complex numerical methods from quantum mechanics.

There are two parallel topics in this dissertation: optical modeling of SOA and SOA based wavelength converters, and optical modeling for LEDs and solid state lighting. In the first part of dissertation, overview of semiconductor optical amplifiers and wavelength converter is first presented, and theory of semiconductor optical amplifiers and optical modeling is followed. Finally, comprehensive numerical simulation of wavelength converters based on semiconductor optical amplifiers is developed. Optical modeling for high brightness LEDs and solid state lighting is studied in the second part of this dissertation.

## **CHAPTER 2**

### **THEORY OF SEMICONDUCTOR OPTICAL AMPLIFIERS**

#### **2.1 Theory of Semiconductor Optical Amplifiers**

First, we present an overview of the system equations for a semiconductor optical amplifier, which include rate equations for electron carriers and traveling equations for photons. Second, material gain coefficients and the spontaneous emission factor are analyzed.

##### **2.1.1 System Equations for Semiconductor Optical Amplifiers**

The theoretical foundation for semiconductor optical amplifiers (SOA) modeling was established in 1980s [11, 21]. Since then major progress on semiconductor optical amplifier modeling focuses on the material gain coefficient, spontaneous emission rate and the fraction of spontaneous emissions coupled into the guided waves in an amplifier. Some numerical simulations using the Finite Difference Method (FDM) have been studied intensively to solve carrier rate equation and photon traveling wave equations. In parallel, some simplified analytical models have been developed with approximations on carrier density, material gain coefficients and spontaneous emissions. In the following sections, theoretical models for SOAs are described, and both numerical solution and simplified analytical solutions are reviewed. Based on Einstein relations between spontaneous emission and stimulated emissions and the noise expression from an ideal amplifier, we have obtained a new expression for the fraction of spontaneous emissions coupled into the guided waves in an amplifier.

In a semiconductor optical amplifier (SOA), both photon and electron densities vary temporally and spatially. The rate equations for photons and electrons not considering spatial variation in modeling a regular laser are no longer valid for modeling

SOAs. Photon distributions are described by a set of traveling equations which are jointly dependent on time and space. Moreover, optical signal and spontaneous emissions are treated differently in modeling of semiconductor optical amplifiers because the phase information of signal beam is required. For a specific wavelength  $\lambda$ , the rate equation of photon due to spontaneous emissions and rate equations for electrons are given by [11]:

$$\frac{dS_\lambda}{dt} = R(N)D_\lambda F + V_g(g_\lambda - \alpha)S_\lambda \quad (2.1)$$

$$\frac{dN}{dt} = \frac{J}{qd} - R(N) - \Gamma V_g \int g_\lambda S_\lambda d\lambda \quad (2.2)$$

The symbol representations are listed as follows:

N: Electron carrier density in the conduction band

$D_\lambda$ : Corresponding electron distribution function for different wavelength

$S_\lambda$ : Photon density at wavelength  $\lambda$  guided into an SOA

J : Current density

d, E , L: Thickness ,width and length of an SOA cavity

q : Electron charge

R: Carrier recombination rate

F: Fraction of spontaneous emissions coupled into guided modes

$g_\lambda$ : Material gain at wavelength  $\lambda$

$\alpha$  : Photon internal loss

$V_g$ : Group velocity

$\Gamma$  : Optical confinement factor

The spontaneous emissions can propagate in both forward, (+z) and backward (-z) directions, so we have

$$S_\lambda = S_\lambda^+ + S_\lambda^- \quad (2.3)$$

A retard frame riding on optical waves from spontaneous emissions is used. So the time derivative of photon density can be obtained

$$\frac{dS_\lambda^+}{dt} = \frac{\partial S_\lambda^+}{\partial t} + V_g \frac{\partial S_\lambda^+}{\partial z} \quad (2.4)$$

$$\frac{dS_\lambda^-}{dt} = \frac{\partial S_\lambda^-}{\partial t} - V_g \frac{\partial S_\lambda^-}{\partial z} \quad (2.5)$$

For steady-state conditions, the following equations of photons are satisfied

$$\frac{dS_\lambda^+}{dz} = \frac{1}{2V_g} R(N)D_\lambda F + (\Gamma g_\lambda - \alpha)S_\lambda^+ \quad (2.6)$$

$$\frac{dS_\lambda^-}{dz} = -\frac{1}{2V_g} R(N)D_\lambda F - (\Gamma g_\lambda - \alpha)S_\lambda^- \quad (2.7)$$

The total spontaneous emissions equally distribute between forward and backward directions. They are traveling wave power equations for spontaneous emissions. The spontaneous carrier lifetime is usually used to determine the carrier recombination rate R

$$R(N) = \frac{N}{\tau} \quad (2.8)$$

Assuming the input end of an SOA at  $z=0$ , and the output end at  $z=L$ . The mirror reflectivity at input has reflectivity  $R_1$ , and the output mirror has reflectivity  $R_2$ .

Boundary conditions for these spontaneous emission traveling power equations are

$$S_{\lambda}^{+}(0) = R_1 S_{\lambda}^{-}(0) \quad (2.9)$$

$$S_{\lambda}^{-}(L) = R_2 S_{\lambda}^{+}(L) \quad (2.10)$$

Gain functions of a single pass gain for forward and backward spontaneous emissions are defined, respectively, as follows:

$$G_{\lambda}^{+}(z) = \exp\left[\int_0^z (\Gamma g_{\lambda} - \alpha) dz\right] \quad (2.11)$$

$$G_{\lambda}^{-}(z) = \exp\left[\int_z^L (\Gamma g_{\lambda} - \alpha) dz\right] \quad (2.12)$$

the single pass gain is given by

$$G_{\lambda} = G_{\lambda}^{+}(L) = G_{\lambda}^{-}(0) \quad (2.13)$$

We also define other two functions related to recombination rates:

$$T_{\lambda}^{+}(z) = \frac{1}{2V_g} D_v F \int_0^z \frac{R(z)}{G_{\lambda}^{+}(z)} dz \quad (2.14)$$

$$T_{\lambda}^{-}(z) = \frac{1}{2V_g} D_v F \int_z^L \frac{R(z)}{G_{\lambda}^{-}(z)} dz \quad (2.15)$$

With the above several defined integral equations, it is easy to get the following solutions for amplified spontaneous emissions (ASE) in both forward and backward directions:

$$S_{\lambda}^{+}(z) = G_{\lambda}^{+}(z)[S_{\lambda}^{+}(0) + T_{\lambda}^{+}(z)] \quad (2.16)$$

$$S_{\lambda}^{-}(z) = G_{\lambda}^{-}(z)[S_{\lambda}^{-}(L) + T_{\lambda}^{-}(z)] \quad (2.17)$$

The initial values of forward and backward spontaneous emissions can be obtained with these boundary conditions of Eqs.(2.9) and (2.10)[11]:

$$S_{\nu}^{+}(0) = \frac{G_{\lambda}R_1}{1 - G_{\lambda}^2R_1R_2} [T_{\lambda}^{+}(L)G_{\lambda}R_2 + T_{\lambda}^{-}(0)] \quad (2.18)$$

$$S_{\nu}^{-}(L) = \frac{G_{\lambda}R_2}{1 - G_{\lambda}^2R_1R_2} [T_{\lambda}^{-}(0)G_{\lambda}R_1 + T_{\lambda}^{+}(L)] \quad (2.19)$$

These integral form solutions to spontaneous emissions are difficult to solve analytically. Numerical simulation results can be obtained using the Finite Difference method (FDM). Under certain approximations, these complex solutions can be simplified to some analytical solutions. Also, these ASE equations are coupled with signal equations and the carrier rate equations through material gain coefficients and the carrier recombination rate. The traveling wave equation for the signal, carrier rate equation and the detailed material gain model will be addressed in the followings.

The treatment of signal wave is different from that of spontaneous emissions. Figure 2.1 shows the schematics of an SOA with finite reflectivity  $R_1$ ,  $R_2$  on its two facets, respectively. The signal wave get partially transmitted and reflected from the two facets of the SOA. As a result, the signal wave is amplified in two directions, forward direction and backward direction, and there are two sets of traveling waves originated from the signal. If  $A_+$  and  $A_-$  denote amplitudes of these forward and backward traveling waves, respectively, we have [22-25]:

$$\frac{dA_{\pm}(z)}{dz} = -jkz + \frac{1}{2}(\Gamma g_{\lambda} - \alpha)A_{\pm}(z) \quad (2.20)$$

$$\frac{dA_-(z)}{dz} = jkz - \frac{1}{2}(\Gamma g_\lambda - \alpha)A_-(z) \quad (2.21)$$

where  $k$  is a propagation constant for this signal wavelength  $\lambda$ :

$$k = \frac{2\pi n}{\lambda} \quad (2.22)$$

and  $n$  is the effective refractive index of the active region of the SOA. These amplified backward and forward signal waves should satisfy the following boundary conditions:

$$A_+(0) = t_1 A_{in} + r_1 A_-(0) \quad (2.23)$$

$$A_-(L) = r_2 A_+(L) \quad (2.24)$$

$$A_{out} = t_2 A_+(L) \quad (2.25)$$

where  $r_1$  and  $r_2$  are amplitude reflection coefficients, and  $t_1$   $t_2$ , the amplitude transmission coefficient assuming both mirrors of an SOA cavity are lossless.  $A_{in}$  is the signal amplitude of at the input of the SOA.  $A_+$  is the amplitude of the forward signal inside the SOA propagates along the positive direction of the  $z$  axis.  $A_-$  represents the amplitude of the backward signal for an SOA cavity with nonzero reflectivity facets. Also a lateral variation of the optical signals inside the SOA cavity is negligible.

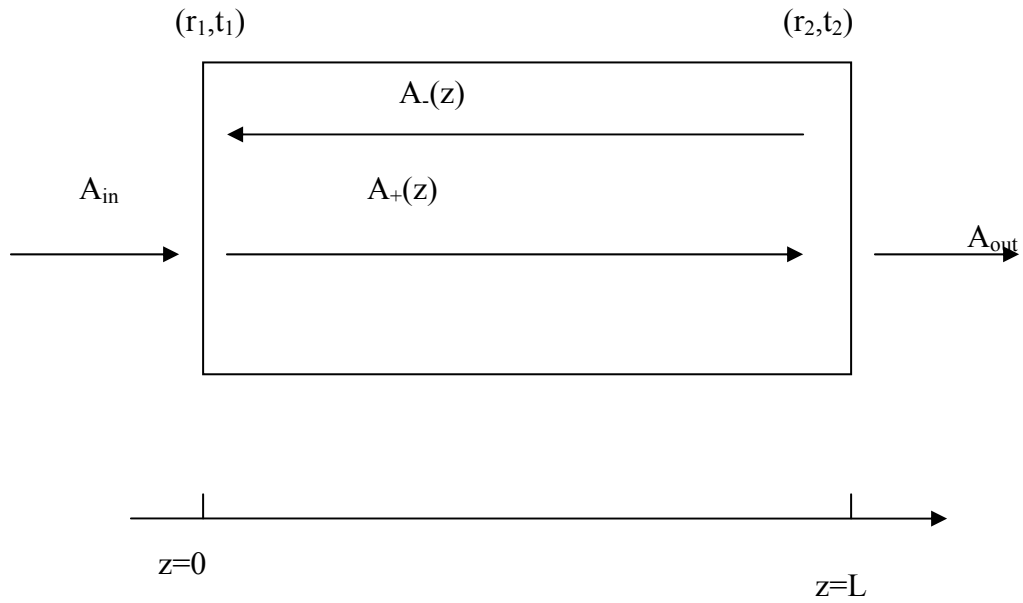


Figure 2.1 Sketch of an SOA

It is easy to prove the following solutions for both forward and backward amplified signals

$$A_+(z) = A_+(0) \sqrt{G_\lambda^+(z)} \exp(-jkz) \quad (2.26)$$

$$A_-(z) = A_-(L) \sqrt{G_\lambda^-(z)} \exp[-jk(L-z)] \quad (2.27)$$

From Equations (2.23-2.24) and (2.27), we have:

$$A_+(0) = \frac{t_1}{1 - r_1 r_2 G_\lambda \exp(-j2kL)} A_{in} \quad (2.28)$$

$$A_-(L) = \frac{\sqrt{G_\lambda} t_1 r_2 \exp(-jkL)}{1 - r_1 r_2 G_\lambda \exp(-j2kL)} A_{in} \quad (2.29)$$

The SOA with mirrors can be considered as a Fabry-Perot (FP) cavity, and the overall power gain of the amplifier from multiple passes of reflections and transmissions can be easily evaluated as:

$$G = \frac{|t_1 t_2|^2 G_\lambda}{|1 - r_1 r_2 G_\lambda \exp(-j2kL)|^2} \quad (2.30)$$

It can also be expressed as:

$$G = \frac{(1 - R_1)(1 - R_2)}{(1 - \sqrt{R_1 R_2} G_\lambda)^2 + 4\sqrt{R_1 R_2} G_\lambda \sin^2 \varphi} G_\lambda \quad (2.31)$$

where  $\varphi = knL$  is the phase delay in a single pass across the cavity. Since we have obtained solutions to both spontaneous emission and signal, it is time to rewrite the steady-state carrier rate equation as:

$$\Gamma V_g \{g_\lambda [|A_+(z)|^2 + |A_-(z)|^2] + \int g_\lambda S_\lambda d\lambda\} + R(N) - \frac{J}{qd} = 0 \quad (2.32)$$

Finally, it is easy to show how the photon density relates to the input and power:

$$P = V_g h\nu |A_{in}|^2 \frac{Ed}{\Gamma} = \gamma |A_{in}|^2 \quad (2.33)$$

The same relation holds for output power. Similarly, spontaneous emissions at the amplifier output, forward emission noise  $N_f$ , and backward emission noise  $N_b$  at the amplifier input, are describe as:

$$N_f(L) = \gamma \sum S_\lambda^+(L) \quad (2.34)$$

$$N_b(L) = \gamma \sum S_\lambda^-(0) \quad (2.35)$$

In these Equations, a discrete summation is used to replace the integral.

### 2.1.2 Material gain coefficients

So far, we still need another piece of information to complete the solution to an semiconductor amplifier: the material gain coefficient. The material gain model is simplified by taking an SOA as an ordinary two-level lasing system, and it is given by [21,26]

$$g_\lambda = \frac{B}{V_g} (D_\lambda N - H_\lambda N_o) \quad (2.36)$$

where B is the stimulated emission factor, N is the electron density in the conduction band, N<sub>o</sub> is the effective carrier density in the valence band; D<sub>λ</sub> and H<sub>λ</sub> are electron distributions in the conduct band and the valence band, respectively. It is well known that the stimulated emission coefficient B and spontaneous emission coefficient A<sub>1</sub> is related by [26]:

$$\frac{A_1}{B} = \left(\frac{2n}{\lambda}\right)^3 \pi \quad (2.37)$$

The spontaneous emission coefficient A<sub>1</sub> can be approximated as 1/τ, and the B can be rewritten as

$$B = \left(\frac{\lambda}{2n}\right)^3 \left(\frac{1}{\pi\tau}\right) \quad (2.38)$$

Finally, the expression of gain coefficients may be given by:

$$g_\lambda = \left(\frac{\lambda}{2n}\right)^3 \left(\frac{1}{\pi v_g \tau}\right) (D_\lambda N - H_\lambda N_o) \quad (2.39)$$

However, the carrier distribution functions  $D_\lambda$  and  $H_\lambda$  still remain unknown. It is the time to determine these two functions. Both  $D_\lambda$  and  $H_\lambda$  are normalized Lorentzian functions.

$$D_\lambda = \frac{1}{1 + (\lambda - \lambda_p)^2 / W_1^2} \frac{\Delta\lambda}{\pi W_1} \quad (2.40)$$

$$H_\lambda = \frac{1}{1 + (\lambda - \lambda_p)^2 / W_2^2} \frac{\Delta\lambda}{\pi W_2} \quad (2.41)$$

where  $\lambda_p$  is the peak wavelength of the carrier distribution functions,  $W_1$  and  $W_2$  are distribution width parameters, and They are two empirical parameters, and  $W_1$  is much smaller than  $W_2$ .  $W_1$  is also a function of another line-width parameter  $W$ , and  $W$  is a line-width parameter in an approximated function of the gain coefficient:

$$g_v = g_{\max} - \left( \frac{\lambda - \lambda_p}{W} \right)^2 \quad (2.42)$$

For small input signal without noise presence, Eq. (2-36) can be approximated:

$$g_v \approx \frac{g_{\max}}{1 + [(\lambda - \lambda_p) / W_1]^2} \approx g_{\max} \left[ 1 - \left( \frac{\lambda - \lambda_p}{W_1} \right)^2 \right] \quad (2.43)$$

where  $g_{\max}$  is determined by:

$$g_{\max} = \frac{B\tau}{V_g} \frac{J}{qd} \frac{\Delta\lambda}{\pi W_1} \quad (2.44)$$

$W_1$  can be approximated by comparison of Eq. (2.42) and Eq. (2.43):

$$W_1 = W \sqrt{g_{\max}} \quad (2.45)$$

Finally,  $\Delta\lambda$  is the longitudinal mode wavelength interval of the amplifier cavity, which is given by

$$\Delta\lambda = \frac{\lambda^2}{2nL} \quad (2.46)$$

### 2.1.3 Spontaneous emission factor

The last parameter is the spontaneous emission factor  $F$ . It is the ratio of the volume of one guided mode in mode number space of the amplifier cavity to the total volume in mode space of spontaneous emissions. It can be approximately described as [11]:

$$F = \frac{\Gamma \lambda_p^2}{4\pi n^2 E d} \quad (2.47)$$

Another way to determine this spontaneous emission factor is to use noise expression from an ideal amplifier. Noise from this ideal linear amplifier can be calculated using quantum mechanical methods [27], which is given by:

$$N_{\min} = (G - 1)h\nu\Delta\nu = (G - 1) \frac{hc^2}{\lambda^3} \Delta\lambda \quad (2.48)$$

where  $c$  is the speed of light, and  $G$  is the power gain of the amplifier. If an SOA operated as an ideal amplifier, the requirements are as follows: (1) its gain is always linear independent the input power, which means the carrier density is constant across the

SOA cavity (2) No internal loss, i.e.,  $\alpha=0$ , and  $N_0=0$  in Eq.(2.36). (3) The cavity facets have zero reflectivity, and there is no coupling loss. Under these assumptions, Eq.(2.6) becomes:

$$\frac{dS_{\lambda}^{+}}{dz} = \frac{1}{2V_g\tau} D_{\lambda} FN + \frac{\Gamma B D_{\lambda}}{V_g} NS_{\lambda}^{+} \quad (2.49)$$

At the output end of the SOA, we have

$$S_{\lambda}^{+}(L) = (G - 1) \frac{F}{2\Gamma B\tau} \quad (2.50)$$

Accordingly, the total noise output within  $\Delta\lambda$ , the longitudinal mode wavelength interval of the amplifier cavity, is:

$$N_{amp} = (G - 1)V_g h\nu \frac{FA}{2\Gamma^2 B\tau} = A(G - 1) \frac{hc^2}{2n\lambda} \frac{F}{\Gamma^2 B\tau} \quad (2.51)$$

where  $A=Ed$  is the cross-section area of the cavity. With help of Eqs. (2.51), (2.48), (2.46) and (2.38), we obtain the a new formula for the spontaneous emission factor

$$\frac{F}{B\tau} = \frac{\Gamma^2}{V_a} \quad (2.52)$$

$$F = \frac{\Gamma^2}{\pi V_a} \left( \frac{\lambda}{2n} \right)^3 \quad (2.53)$$

where  $V_a=EdL$  is the volume of the cavity of the SOA. Eqs. (2.47) and (2.52) are used to determine the spontaneous emission and gain coefficient from stimulated emissions.

Also, the final expression of  $W_1$  can be obtained as using Eqs. (2.44), (2.45), (2.47) and (2.52)

$$W_1 = \left( \frac{\lambda^4}{\pi^2 n^2 c W} \frac{J}{qd} \right)^{1/3} \frac{W}{2} \quad (2.54)$$

So far, we have all the parameters required to solve a carrier rate equation and traveling wave equations for the signal and spontaneous emissions. These parameters include the stimulated emission factor for material gain coefficients  $B$ , the spontaneous emission factor  $F$ . The width parameter  $W$  should be determined experimentally. Finally, there is an electron injection efficiency  $\eta$ , associated with the drive current of an amplifier [11]. Some electrons are lost due to Auger recombination, carrier leakage effects and other effects. This electron injection efficiency can be determined experimentally. As a result, the effective drive current should be scaled according to this electron injection efficiency.

Without simplification and approximation, the system equations for an SOA have no analytical solutions. In the following sections, the numerical solution based on the finite difference method (FDM) is first developed. The numerical solution to a traveling wave amplifier i.e., with  $R_1=R_2=0$  is considered. In an unsaturated Fabry-Perot (FP) type amplifier, the carrier density and gain can be assumed to be independent of  $z$  position along an SOA cavity. As a result, an analytical solution to FP type amplifier can be obtained, which is detailed in Section 2.3 for SOAs simplified analytical solutions.

## 2.2 Numerical Modeling of SOAs

To solve the SOA equation numerically, the amplifier is divided into multiple sections as shown in Figure 2.2. With initial conditions, the carrier rate equation and traveling wave equations for signal and spontaneous emission are applied to each of these sections. The carrier density for each section is adjusted based on the initial solution.

Multiple iterations are general required to reach convergence. Detailed operation procedures for this numerical algorithm are listed as follows [25]:

Step 1: Take a specific signal input, set spontaneous emissions as zero, and calculate initial carrier density for the carrier rate equation.

Step 2: Computer gain coefficients using the updated carrier density.

Step 3: Traveling wave equations for signal and spontaneous emissions are evaluated using finite difference methods.

Step 4: The signal and spontaneous emissions results for each section from Step 3 are applied to the carrier rate equation.

Step 5: The carrier density for each section is adjusted by checking the sign of the carrier rate equation. If the sign is plus, the carrier density for each section is increased by a weight. Otherwise, decrease the carrier density.

Step 6: Check the carrier difference from the last iteration. If the differences for all sections are less than a predefined small value, a converged solution is achieved. Otherwise, go back to step 2 start a new iteration.

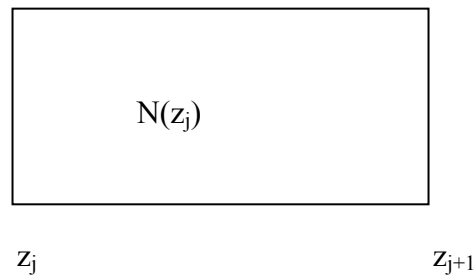


Figure 2.2 Sub-section j of an SOA in numerical simulations

To verify this numerical algorithm, we use this algorithm to solve an amplifier in Reference 11. The following simulation parameters are all from this reference:  $E=15 \mu\text{m}$ ,  $d=0.3 \mu\text{m}$ ,  $L=250 \mu\text{m}$ ,  $R_1=R_2=0$ ,  $\alpha=20 \text{ cm}^{-1}$ ,  $\tau=3 \text{ ns}$ ,  $W=0.18 \mu\text{m}^{3/2}$ ,  $W_2=1 \mu\text{m}$ ,  $n=4$ ,  $\lambda_p=1.3 \mu\text{m}$ ,  $N_0=9.25 \times 10^{18} \text{ cm}^{-3}$ ,  $\Gamma=0.5$ ,  $\eta=0.06$ ,  $J=24 \text{ kA/cm}^2$ ,  $c=3 \times 10^8 \text{ m/s}$

The amplifier cavity was divided into 20 sections. Figure 2.3 shows the amplifier gain and versus input power, and the amplifier start to saturate as the input power reach 0dBm, 1mW. The signal and noise output are plotted in Figure 2.4. These simulated results are in good agreement with published results [11].

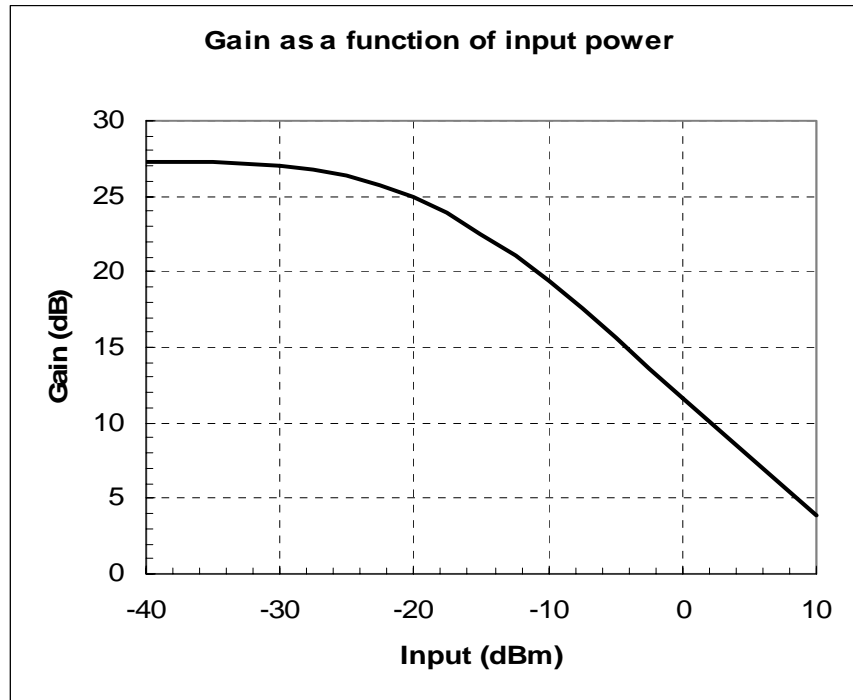


Figure 2.3 Gain plot for an SOA

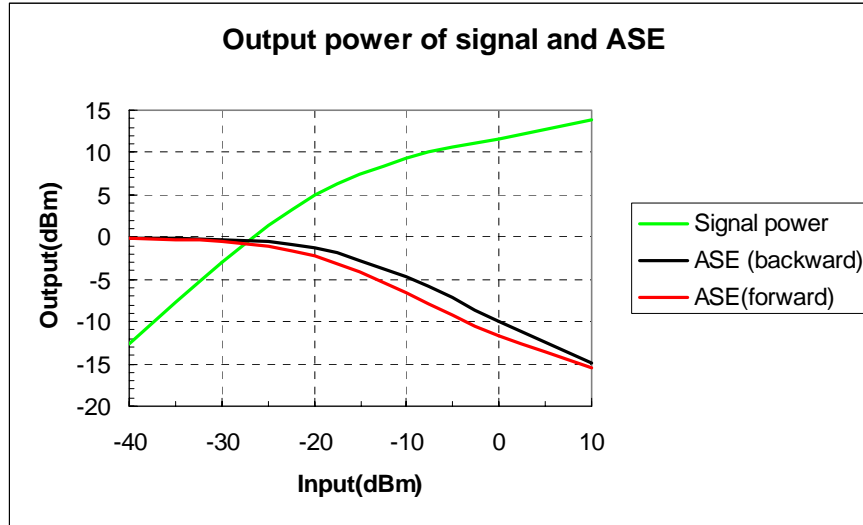


Figure 2.4 Signal and noise output for different input powers

Another simulation example is a 1.55  $\mu\text{m}$  SOA with the following parameters [25]:  $E=0.4 \mu\text{m}$ ,  $d=0.4 \mu\text{m}$ ,  $L=700 \mu\text{m}$ ,  $R_1=R_2=0$ ,  $\alpha=80 \text{ cm}^{-1}$ ,  $\tau=400 \text{ ns}$ ,  $W=0.18 \mu\text{m}^{3/2}$ ,  $W_2=1 \mu\text{m}$ ,  $n=3.22$ ,  $\lambda_p=1.5377 \mu\text{m}$ ,  $N_0=9.25 \times 10^{18} \text{ cm}^{-3}$ ,  $\Gamma=0.45$ ,  $\eta=0.45$ , Drive current  $I=130 \text{ mA}$ ,  $c=3 \times 10^8 \text{ m/s}$ . We first plot the signal gain versus difference input power, and compare these simulated results are shown in Figure 2.5. The saturated output power is about 5 dBm. The signal input power is -25.6 dBm, and the signal wavelength is 1537.7 nm. Our simulation data well fits experimental data as shown in Figure 2.6 [25].

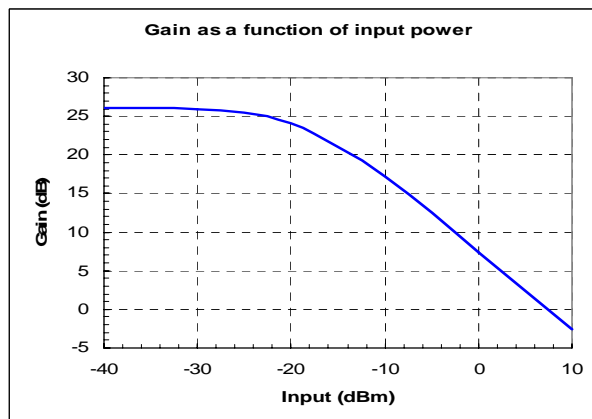


Figure 2.5 Signal gain versus inputs

Next, the simulated gain is plotted as different bias currents, and compared to experimental data with the same signal wavelength and input power. As we can see from Figure 2.6, the threshold bias current for amplification is about 50 mA. Figure 2.7 shows our simulated results for both signal and ASE. The noise figure (NF) can be calculated based on these simulations according to [28]

$$NF = 10 \log_{10} \left[ \frac{\sigma_n(\lambda)}{h\nu G_\lambda} + \frac{\eta_{out}}{G_\lambda} \right] \quad (2.55)$$

where the coupling loss  $\eta_{out}$  is taken as a 3dB. The output power spectrum density of spontaneous emission noise  $\sigma_n(\lambda)$  is given by

$$\sigma_n(\lambda) = \frac{2\gamma S^+(\lambda)}{\Delta\lambda} \quad (2.56)$$

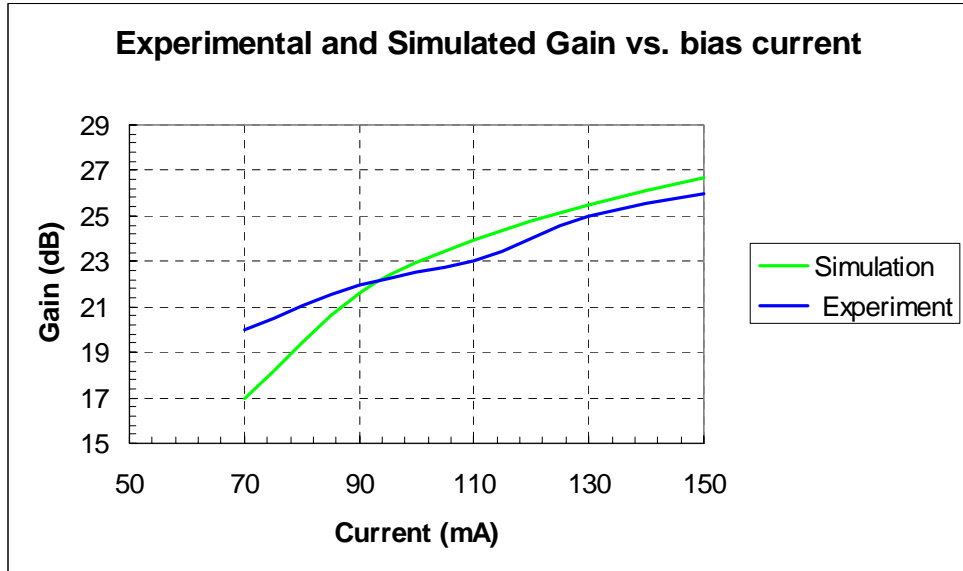


Figure 2.6 Signal gain versus bias current

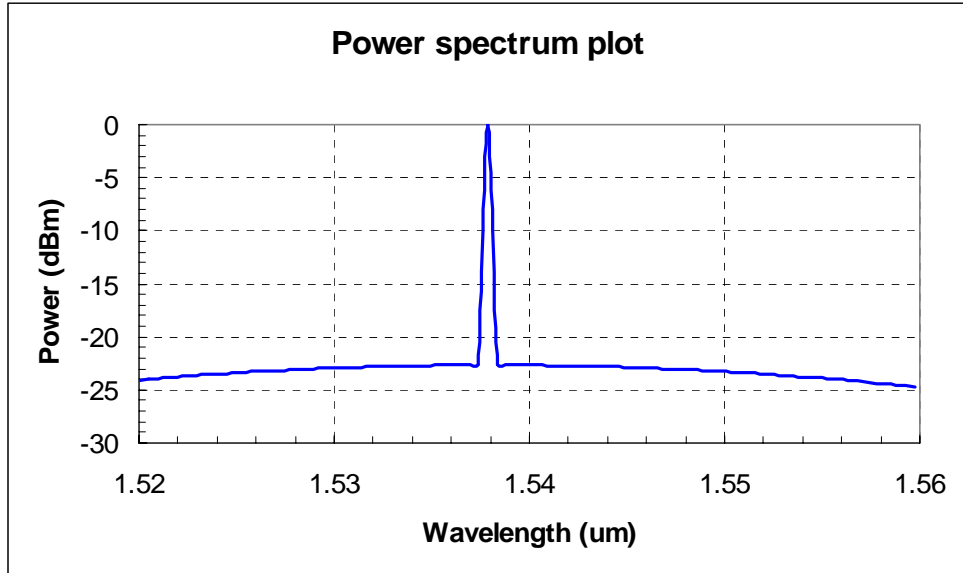


Figure 2.7 Optical spectrum of the SOA output for both signal and ASE

Our simulated NF is about 3dB higher than the measured data, which means the ASE is overestimated in our simulations. The part of reason is the spontaneous emission factor is Eq.(2.47) is just an approximated expression. The exact treatment need rigorous treatment of both guided modes and leakage modes of the waveguide inside the SOA [11]. Moreover, our more accurate expressions in Eq.(2.53) and Eq.(2.39) require more detailed expression for carrier distributions  $D_{\lambda}$ ,  $H_{\lambda}$  using Fermi-Dirac distributions.

### 2.3 Simplified Analytical Solution to SOAs

In traveling wave SOAs, the phase information of signals can be neglected. So, traveling wave power equations can be applied to both the signal and spontaneous emissions. Also, the material gain coefficients and spontaneous emission rate can be treated to be linearly dependent on the carrier density. Simon has developed a simple analytical solution for a traveling wave SOA based on several assumptions: (1) spontaneous emissions are negligible (2) There is no internal loss in this SOA (3) The

material gain is simply given by  $g=a(N-N_0)$ , and  $a$  is the gain constant [23]. Since reflectivities at both facets of this SOA are zeros, there are no any backward signals. So, the traveling wave power equation becomes [22]:

$$\frac{dS(z)}{dz} = \Gamma a(N - N_0)S(z) \quad (2.57)$$

The carrier rate Equation (2.32) is simplified to:

$$\Gamma V_g a(N - N_0)S(z) + \frac{N}{\tau} - \frac{J}{qd} = 0 \quad (2.58)$$

With help of Eqs. (2.57) and (2.58), we have:

$$\left( V_g \Gamma a S + \frac{1}{\tau} \right) \frac{dS}{dz} = \Gamma a \left( \frac{J}{qd} - \frac{N_0}{\tau} \right) S \quad (2.59)$$

It can also be written as:

$$\left( V_g \Gamma a + \frac{1}{S\tau} \right) dS = \Gamma a \left( \frac{J}{qd} - \frac{N_0}{\tau} \right) dz \quad (2.60)$$

To get a solution, we can directly integrate Eq.( 2.60)

$$S(0) = \frac{L}{V_g(G-1)} \left[ \frac{J}{qd} - \frac{N_0}{\tau} - \frac{\ln G}{\Gamma L a \tau} \right] \quad (2.61)$$

This equation shows that the signal gain  $G$  is a function of the input power and a drive current for a given amplifier. The output saturation power of an amplifier is the power at which its single pass gain decreases by 3 dB. Saturation is caused by carrier depletions in an SOA, which means the SOA carriers can not provide enough gain for strong input power. Beyond this saturation power, some nonlinear effects will occurs in the SOA. It is easy to calculate the saturation power of an amplifier with analytical solutions for an amplifier. With the help of Eq. (2.59), the gain coefficient can be defined as a function of signal photon density  $S$ .

$$g = \frac{g_0}{1 + S(z)/S_s} \quad (2.62)$$

$$S_s = \frac{1}{V_g \Gamma a \tau} \quad (2.63)$$

$$g_o = a \left( \frac{J}{qd} \tau - N_0 \right) \quad (2.64)$$

We can rewrite Eq. (2.59) as:

$$\frac{1}{S(z)} \frac{dS(z)}{dz} = \Gamma g = \frac{\Gamma g_o}{1 + S(z)/S_s} \quad (2.65)$$

Integrating Eq.(2.65):

$$\int_{S(0)}^{S(L)} \left( \frac{1}{S(z)} + \frac{1}{S_s} \right) dS = \int_0^L \Gamma g_o dz \quad (2.66)$$

Thus

$$\ln(G) + \frac{S(L) - S(0)}{S_s} = \Gamma g_o L \quad (2.67)$$

If  $S(L)$  is much smaller than  $S_s$ , which is the small signal case, the single pass gain becomes:

$$G = G_0 = \exp(\Gamma g_o L) \quad (2.68)$$

The saturation state is defined as  $G=0.5G_0$ , so the corresponding output photon density is:

$$S(L) - S(0) = S_s \ln 2 \quad (2.69)$$

We can approximately take:  $S(L) \approx S_s \ln 2$ , which means the output saturation power is

$$P_{sat} = V_s E d h \nu S_s \ln 2 = h \nu \frac{A}{\Gamma \tau a} \ln 2 \quad (2.70)$$

We can increase the saturation power by decreasing the carrier lifetime  $\tau$ , the confinement factor  $\Gamma$ , the gain constant  $a$  (so called differential gain) and/or increasing the amplifier cavity section area  $A$ .

For the Fabry-Perot (FP) amplifier, the phase information of the signal wave should be retained. Also both signal wave and ASE have to meet proper boundary conditions. A analytical solution for unsaturated FP SOAs can be obtained under the following assumptions: The gain is constant throughout the cavity of the SOA. Spontaneous emissions can be neglected. The Input signal is also small. The single pass gain can be calculated using Eqs.(2.11), (2.13) and (2.64):

$$G_\lambda = \exp \left[ \Gamma a \left( \frac{J}{qd} \tau - N_o \right) L - \alpha L \right] \quad (2.71)$$

Accordingly, the overall signal power gain can be obtained using Eq.(2.31). For a saturated FP-SOA, A simplified numerical solution is available by averaging photon densities of signal and spontaneous emissions over the length of cavity [22]. The overall power gain in Eq. (2.31) is called forward gain because it is the power gain for signal transmitted through the FP cavity. The backward power gain is used to calculate how much power reflected from this FP, which is given by [13]

$$G_b = \frac{(\sqrt{R_1} - \sqrt{R_2} G_\lambda)^2 + 4\sqrt{R_1 R_2} \sin^2 \varphi}{(1 - \sqrt{R_1 R_2} G_\lambda)^2 + 4\sqrt{R_1 R_2} \sin^2 \varphi} \quad (2.72)$$

For a given wavelength range, the pass-band gain ripple for the forward power gain is the ratio of gain peak to valley. It is easy to calculate this gain ripple from Eq. (2.31):

$$RP = 10 \lg \frac{(1 + \sqrt{R_1 R_2} G_\lambda)^2}{(1 - \sqrt{R_1 R_2} G_\lambda)^2} \quad (2.73)$$

These two Equations for FP-SOA are very useful to evaluate a traveling wave SOA because there is always residual facet reflectivity in traveling wave SOA fabrication. In general, the gain ripple should be less than 1dB cross the pass-band. In addition to these gain ripple effects from residual facet reflectivity, another problem from the facet reflectivity is the forward-backward gain ratio. For  $R_1=R_2$ , this ratio is about  $1/(G_\lambda R)$ . If the forward gain is 30 dB, and  $R=10^{-6}$ , the ratio is 30 dB.

In this chapter, an overview of SOAs theory is first presented, and a new formula for the spontaneous emission factor is also derived. Both numerical and analytical solutions are discussed in details. These solutions are successfully applied to some exiting SOA examples. As we mentioned early, the gain coefficient model is critical to predict performances. In next chapter, we will discuss several models for gain coefficients. Wavelength conversion through XGM, one of applications of SOA nonlinearity, is also going to explored in details in the coming chapter.

## CHAPTER 3

# WAVELENGTH CONVERSION THROUGH CROSS-GAIN MODULATION IN SEMICONDUCTOR OPTICAL AMPLIFIERS

### 3.1. Introduction

Significant progress has been made on wavelength converters based on semiconductor optical amplifiers (SOA) [29-30], in which modulation bit rates as high as 100 Gb/s have been achieved. Previous theoretical studies have employed both analytic and numerical methods [15,17]. In the numerical studies, the governing differential equations are solved in time domain using the finite difference method (FDM). In all models, the waveguide internal loss is assumed uniform across the cavity of the SOA, and the gain coefficient is assumed proportional to the difference between the carrier and transparency carrier densities; the differential gain is assumed constant accordingly. These assumptions are valid only for wavelengths in the vicinity of the peak gain wavelength. Therefore, high accuracy for wideband wavelength conversion may not be guaranteed.

A steady state numerical model of SOA wavelength converters is presented in this paper. In it, a new gain coefficient model of bulk InGaAsP SOAs developed by Yariv [31] and Connelly [25] is applied, which includes the internal loss variation with the electron carrier density. In our model, all physical variables, including the carrier density, gain coefficient, differential gain, and internal loss, vary spatially along the length of the SOA cavity. The model predicts the wavelength-dependent characteristics of a wavelength converter in both large and small signal regimes. Key performance parameters, including the conversion efficiency and bandwidth, can be evaluated and

optimized with respect to choices in the pump and probe wavelengths, input power levels, and cavity length.

### 3.2 Different Gain Coefficient Models

The wavelength dependence of gain coefficients is critical to simulate and predict performances of this type of wavelength converter because wavelength converters use cross-gain modulation among different wavelengths. Marcuse [11, 27] developed a model for gain coefficients, in which Lorentzian functions are used to describe wavelength dependence of gain coefficients. This model is similar to the gain model for an ordinary two levels lasing medium. It has been already discussed in Chapter 2. The problem of this model is that it requires several parameters, such as the transparency carrier density  $N_0$ , the line width factor  $W$ , and the stimulated emission constant  $B$ . Moreover, this model does not include the temperature effect.

Another simplified model uses polynomial approximation [13], and parabolic gain-wavelength dependence is used to represent the wavelength dependence of gain coefficients:

$$g_{\lambda}(N) = a(N - N_0) - a_1(\lambda - \lambda_p)^2 \quad (3.1)$$

$$\lambda_p = \lambda_0 - a_2(N - N_0) \quad (3.2)$$

This model also needs several empirical parameters including the transparency carrier density, and it does not include the temperature variations. Connelly proposed a comprehensive wideband model for a bulk InP-InGaAsP SOA based on Yariv's work.

The gain coefficient for a bulk InP-InGaAsP SOA is related to the electron carrier density and the light frequency by [25]

$$g(\nu, N) = \frac{c^2}{4\sqrt{2}\pi^{3/2}n_1^2\tau_1\nu^2} \left[ \frac{2m_e m_{hh}}{\hbar(m_e + m_{hh})} \right]^{3/2} \sqrt{\nu - \frac{E_g(N)}{h}} (f_c(\nu) - f_v(\nu)) \quad (3.3)$$

where  $c$  is the speed of light in vacuum,  $n_1=3.22$  is the refractive index of the active region of the SOA,  $\tau_1$  is the radiative lifetime of the carrier,  $\nu$  is the photon frequency,  $h$  is Planck's constant, and  $m_e = 4.10 \times 10^{-32}$  kg, is the electron effective mass for the conduction band,  $m_{hh} = 4.19 \times 10^{-31}$  kg is the heavy hole effective mass for the valence band,  $N$  is the electron carrier density,  $E_g$  is the bandgap energy. The  $f_c$  and  $f_v$  are the Fermi-Dirac distributions in the conduction and valence bands, respectively, and  $\tau_1$  is found through

$$\tau_1 = \frac{1}{A_{rad} + B_{rad}N(z)} \quad (3.4)$$

where  $A_{rad}=1.0 \times 10^7 \text{ s}^{-1}$  and  $B_{rad}=3.6 \times 10^{-16} \text{ m}^3 \text{ s}^{-1}$ . For  $f_c$  and  $f_v$  we have:

$$f_c(\nu) = \left[ 1 + \exp\left(\frac{E_c(\nu) - E_{fc}}{kT}\right) \right]^{-1} \quad (3.5)$$

$$f_v(\nu) = \left[ 1 + \exp\left(\frac{E_v(\nu) - E_{fv}}{kT}\right) \right]^{-1} \quad (3.6)$$

and

$$E_c = \left[ h\nu - E_g(N) \right] \frac{m_{hh}}{m_e + m_{hh}} \quad (3.7)$$

$$E_v = - \left[ h\nu - E_g(N) \right] \frac{m_e}{m_e + m_{hh}} \quad (3.8)$$

Also

$$E_g(N) = E_o - qK_g N^{1/3} \quad (3.9)$$

where  $E_{fc}$  is the quasi-Fermi level of the conduction band.  $E_{fv}$  is the quasi-Fermi level of the valence band. These quasi-Fermi levels can be calculated using Nilsson approximation.  $E_o = 0.777$  eV is the bandgap energy without carrier injection,  $q$  is the electronic charge, and  $K_g = 9 \times 10^{-11}$  eVm the bandgap shrinkage factor. The gain coefficients versus different wavelengths are plotted for different carrier densities. Figure 3.1 shows these results. As the carrier density is increased, the material gain peak shifts to shorter wavelength, and increase the gain coefficient value. So this model can predict the well-known effect of nonlinear gain compression.

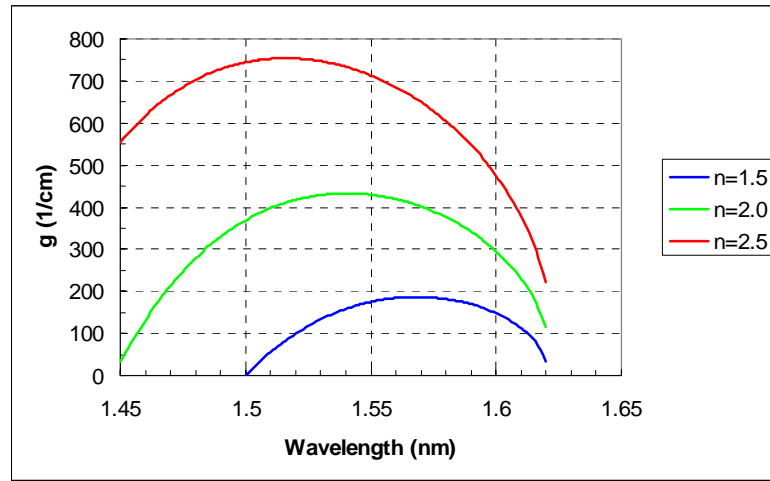


Figure 3.1 Gain coefficient plots versus wavelengths

### 3.3 Steady State Numerical Model for SOA Based Wavelength Converters

A semiconductor optical amplifier based on cross gain modulation (XGM) is investigated in this paper. Co-propagating pump and probe beams are used, where the information carried on the modulated pump ( $\lambda_p$ ) is complementarily copied onto the CW

probe ( $\lambda_c$ ) as shown in Figure 3.2. Additionally, the SOA-wavelength converter is assumed to operate in saturation mode in order to enhance the modulation bandwidth.

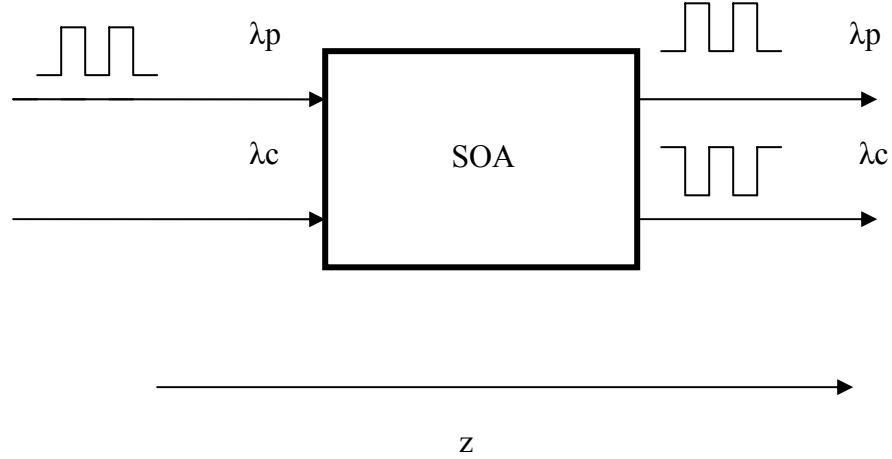


Figure 3.2 Schematics of an SOA wavelength converter

Consequently, amplified spontaneous emission (ASE) is neglected [32]. The steady state equations for photons and electron carriers are [11,22]

$$\frac{dS_i(z)}{dz} = [\Gamma g(v_i, N(z)) - \alpha(N(z))]S_i(z) \quad i=1, 2 \quad (3.10)$$

$$\frac{dN(z)}{dt} = \frac{J}{qd} - R(N(z)) - V_g \Gamma [g(v_1, N(z))S_1(z) + g(v_2, N(z))S_2(z)] = 0 \quad (3.11)$$

where  $S_1$  is the photon density of the modulated pump, and  $S_2$  is the photon density of the CW probe. The gain coefficients  $g$  and the waveguide loss  $\alpha$  are functions of the electron carrier density.  $J$  is the injection current density,  $R$  is the spontaneous recombination rate (including the radiative and nonradiative mechanisms),  $d$  is the thickness of the active

region of the SOA,  $V_g$  is the group velocity, and  $\Gamma$  is the mode confinement factor. The waveguide internal loss is given by:

$$\alpha(N) = \alpha_o + \Gamma\beta N \quad (3.12)$$

where  $\alpha_o = 30 \text{ cm}^{-1}$  is the carrier-independent absorption term accounting for intrinsic material loss, and  $\beta = 7.5 \times 10^{-21} \text{ m}^2$  is the carrier dependent term due to intervalence band absorption [11,22,25]. To model the dynamic property of an SOA wavelength converter, the photon and carrier densities can be described by large steady components with small perturbations. They are written as  $S_i(z,t) = S_{io}(z) + s_i(z)\exp(j\omega t)$ ,  $i = 1, 2$ , for the photon density, and  $N(z,t) = N_o(z) + n(z)\exp(j\omega t)$  for the electron carrier density, where  $\omega$  is the angular modulation frequency of the pump signal. Using the first order approximation for small signals, we have:

$$R(N(z,t)) = R(N_o(z)) + \frac{\partial R}{\partial N} n(z)\exp(j\omega t) \quad (3.13)$$

$$g(v_i, N(z,t)) = g(v_i, N_o(z)) + \frac{\partial g}{\partial n} n(z)\exp(j\omega t) \quad (3.14)$$

$$\begin{aligned} \alpha(N(z,t)) &= \alpha(N_o(z)) + \frac{\partial \alpha}{\partial n} n(z)\exp(j\omega t) \\ &= \alpha(N_o(z)) - \Gamma\beta n(z)\exp(j\omega t) \end{aligned} \quad (3.15)$$

Plugging Equations (3.13-3.15) into Equations (3.10-3.11) with some basic algebraic operations, the steady state equations for large signals can be obtained:

$$\frac{dS_{i0}(z)}{dz} = [\Gamma g(v_i, N_o(z)) - \alpha(N_o(z))]S_{i0}(z) \quad i=1,2 \quad (3.16)$$

$$\frac{J}{qd} - \frac{N_o(z)}{\tau_d} - V_g \Gamma [g(v_1, N_o(z))S_{10}(z) + g(v_2, N_o(z))S_{20}(z)] = 0 \quad (3.17)$$

The small signal equations are

$$\frac{ds_i(z)}{dz} = [\Gamma g(v_i, N_o(z)) - \alpha(N_o(z))]s_i(z) + \Gamma[a_n(v_i, N_o(z)) - \beta]S_{io}(z)n(z) \quad (3.18)$$

$$n(z) = -\frac{A(z)}{B(z)} \quad (3.19)$$

$$A(z) = \Gamma V_g [g(v_1, N_o(z))s_1(z) + g(v_2, N_o(z))s_2(z)] \quad (3.20)$$

$$B(z) = \frac{1}{\tau_a} + \Gamma V_g [a_n(v_1, N_o(z))S_{10}(z) + a_n(v_2, N_o(z))S_{20}(z)] + j\omega \quad (3.21)$$

$$a_n(v_i, N) = \frac{\partial g(v_i, N)}{\partial N} \quad (3.22)$$

$\tau_d$  is the spontaneous lifetime, related to the carrier density by [11]

$$R(N) = \frac{N}{\tau_d} \quad (3.23)$$

and  $\tau_a$ , the spatial average of  $dN/dR$ , and given by:

$$\frac{1}{\tau_a} = \left( \frac{\partial R}{\partial N} \right)_{N=N_m} \quad (3.24)$$

where  $N_m$  is the spatial average of the carrier density  $N_o(z)$ . In general, the spontaneous recombination rate is given by  $R(N) = R_1N + R_2N^2 + R_3N^3$ , in which  $R_1$ ,  $R_2$ , and  $R_3$  represent the nonradiative, spontaneous, and Auger recombination coefficients, respectively.

These coefficients depend on device materials and fabrication processes, however, and are difficult to determine accurately. As a result, the recombination rate,  $R$ , is usually approximated by Equation (17) [11, 22]. The differences between  $\tau_d$  and  $\tau_a$  can be explained by the different operations of large signal and small signal processes, and mathematic derivations above [16]. The differential gain,  $a_n$ , is a function of optical frequency and carrier density; it therefore varies throughout the SOA cavity. This contrasts with the conventional gain coefficient model based on the polynomial

approximation method, in which the differential gain is assumed constant [14]. Additionally in our studies, the frequency separation between the pump and probe is assumed large compared to the frequency response of the carrier stimulated emission. Four-wave-mixing effects can thus be ignored [32].

### **3.4 Numerical Solution Using the Finite Difference Method in Spatial Domain**

#### **3.4.1 Large signal simulations**

In our method, the large signal Equations, (3.3), (3.5) and (3.16) through (3.17) are first solved using FDM in spatial domain; the results are substituted into the small signal equations, (3.18) through (3.22). The latter are then solved using the same FDM algorithm. To apply the FDM, the SOA is divided into small sections of  $5\mu\text{m}$  length. A numerical algorithm for solving finite differential equations is used similar to that in Ref. 25, in which the carrier density is adjusted throughout the SOA cavity through multiple iterations. Both carrier density  $N$  and differential gain  $a_n(\nu_i, N)$  are numerically calculated using Equations (3.3) and (3.16-3.17). Numerical values of differential gain vary between  $5.0 \times 10^{-20} \text{ m}^2$  and  $7.0 \times 10^{-20} \text{ m}^2$ , which is in good agreement with experimental results [33]. Gain coefficients are wavelength dependent and varied across the SOA cavity as a function of the carrier density.

The model was tested for long and short bulk InGaAsP SOA's that were fabricated using the same type of wafer, and which have active regions of  $0.43 \mu\text{m}$  thickness and  $0.5 \mu\text{m}$  width [17,34]. The long SOA has a  $1250 \mu\text{m}$  cavity length, and uses a 220 mA injection current; the short SOA has a  $450 \mu\text{m}$  cavity length, and uses an 80 mA injection current. In a down-converter, the pump wavelength is  $1.55 \mu\text{m}$  and the

input power is -5 dBm. The probe signal at 1.54  $\mu\text{m}$  has an input power of -8 dBm. The pump and probe wavelengths are switched for an up-converter. The above parameters are taken from Ref. 17, and are used to calibrate our model. The down-converter is simulated first. The carrier spontaneous lifetime  $\tau_d$  is assumed to be 400 ps, and its small signal counterpart  $\tau_a$  is assumed to be 200 ps [15-16]. The confinement factor is 0.4. With these values, the large signal solution was first obtained. The pump and probe optical powers, carrier density, the gain coefficients, and the internal loss are shown successively in Figures. (3.3-3.6). Figure 3.3 and Figure 3.4 are for the long SOA, and Figure 3.5 and Figure 3.6 for the short SOA. Results show major differences between the short and long SOA wavelength converters for large signal simulations. In the case of a long SOA, the saturation and gain competition between 1.55  $\mu\text{m}$  and 1.54  $\mu\text{m}$  signals result in the saturation of the 1.54  $\mu\text{m}$  signal as shown in Figure 3.3(a). This can be qualitatively explained by strong local carrier depletion induced by the 1.55  $\mu\text{m}$  signal. The carrier density distribution across the SOA cavity keeps almost identical for up and down converters, with only about 0.5% difference at the end of the cavity, as shown in Figure 3.3(b) and Figure 3.4 (b).

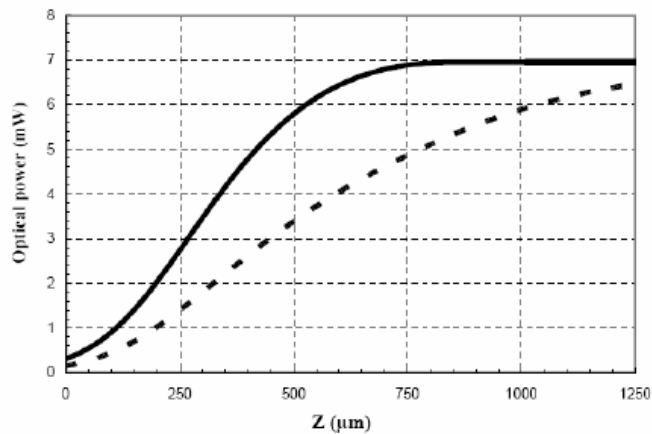
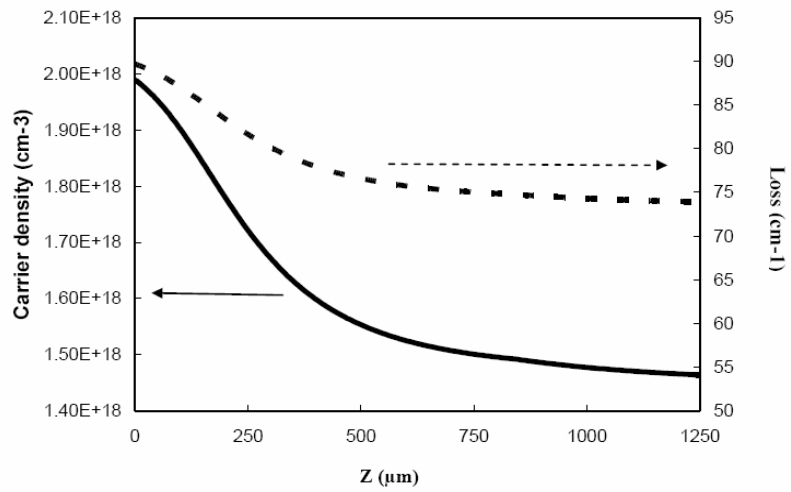


Figure 3.3 (a)



(b)

Figure 3.3 Large signal simulation results for the long SOA up converter: (a) pump power (line) and probe power (dot), (b) carrier density (line) and internal loss (dot)

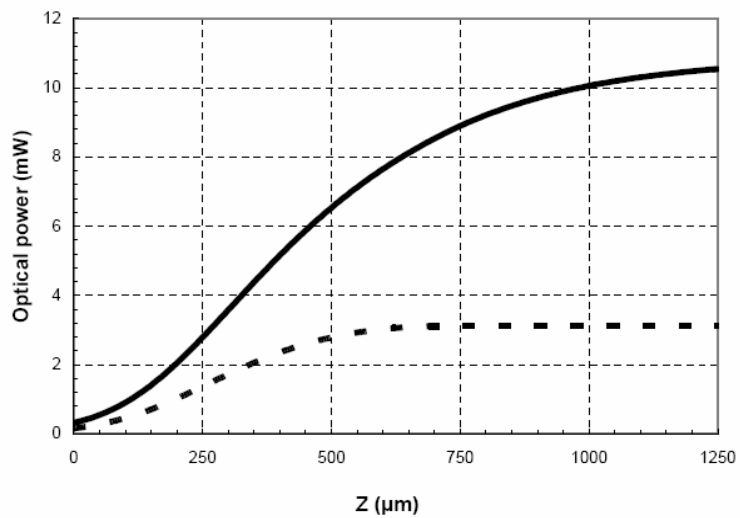
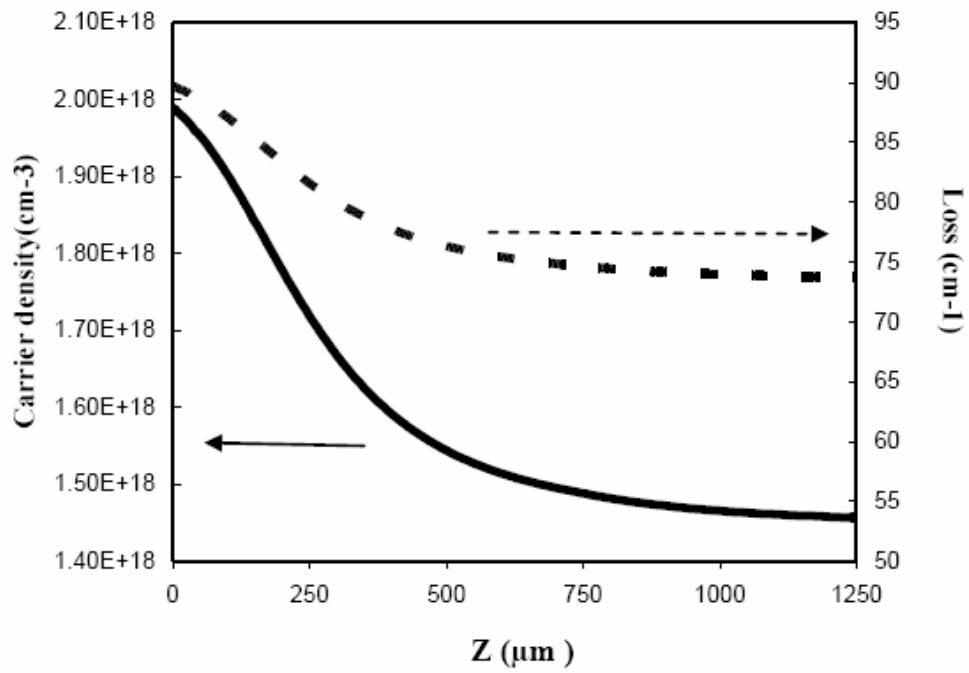


Figure 3.4 (a)



(b)

Figure 3.4 Large signal simulation of down conversion using a long SOA: (a) pump power (line) and probe power (dot), (b) carrier density (line) and internal loss (dot)

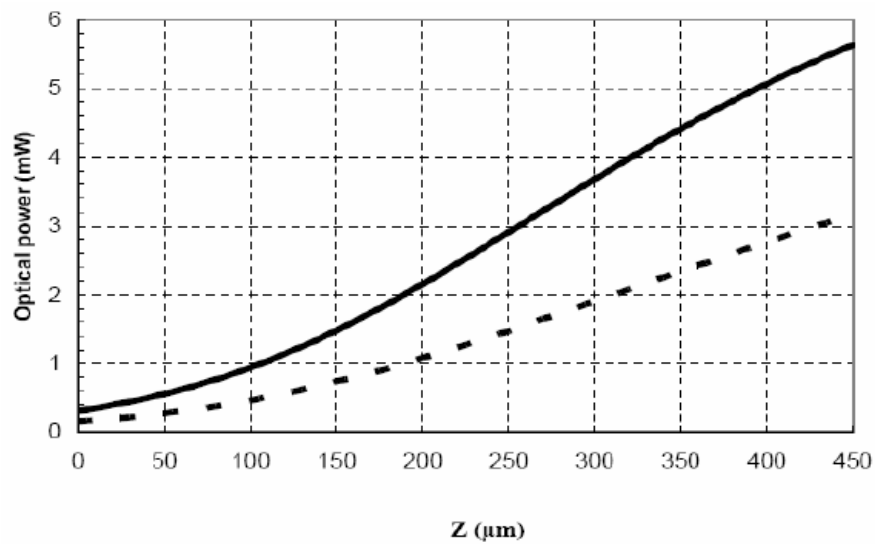
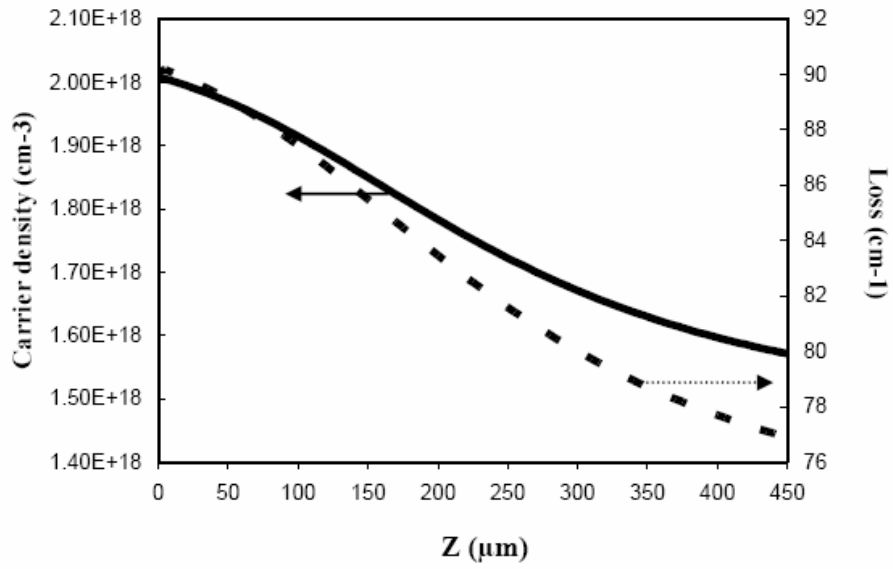


Figure 3.5 (a)



(b)

Figure 3.5 Large signal simulation results for the short SOA up converter: (a) pump power (line) and probe power (dot), (b) carrier density (line) and internal loss (dot)

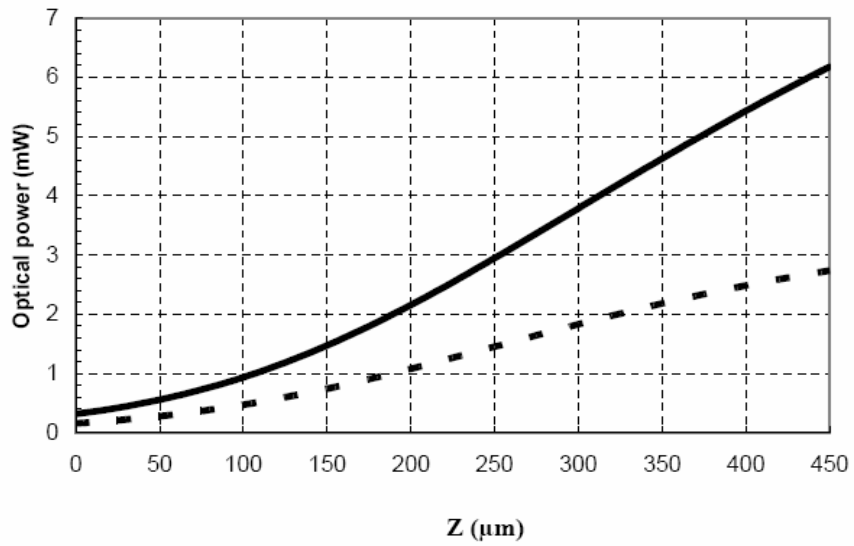
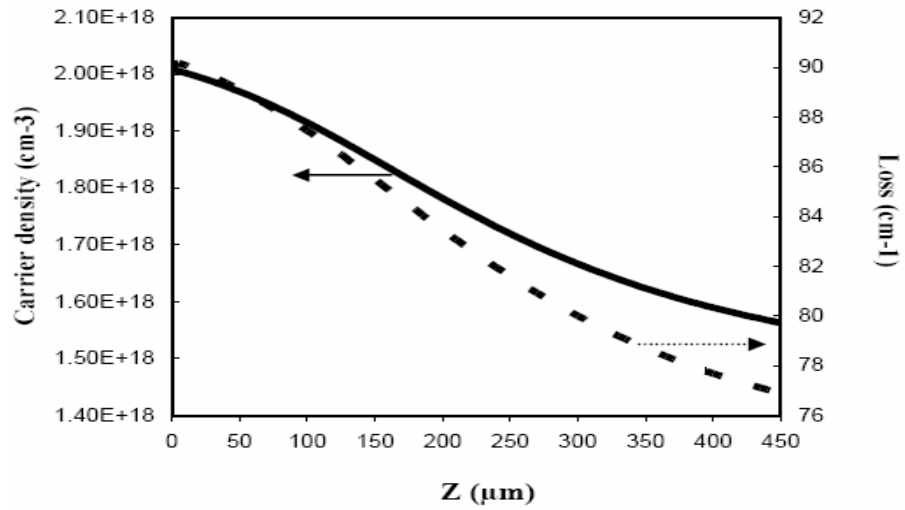


Figure 3.6 (a)



(b)

Figure 3.6 Large signal simulation results for the short SOA down converter: (a) pump power (line) and probe power (dot), (b) carrier density (line) and internal loss (dot)

In the short SOA wavelength converter, the large signal behavior differs from that long SOA converter as shown in Figure 3.5 and Figure 3.6; in that 1.54  $\mu\text{m}$  signal experiences no saturation in either up-conversion or down-conversion. Furthermore, the gain difference between pump and probe signal is less than 0.5 dB, as shown in Table 1. The small gain difference leads to up and down conversion processes of essentially equal efficiency. The processes are analyzed in more detail in the small signal simulations.

Table 1 Large signal gain for long and short wavelength converter

Gain (dB)	Long SOA		Short SOA	
	Down conversion	Up conversion	Down conversion	Up conversion
Pump signal	15.2	13.0	12.9	12.5
Probe signal	13.4	16.1	12.4	13.0

### 3.4.2 Small signal simulations

The small signal components in Eqs.(3.15-3.19) include the pump power, probe power and carrier density, all of which are complex. The phase difference between the pump and probe is the consequence of cross gain modulation. In our simulations, a sign difference occurs between the real components of the pump and probe signals, which is the result of the phase difference between the pump and probe signals. The small signal simulation results shown in Figure 3.7 through Figure 3.9 were then obtained by solving the equations, (3.15) through (3.19) based on the large signal simulation results, and FDM in spatial domain is used to solve those equations for small signal components. The small signal values of the pump power, probe power, and carrier density depend on the modulation frequency. These are numerically determined and displayed in Figure 3.8 and Figure 3.9. For both long and short SOAs, the small signal carrier distribution is the same for up and down conversion as is shown in Figure 3.9, in a similar manner to the large signal result. At low modulation frequency, the carrier density peak is close to the input end of the SOA; at high modulation frequency, the peak is shifted and flattened toward the output end of the SOA.

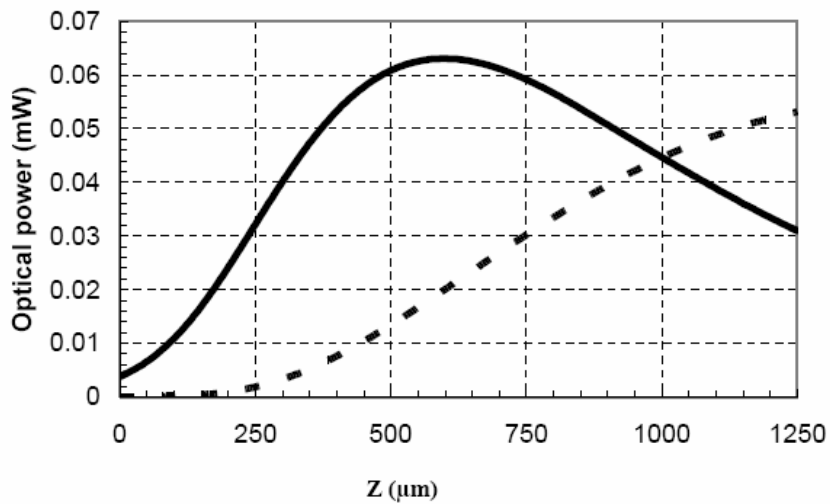
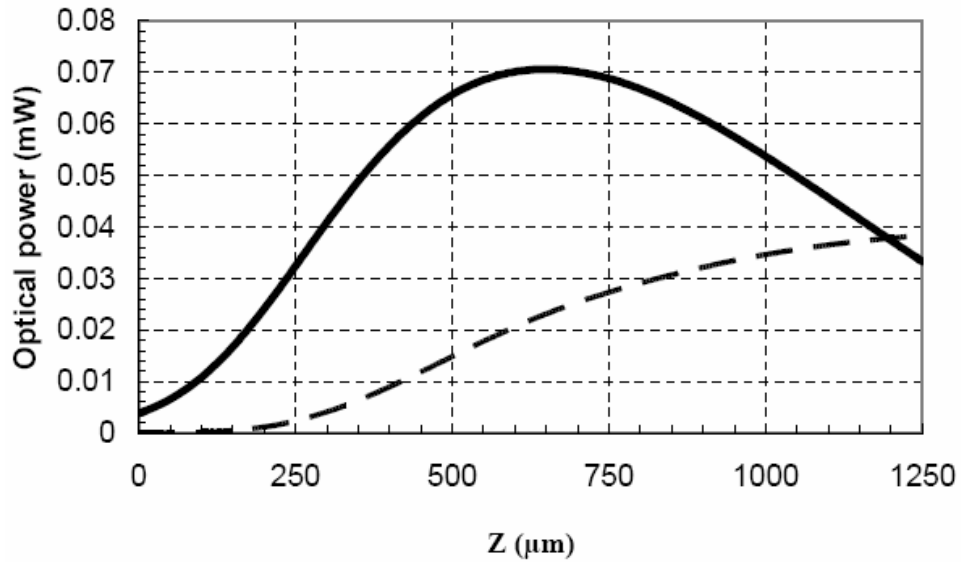


Figure 3.7 (a)



(b)

Figure 3.7 Small signal simulation results for the long SOA converter: (a) pump power (line) and probe power (dot) for up conversion at 6 GHz modulation, (b) pump power (line) and probe power (dot) for down conversion at 5 GHz modulation

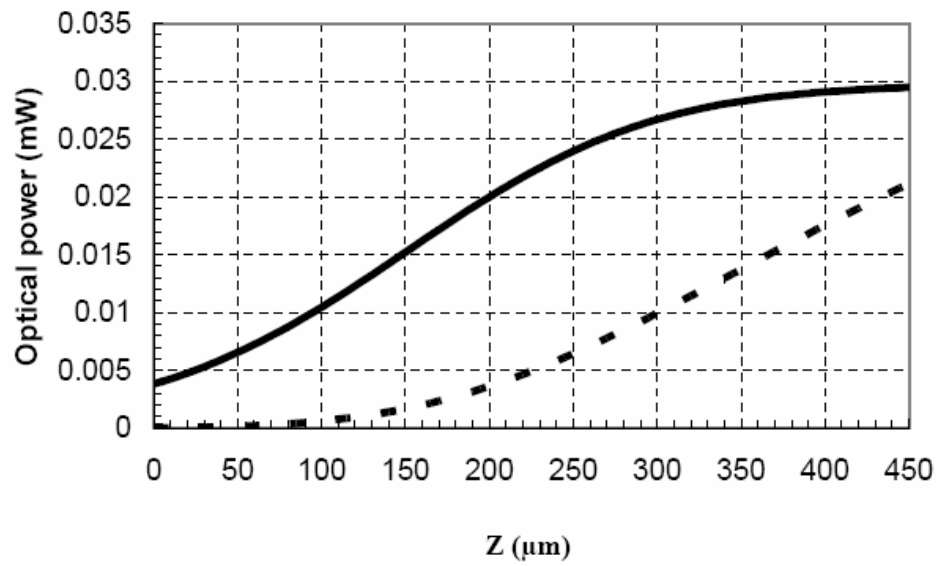
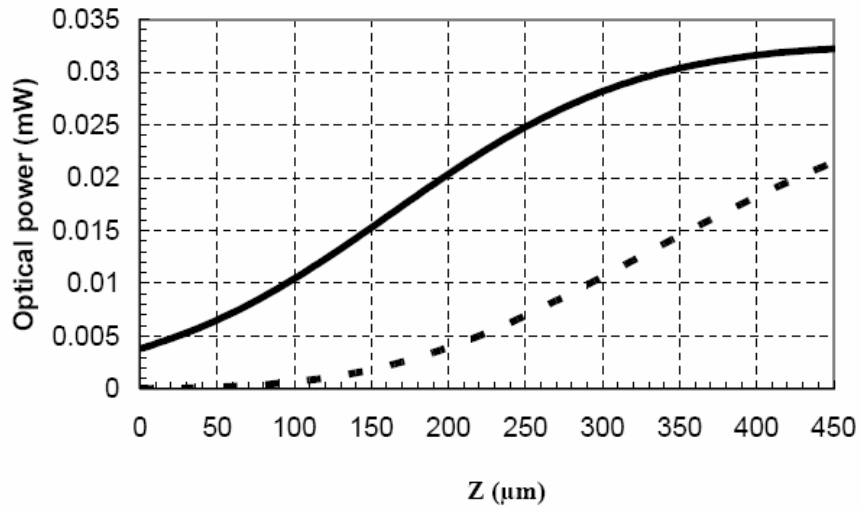


Figure 3.8 (a)



(b)

Figure 3.8 Small signal simulation for the short converter at 1GHz modulation: (a) pump power (line) and probe power (dot) for up conversion, (b) pump power (solid ) and probe power (dot) for down conversion

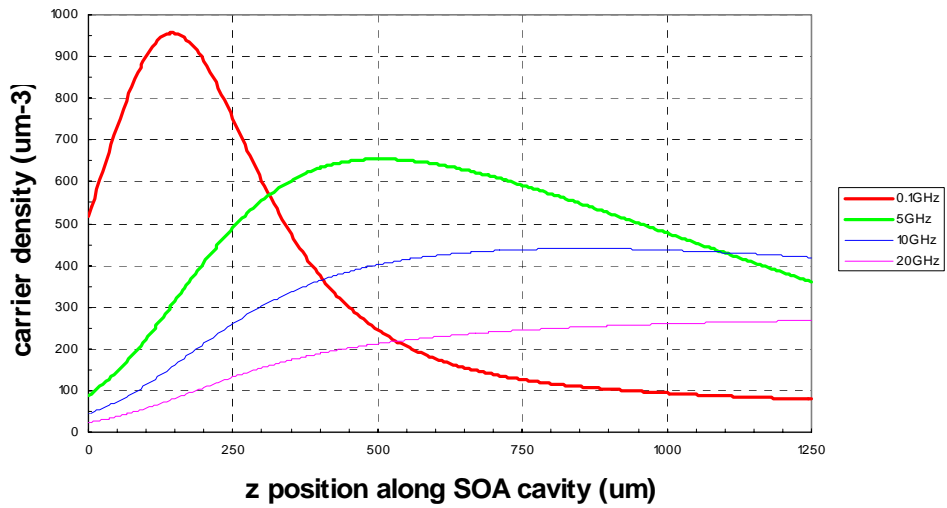
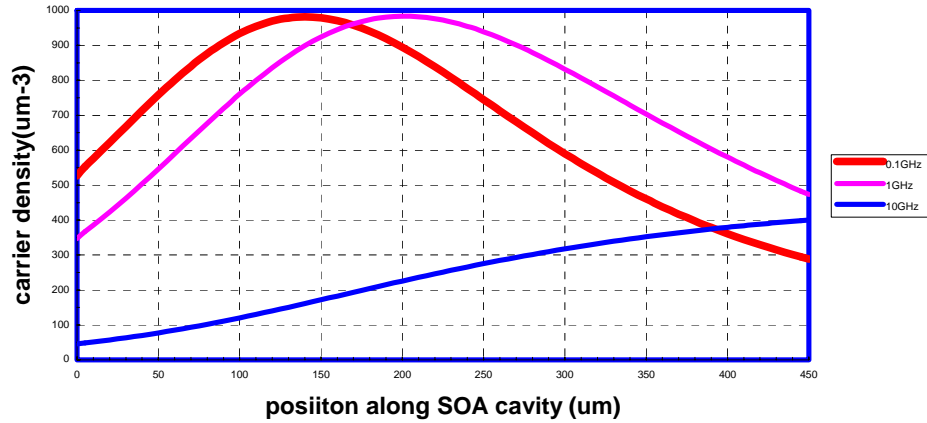


Figure 3.9 (a)



(b)

Figure 3.9 Small signals of carrier density versus different modulation frequency: (a) the long SOA, (b) the short SOA

The ratio of the optical modulation depth (OMD) of the probe signal at the output end of the wavelength converter to the OMD of the pump signal at the input end is defined as the conversion efficiency

$$\eta(\omega) = \frac{OMD(\omega, L, 2)}{OMD(\omega, 0, 1)} \quad (3.25)$$

where  $\omega$  denotes the angular modulation frequency,  $L$  is the length of the SOA cavity, and  $OMD(\omega, z, i) = |s_i(\omega, z)/S_{i0}(z)|$ , with  $i=1,2$ . The OMD of pump signal at the input end of SOA is 3% in our simulation. There is good agreement between our simulation results and published results as shown in Figure. 3.10(a) [17]. The simulation results in Ref. 17 are obtained using a large signal numerical model in the time domain, whereas our model is based on the steady state small signal approximation. The little deviation is that we treat the SOA with traveling wave case with zero reflectivity at each end of facets of

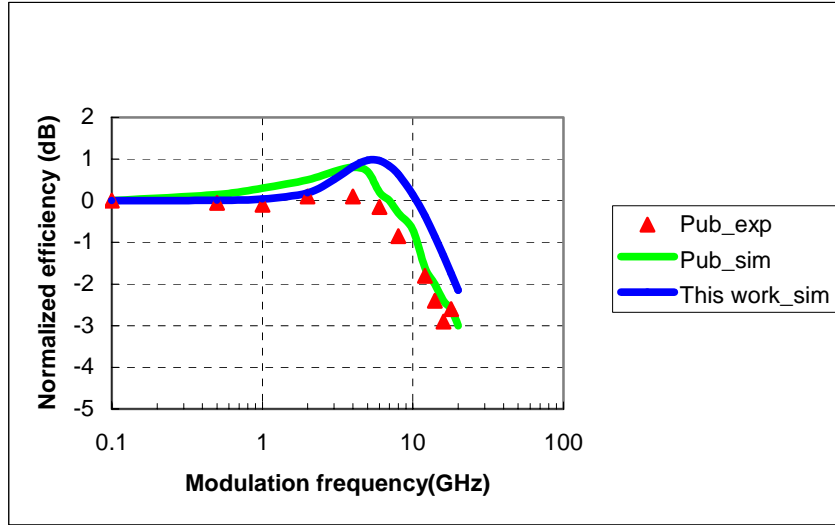


Figure 3.10 A Long SOA down converter efficiency comparisons: our modeling results (blue), simulation results (green) and experimental data (red) in Ref. 17

SOA, and the ASE is taken into account in Ref.17; and those differences slightly change the simulation results because the non-zero reflectivity at the facets of SOAs change the boundary conditions of those differential equations governing the photon and carriers transportation [12]. These approximations cause the signal to be over amplified. As a result, larger signal power reduces the carrier lifetime of stimulated emission and the effective life time of carriers [12, 14]. This reduced effective life time of carriers extends the modulation bandwidth. This is the reason why our simulation result is little overshoot at modulation frequencies beyond 10 GHz. At low modulation frequency, our simulation works better than the simulated results in Ref. 17. The modulation efficiency at low frequency is mainly determined by the spontaneous lifetime because the carrier variation can follow the light modulation at low modulation frequency.

As we all know that small signal performance of an SOA is strongly depends on its large signal behavior. An approximately 2.5 dB large signal gain difference exists

between the 1.55  $\mu\text{m}$  and 1.54  $\mu\text{m}$  signals for both up and down long SOA converters as shown in Table 1. This gain difference attributes the asymmetric performances of up and down converters in a long SOA. The relative large gain for pump signal makes the SOA operate in deep saturation states, and increases the wavelength conversion bandwidth, especially for a down converter as shown in Figure 3.11 [14-15]. The conversion efficiency of a wavelength converter is normalized relative to its efficiency at the modulation frequency of 0.1 GHz. The normalized conversion efficiency can be calculated using Eq. (3.25)

$$NE(\omega) = 10 \lg \frac{\eta(\omega)}{\eta(\omega = 0.1\text{GHz})} \quad (3.26)$$

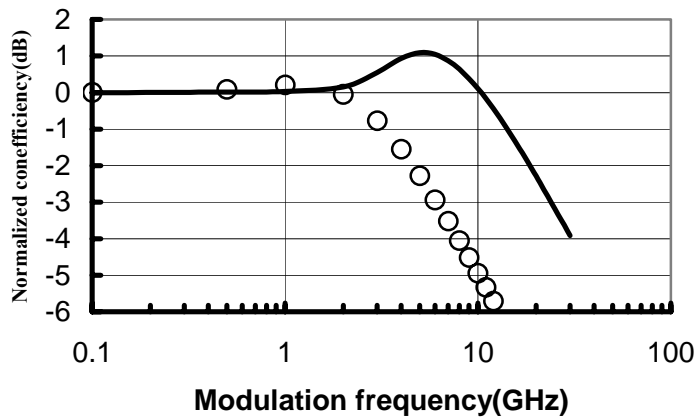


Figure 3.11 Normalized converter efficiency plots of down-converters, the 1250  $\mu\text{m}$  SOA (solid line), and the 450  $\mu\text{m}$  SOA (circles)

To investigate the up-converter, the pump and probe wavelengths are interchanged, with all other parameters fixed. For both the 1250  $\mu\text{m}$  and 450  $\mu\text{m}$  cavities, the efficiency of the up-converter is degraded, which is consistent with the extinction

ratio degradation of the up-converted signal [17]. However, for the long cavity, the 3-dB bandwidth increases by about 6 GHz in the up-converter as shown in Figure 3.12 and Figure 3.13, while the short cavity device maintains nearly the same bandwidth for both down- and up- conversion as shown in Figure 3.14.

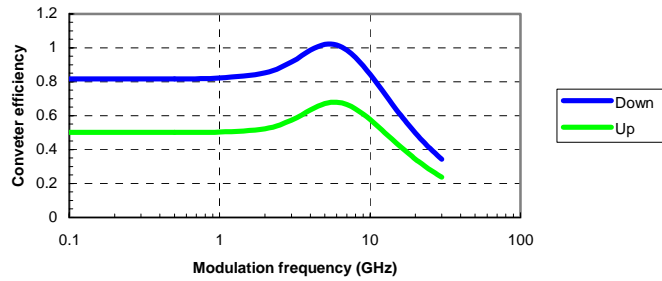


Figure 3.12 Down (blue) and up conversion (green )for the 1250  $\mu\text{m}$  SOA

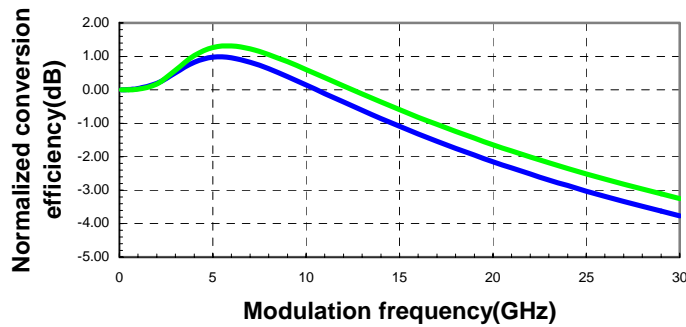


Figure 3.13 Normalized down (blue) and up conversion (green) for the 1250  $\mu\text{m}$  SOA

This latter result occurs because pump and probe signals are almost indistinguishable in the short SOA due to the little difference of large signal gains between pump and probe signals. Our simulations show that the large signal gains are very close for the pump and

probe signals in the short SOA; values near 13dB occur in both up-converter and down-converter. However, the large signal gains for pump and probe signals in case of a long SOA differed by about 2.5dB. Gain competition between different wavelengths is more severe in the case of the long SOA. As a result of relative large gain provided by the long SOA and the more accurate gain coefficient model based on different wavelengths and the carrier variation across an SOA [25].

In the long SOA converter, the peak of modulation efficiency occurs at 5GHz for down conversion and at 6 GHz for up conversion. This peak occurs at the modulation frequency at which the plots of small signal components of pump and probe signals tend to cross at the end of an SOA as shown in Figure 3.7. In that case, the small signal component of the pump has undergone local attenuation close to the output end of the SOA, and the small signal component of the probe has monotonically increased across the SOA cavity.

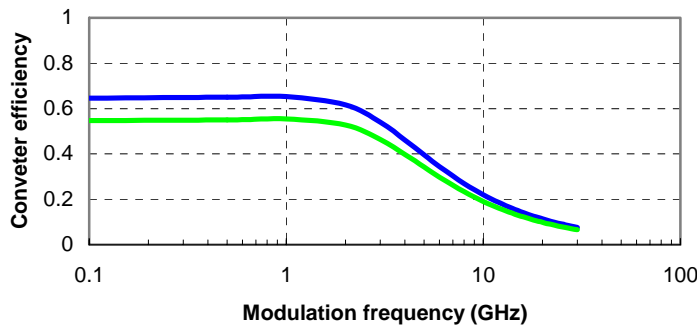


Figure 3.14 Down (blue) and up conversion (green ) comparison for the 450  $\mu\text{m}$  SOA,

### 3.5 Conclusions

A steady state numerical model of the bulk semiconductor optical amplifier wavelength converter is reported based on an analytical model of the gain coefficient. Our model takes into account the spatial variations of the carrier density, gain coefficients, differential gain and waveguide loss through the cavity of SOA. To the best of our knowledge, these variations are included in a SOA wavelength converter model for the first time. SOAs with different cavity lengths were investigated in both down-conversion and up-conversion models. The simulation results of the steady state model are consistent with prior published results using the finite difference time domain method [17].

In addition, long and short SOA wavelength converters were investigated using our model. This is the first application of a steady state numerical model with an analytic gain coefficient to up-conversion and down-conversion process in short and long SOAs. In the long SOA wavelength converter, we find that the down-conversion has about 3-dB increase of conversion efficiencies, but with a 6 GHz normalized modulation bandwidth decrease than that of the up-conversion as shown in Figures 3.12 and 3.13. However, the up and down-conversion efficiencies are almost identical for the short device, which are plotted in Figure 3.14. This equal performance feature of the up-converter and down converter using an SOA is one of the critical factors to evaluate wavelength length converters. A long SOA wavelength converter does not have such features even though it can offer large bandwidth. This is the trade off between the modulation bandwidth and the equal performance of an up-converter and a down-converter. Our model can be used

to optimize SOA-wavelength converters with proper cavity length to meet system requirements on bandwidth and equal performance of the up and down conversion.

## CHAPTER 4

### HIGH BRIGHTNESS LED AND SOLID STATE LIGHTING

#### 4.1 Introduction to Solid State Lighting

Lighting accounts for approximately 20% of total energy consumption in the U.S. Thus, it is difficult to overstate the importance of developing more efficient light sources. One such source is solid state lighting based on LEDs. LEDs offer significant advantages over conventional light sources such as incandescent lamps, fluorescent lamps, and discharge light sources because of their higher lighting efficiency, longer lifetimes, lower power consumption, and directly tunable color effects without additional color filters.. Currently, the majority of LED applications are indicators, in which viewers look directly at LEDs at relatively short distances, and signals. However, LEDs have been commercialized in both mobile LCD displays and traffic lights, and significant progress is being made toward the development of commercial solid state light sources based on high power LEDs [35]. Strictly speaking, all applications mentioned above are defined as indicator-type applications because the light source is a main focus of the viewers.

However, solid state lighting will be used as a general lighting source in the future, much like incandescent light bulbs today. The major functional differences of general light sources compared to indicator lights are [35]: First, the main purpose of general illumination sources is to provide ambient light for viewers. Surrounding objects, not light sources, are often the focus of viewers in this case. Second, the illumination flux of solid state general illumination sources is usually several orders of magnitude higher than that of indicator sources. Third, most general illumination sources are white, whereas indicator lights are found in various colors.

In general, white light can be obtained by four approaches: 1) directly mixing red , green and blue (RGB) light from their corresponding monochromatic LEDs in the

spatial domain; 2) mixing RGB light sequentially at a higher frequency than the human eye can detect; 3) using a blue LED to pump a yellow phosphor having the capability to emit green and red light, and combining the remaining blue light from the LED pump with the emitted red and green light from the phosphors; 4) pumping RGB phosphors with a UV LED [35-36]. The first two approaches offer the best efficiency and color rendering, and the correlated color temperature of the white light emitted by these two techniques can be programmed.

III-V semiconductor materials are used in solid state lighting to produce monochromatic light. AlInGaP grown on a GaAs substrate emits red or amber light. Transparent GaP is used to replace GaAs using the wafer bonding technique in order to overcome light absorption by GaAs [35]. The green, blue, and UV light can be obtained from AlInGaN grown on either sapphire or silicon carbide (SiC) [37]. These technologies can produce full color LEDs which are superior to conventional color lighting by filtering white light.

The current challenges faced by solid state lighting are to increase total flux output from multiple LEDs assembled into one lamp, and to increase lighting efficiency from each individual LED. A 60 Watt incandescent bulb emits about 1 kilo-lumen, which is about 20 times the light output from a white LED. Therefore, multiple LEDs per packages are necessary to deliver enough total flux output for general purpose illumination applications. Lighting efficiency in terms of lumens per watt is one of the criteria used to measure power saving by solid state lighting. The current lighting efficiency from LEDs is about 50 lumen/Watt. This offers about 70% power saving over an incandescent lamp, 50% over halogen light bulbs, and 40 % over compact fluorescent light (CFL) bulbs [35]. The lighting efficiency from solid state lighting is projected to reach 80-100 lumen/Watt by 2008.

#### **4.2 High Brightness LED Design and Fabrication**

A major breakthrough in solid state lighting has been the commercialization of GaN-based LEDs [37-41]. A typical single quantum well LED structure is shown in Figure 4.1. An n-GaN buffer layer is first grown on a sapphire substrate. On top of this buffer layer is an undoped InGaN quantum well between n-InGaN and p-AlGaN epilayers, followed by the top p-GaN layer. This structure must be partially etched to expose the n-GaN layer, as shown in Figure 4.2. A Ti/Al contact and a semitransparent Ni/Au contact are deposited on the n-GaN and p-GaN layers, respectively. The Ni and Au serve as current-spreading layers to overcome the low conductivity of the p-GaN material [42]. The wafer is usually cut into a rectangular shape, and molded onto a lead frame. Light can be coupled out through the top p-GaN layer and collected in an upward direction. Other coupling directions based on flip-chip packaging are also implemented. The device resistance of LED chips is limited by the n-GaN layer, and typical sheet resistance of the layer is 10-20  $\Omega$  per square, which limits the lateral dimensions of an LED device to about 300  $\mu\text{m}$  by 300  $\mu\text{m}$ .

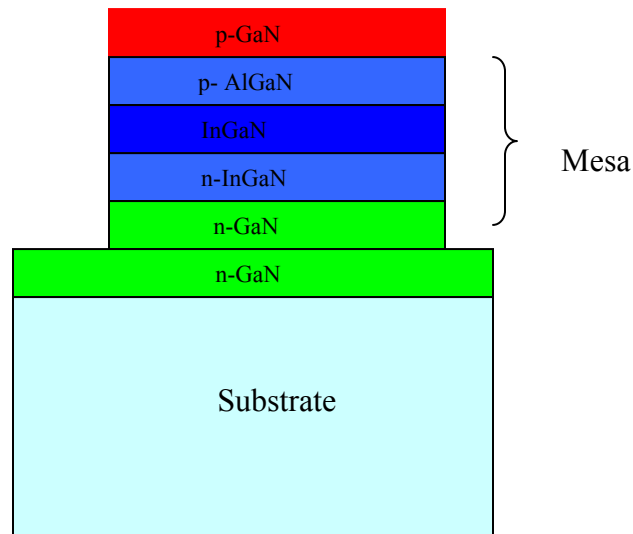


Figure 4.1 The GaN LED die structure

The final step is the LED lamp level design and packaging, in which a transparent epoxy dome is used to encapsulate the LED die. A small reflector cup attached to the die inside the epoxy is usually used to direct the light emission forward. Both die shape and epoxy geometry can be optimized to improve light extraction efficiency. In solid state light packages, multiple die are used to improve the overall lighting output. Multiple die with different colors can be packaged together, and the configuration geometry of those multiple die can be used to achieve the desired color mixing effect in optical display and illumination. Likewise, different spatial arrangements of LED lamps can be assembled together in traffic lighting and other outdoor lighting applications.

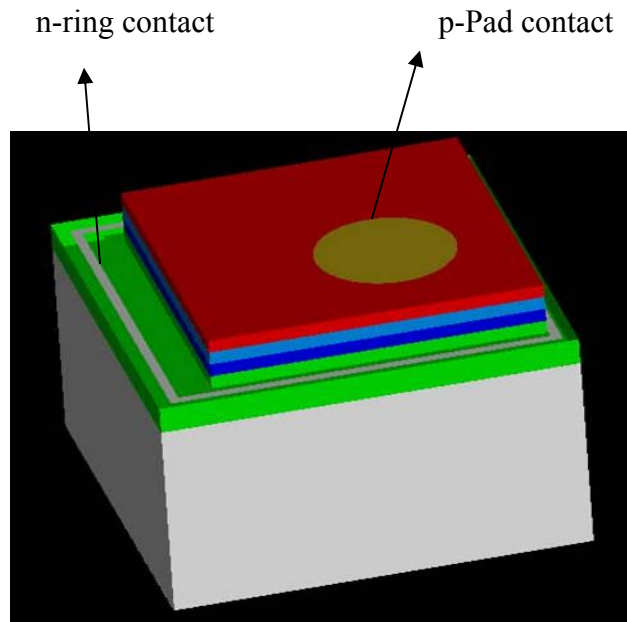


Figure 4.2 3-D plot of LED with electrode contacts.

Light extraction from an LED structure is an important criterion to evaluate the lighting performance of LEDs. The external quantum efficiency  $\eta_{\text{ext}}$  is a product of the optical extraction efficiency  $\eta_{\text{opt}}$  and internal quantum efficiency  $\eta_{\text{int}}$ . It is determined by the average number of extracted optical photons from an injected electron,  $\eta_{\text{ext}} = \eta_{\text{int}} \times \eta_{\text{opt}}$

The internal quantum efficiency  $\eta_{\text{int}}$  is a ratio of the number of generated photons to that of injected electrons, and it can also be determined by the fractions of the total current to the corresponding current producing the spontaneous recombination. The internal quantum efficiency is mainly determined by energy band structures and carrier transport properties, and the optical extraction efficiency  $\eta_{\text{opt}}$  is mainly limited by the geometrical structure of the LED device and package materials. The total internal reflections (TIR) of emitted photons from the active layer of LEDs at the interface for different materials is a critical factor that affects the optical extraction efficiency, where only light emitted within the critical angle  $\theta_c = \sin^{-1}(n_1/n)$  can be coupled outside the LED ( $n_1$  is the index of materials surrounding the LED, and  $n$  is the index of GaN material). And light absorption from semiconductor materials of the LED is another factor that affects the optical extraction efficiency. In the theory of waveguide optics, the TIR produces guided modes inside LED structures. Those guided modes partially survive the waveguide loss /material absorption and can escape through the side walls of LED chips in lateral directions. On the other hand, the leakage modes can escape relatively easily from the LED device structure in various directions.

To improve the light extraction efficiency of LEDs, LED structures have to be optimized using optical modeling techniques. Several methods of optical modeling have been developed, including both geometrical based ray tracing methods and wave optics methods. In the next chapter, we will focus on the theory of optical modeling.

# CHAPTER 5

## THEORY OF OPTICAL MODELING FOR HIGH BRIGHTNESS LEDS

### 5.1 Introduction to Optical Modeling

Many methods are reported to improve the optical extraction efficiency of LEDs. In conventional LED packages, the light can be partially extracted through the top p-GaN window. The light extraction efficiency was improved by applying a back reflector on the bottom of the substrate, and light emitting toward the substrate was folded back to avoid light loss from the LED. Another approach is to optimize the LED geometry such that more light escapes from the sidewalls of the LED [35]. Altering the direction of spontaneous light emission is also proposed in resonant-cavity LEDs (RCL) [43]. A surface textured or roughness method is used to overcome the total internal reflection by enhancing the light scattering [44]. These methods can be explained using the waveguide theory. To improve light extraction efficiency, waveguide structures in LEDs need to be altered such that more leakage modes are excited, and the guided modes are compressed in those LEDs with a special designed device geometry. For RCL, the vertical directions of LED spontaneous emission are enhanced by a resonant cavity, and lateral emissions are attenuated.

Optical modeling is critical to predict the optical extraction efficiency of high brightness LEDs. Considering the physical optics property, multi-mode light generation and propagation, and complex device structures of LEDs, rigorous modeling of LEDs is quite challenging. In general, optical modeling can be classified in several levels as shown in Figure 5.1:

Level 1 is the photonics/optoelectronics level, in which an optical photon is the elementary unit. Its optical wavelength and polarization direction can be analyzed from

the carrier transport, energy band structures. Level 2 belongs to physical optics, the optical source is described by electronic dipole radiations, which is a superposition of TE (s) and TM (p) regular plane waves or evanescent waves. Light propagations are governed by guided wave optics and diffractive optics play major roles [45]. Level 3 is based on geometrical optics, and optical ray tracing is the major tool to predict the optical phenomena, such as refraction, reflection, diffusing, scattering, and other optical lighting and imaging effects. Depending on different applications and design accuracy, LED modeling general requires Level 2, Level 3, or a combination of the two levels.

Optical ray tracing is most intensively used in modeling solid state lighting, especially in LED chip-level and lamp-level modeling. In LED die-level modeling, ray tracing and guided wave optics are both used to predict the lighting propagation and extraction behaviors. In this chapter, principles of geometrical optics based level 3 are first presented, and followed by introduction to level 2 using electronic dipole methods and wave optics.

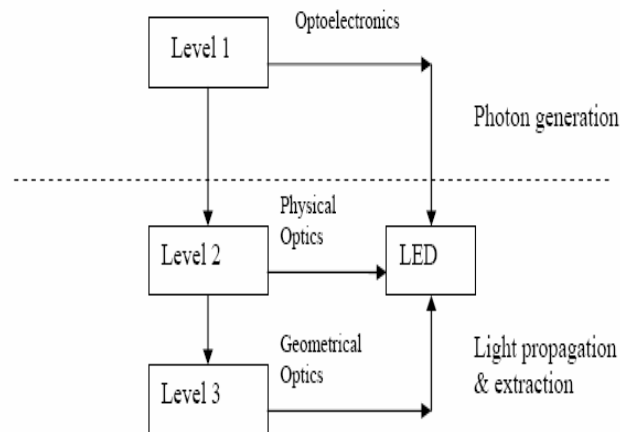


Figure 5.1 Three levels of optical modeling

## 5.2 Theory of Optical Ray Tracing

In geometrical optics, light is considered as a ray bundle. A ray is originated from a light source, and propagates along a straight path within the same medium such as air, and undergoes refraction and reflection at an interface of different media. At each of these interfaces, a ray splits one refracted ray and one reflected ray. The refracted ray prorogates in a forward direction and the reflected ray moves backward. Both refracted ray and reflected ray split a secondary refracted ray and a secondary reflected ray, to distinguish them from the parent ray, when they reach an interface at different media. These multiple reflections and refractions at different interface in an optical system will form a binary tree of rays as shown in Figure 5.2. In optical modeling for a LED, these secondary rays need to be traced. In general, this ray tree should be traced up to level 2 to guarantee a high accuracy. To carry out ray tracing, the optical power of refraction ray and reflection ray is calculated using Fresnel coefficients at each interface [46]. The total optical power at a specific surface can be obtained by accumulating powers of rays reaching this surface. Finally, the polarization effects are usually averaged in ray tracing

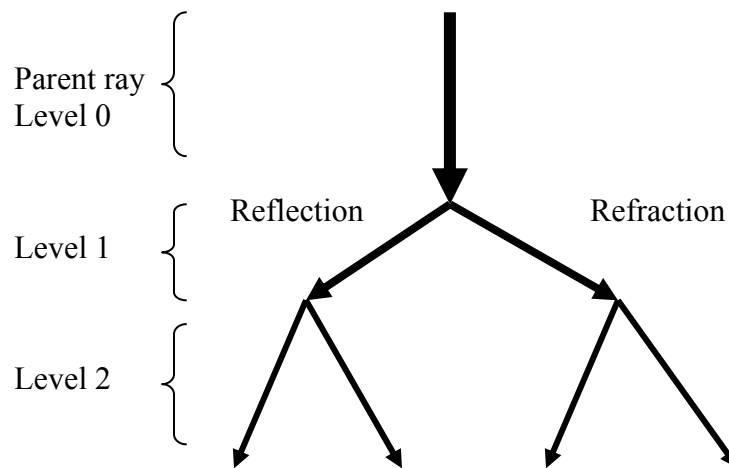


Figure 5.2 A binary tree of rays

A ray is defined by its starting point  $r(x,y,z)$  and a direction of propagation at a medium with a refractive index of  $n$ . A data structure in C to define ray is [47]:

```
typedef structure {
    float r[3];    /* starting point: x,y,z */
    float K[3];   /* propagation direction: kx, ky,kz */
    float n;      /* index of refraction */
} DEF_RAY;
```

The magnitude of a propagation direction vector  $K$  is  $n$ , the refractive index of a medium,  $|K|=n$ . By doing so, the propagation direction can be easily obtained when a refraction happens at an interface for different medium as shown in Figure 5.3. For a given ray in the direction  $K$  impinges on an interface, the vector  $K'$  after refraction, Snell's law can be expressed as:

$$K' = K + (p' - p)\sigma \quad (5.1)$$

where  $p = n \cos \theta$ , and  $\sigma$  is the surface normal of this interface,  $\theta$  is the angle of incidence; and  $p'$  and  $p$  are related by Snell's law:

$$p' = \pm \sqrt{p^2 + n'^2 - n^2} \quad (5.2)$$

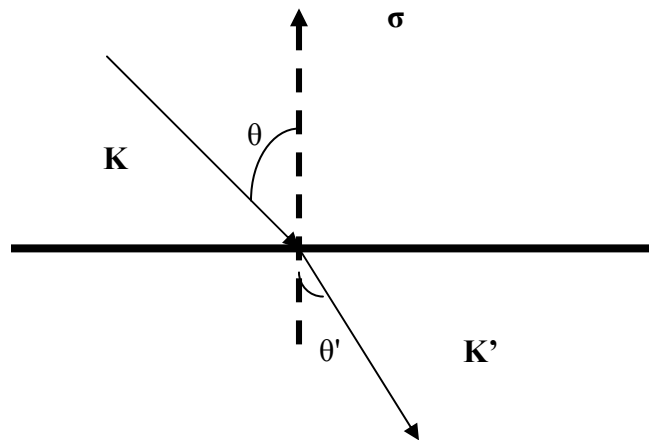


Figure 5.3 The propagation direction calculation

If the  $p'$  become a complex number, the ray is under total internal reflection. For refraction,  $p$  and  $p'$  maintain the same sign; for reflection,  $p$  and  $p'$  have different signs. It is easy to show that  $p=-p'$  for reflection. The surface normal  $\sigma$  can be calculated as follows:

$$\sigma = -\left\{ \frac{x}{R}, \frac{y}{R}, \frac{z}{R} - 1 \right\} \quad (5.3)$$

where  $R$  is the radius of a sphere centered at  $(0,0, R)$  defined as:

$$x^2 + y^2 + z^2 - 2Rz = 0 \quad (5.4)$$

The ray translation is given by

$$\begin{aligned} x' &= x + lk_x \\ y' &= y + lk_y \\ z' &= z + lk_z \end{aligned} \quad (5.5)$$

where  $d = nl$  is the actual distance along the ray. The ray translation in C code is described:

```
int j;
float l;
DEF_RAY *ray;

for (j=0; j<3; j++) r->r[j]=r[j]+l*ray->k[j];
```

When a ray reaches a surface separating different media, we need not only calculate the direction propagation, but also the intersection for the surface and ray. This intersection can be calculated using Eqs. (5.4) and (5.5):

$$(x + lk_x)^2 + (y + lk_y)^2 + (z + lk_z)^2 - 2R(z + lk_z) = 0 \quad (5.6)$$

$l$  is obtained by solving the above Equation:

$$l = \frac{C}{B \pm \sqrt{B^2 - AC}} \quad (5.7)$$

where B, C are given by:

$$B = k_z - (k_x x + k_y y + k_z z) c_r \quad (5.8)$$

$$C = (x^2 + y^2 + z^2) c_r - 2z$$

and  $c_r$  is the radius curvature,  $c_r = 1/R$ . In general, there are two intersections of the ray with a sphere. If the argument of the square root is zero, this means the ray is tangent to this sphere. If the ray can not intersect the sphere,  $l$  becomes a complex number. If a ray intersect a plane, i.e,  $c_r = 0$ , Eq.(5.7) is simplified:

$$l = -\frac{z}{k_z} \quad (5.9)$$

In essence, Equations (5.1) (5.5) and (5.7) are important to ray tracing. For each optical surface a ray encounters: first, the intersection point and direction of propagation are calculated, and then they are plugged into Eq. (5.5) to obtain a new state of the ray. This traced ray is traced again for next optical surface until it reaches either a detector or the image surface. In general, a launched ray experience two different actions: First, it translates through a uniform medium. Second, it experiences refraction and reflection at an interface between two different media. In some cases, the scattering also occurs at rough surfaces in which one incident ray become a scattered ray bundle distributed among a range of propagation directions as shown in Figure 5.4.

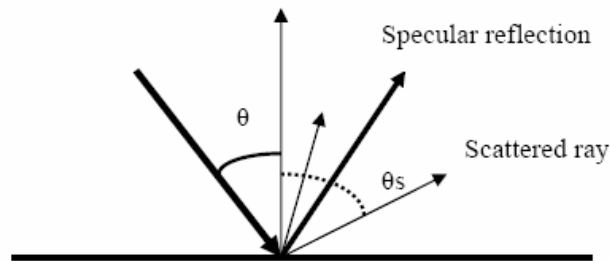


Figure 5.4 Picture of Ray scattering

To complete this introduction to ray tracing, we start to introduce light scattering at a rough surface. As discussed above, the Fresnel coefficients can be used for regular reflection and refraction at an interface without roughness. Both optical power and directions of light can be obtained using the Fresnel Equation and the Snell's law. For a rough surface, the light scattering needs to be taken into account. To model light scattering, we first introduce a function for light scattering, so called, Bi-directional Scatter Distribution Function (BSDF). The BSDF can be explained using Figure 5.3. Assuming light with power  $P$  incident on the rough surface with an incident angle of  $\theta$ , and the irradiance is defined as:

$$E(\theta, \varphi) = \frac{dP_i(\theta, \varphi)}{dS \cos \theta} \quad (5.10)$$

For scattered power  $P_s$  at a certain direction of  $\theta'$ , the radiance  $B$  is given by:

$$B(\theta_s, \varphi_s) = \frac{dP_s(\theta_s, \varphi_s)}{dS_s \cos \theta_s d\Omega} \quad (5.11)$$

With Equations (5.10) and (5.11), the BSDF is described as:

$$BSDF = \frac{B(\theta_s, \varphi_s)}{E(\theta, \varphi)} \quad (5.12)$$

It is also assumed that the scattered power linearly depends on the incident power, so the BSDF is the ratio of the radiance of a surface to the irradiance shining on the surface [48]. The total integrated scatter (TIS) is the total power scattered into a hemisphere above the surface divided by the incident power, and it is equivalent to integrate the BSDF over the hemisphere [49]:

$$TIS(\theta, \varphi) = \int_0^{2\pi} d\varphi' \int_0^{\pi/2} BSDF(\theta, \varphi, \theta', \varphi') d\theta' \quad (5.13)$$

Davis proposed a formula to relate the TIS and the surface roughness:

$$TIS = \left( \frac{2\pi\delta\Delta n}{\lambda} \right)^2 \quad (5.14)$$

where  $\delta$  is the RMS of the surface roughness,  $\Delta n$  is the refractive index difference between the surface and its ambient medium. There are several assumptions about the relation. Since the surface is clear and relatively smooth the scattering mainly occurs at directions close the specular direction, i.e, the regular reflection direction [49].

The accuracy of tracing scattered ray depends on models to describe the scatter property. There are several isotropic models to predict light scattering, for example the Lambertian model or the Harvey model. More rigorous models should be determined experimentally. The procedure to trace scattered rays is very similar to trace regular rays. Care must be taken to reallocate power scattered from the incident ray to scattered rays at a range of scattered angles based on corresponding scatter models.

### 5.3 Optical Modeling Based on Electronics Dipole Emissions

Optical modeling of LEDs based on electronic dipole emission is an important tool to predict the modification of spontaneous emissions of LEDs resulting from chip structure variations. One example is modeling RCLs using the dipole method [43,50]. The optical source is described by electronic dipole radiations, which is a superposition of TE (s) and TM (p) regular plane waves or evanescent waves. LED chip structures can be modeled as a multilayer planar system. The light extraction is analyzed by propagating these dipole radiations through the multilayer planar structure. Both regular plane waves and evanescent waves undergo reflections and transmissions, which can be modeled using a matrix method. Assuming the refractive index variation direction of this multilayer system is along the z direction, the LED device structure growth direction, the wavevector is defined as  $k_i = (k_{ix}, k_{iy}, k_{iz})$  as shown in Figure 5.5. If  $k_{ix}^2 + k_{iy}^2 = k_p^2 \leq k_i^2$ ; the waves are regular plane waves, otherwise, they become evanescent waves.

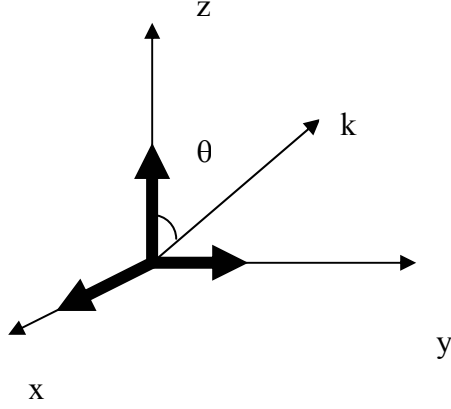


Figure 5.5 Dipole orientations

An electric dipole can be projected onto x, y, and z directions. The x component of a dipole emits TE light waves and both y and z components emit TM polarized waves. Using radiant, the power per unit solid angle to describe those dipole emissions, we have

$$\begin{aligned}
 \left(\frac{dP}{d\Omega}\right)^{(x)} &= \frac{3}{8\pi} \\
 \left(\frac{dP}{d\Omega}\right)^{(y)} &= \frac{3}{8\pi} \cos^2 \theta \\
 \left(\frac{dP}{d\Omega}\right)^{(z)} &= \frac{3}{8\pi} \sin^2 \theta
 \end{aligned} \tag{5.15}$$

where  $\theta$  is the off-normal emission angle relative to the z direction. The emission from dipoles propagates inside the LED multilayer structure, and undergoes reflections and transmissions. These optical propagations can be modeled using matrix methods for thin-film optics [51]. Two matrices are necessary to determine the light coupled out of the LED chip as shown in Figure 5.6. One is the effective matrix MB from all the layers below the source layer, and another is a matrix MA for all layers above the source layer. The overall reflection and transmission amplitude coefficients from matrix MB are  $r_1$  and

$t_1$ , respectively; and  $r_2$ ,  $t_2$  for matrix MA. The coupled out light amplitude from the bottom and top of a source layer are  $E_1$ ,  $E_2$ , respectively. Therefore we have

$$E_1(\theta) = \frac{t_1(r_2 A_+ - A_-)}{1 - r_1 r_2} \quad (5.16)$$

$$E_2(\theta) = \frac{t_2(r_1 A_- - A_+)}{1 - r_1 r_2} \quad (5.17)$$

where  $A_+$  and  $A_-$  represent the amplitudes of source terms in Eq. (4) propagating along  $+z$  and  $-z$  direction, respectively. The normalized outside power per unit solid angle and unit emitter, radiance is  $B(\theta)$ , and the extracted power on the specified side of LED chips is

$$P_{ext} = 2\pi \int B(\theta) \sin \theta d\theta \quad (5.18)$$

This method has been used to model the light extraction efficiency of RCL.

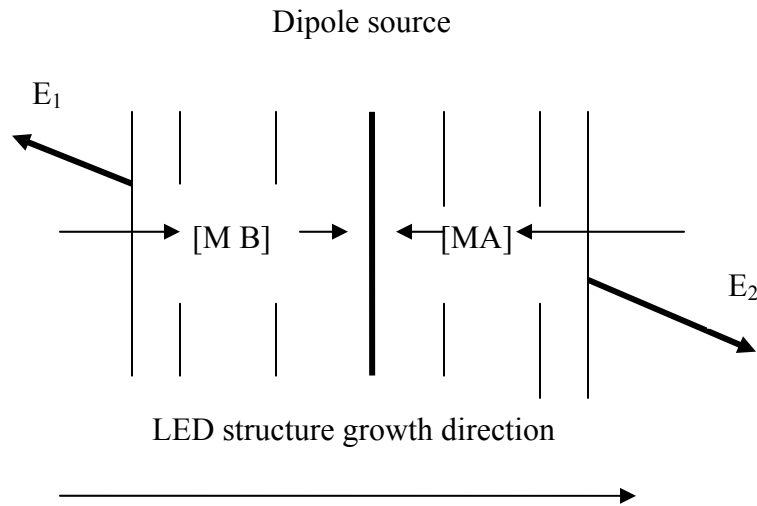


Figure 5.6 Sketch of multi-layers for transfer matrices

This method is first proposed by Benisty et al [50], which is the theory to unify dipole emission and the transfer-matrix method for thin film optics in an elegant framework. In this section, we first brief overview dipole emission for optical source, and then introduce the transfer matrix method.

### 5.3.1 Optical source is modeled by dipole emission

For an optical source or emitted embedded into a multi-layer planar structure, the source treated as dipole emissions causes an discontinuity of the electric field with a TE or TM polarization. Assuming light propagates along z axis, and  $E_b$  and  $E_t$  denotes electric field at bottom and top sides of the source dipole layer, respectively, we have:

$$E_t - E_b = \text{source dipole} \quad (5.19)$$

To represent the dipole emissions in Eq. (5.15) as a function wave vector, the wave vector in a medium layer i with refractive index  $n_i$  is:

$$\begin{aligned} (k_{i,x})^2 + (k_{i,y})^2 + (k_{i,z})^2 &= \left( \frac{2\pi n_i}{\lambda} \right)^2 \\ (k_p)^2 + (k_{i,z})^2 &= (k_i)^2 \end{aligned} \quad (5.20)$$

where  $k_{i,z} = k_i \cos \theta_i$  is a z component of  $k_i$ , and it can be used to represent both regular plane waves and evanescent waves;  $k_p$  is the in-plane component of  $k_i$ , which is constant throughout all interfaces of this multi-layer planar structure. Next, we need to normalize the power in Eq.(5.15) to corresponding amplitude forms, to represent dipole emission along +z and -z directions; we further assume that the source dipole is located at the plane  $z=0$ . The dipole along the z direction is a vertical dipole, and the in-plane dipoles, dipoles along the x and y directions, are horizontal dipoles. For horizontal dipoles, their amplitudes are given by the square root of the radiant power in Equation (5.15):

$$\begin{aligned}
Ah_+^x &= -\frac{1}{4} \sqrt{\frac{3}{\pi}} \\
Ah_-^x &= \frac{1}{4} \sqrt{\frac{3}{\pi}} \\
Ah_+^y &= -\frac{1}{4} \sqrt{\frac{3}{\pi}} \frac{k_{i,z}}{k_i} \\
Ah_-^y &= \frac{1}{4} \sqrt{\frac{3}{\pi}} \frac{k_{i,z}}{k_i}
\end{aligned} \tag{5.21}$$

where + and – subscripts correspond to +z and –z directions respectively. Similarly, for vertical dipoles, we have:

$$Av_+^z = Av_-^z = \frac{1}{2} \sqrt{\frac{3}{2\pi}} \frac{k_p}{k_i} \tag{5.22}$$

The signs in Equation (5.21) are defined by considering boundary conditions of Maxwell equations [43]. In terms of TE or TM polarizations, their amplitudes are:

$$\begin{aligned}
\text{TE mode:} \quad A_+(TE) &= Ah_+^x \\
A_-(TE) &= Ah_-^x
\end{aligned} \tag{5.23}$$

$$\begin{aligned}
\text{TM mode:} \quad A_+(TM) &= Ah_+^x + Av_+^z \\
A_-(TM) &= Ah_-^x + Av_-^z
\end{aligned} \tag{5.24}$$

If we use a 2 x 1 vector to represent electric fields propagating along +z and –z directions:

$$\text{TE mode:} \quad E^s(z) = \begin{pmatrix} E_+^s \\ E_-^s \end{pmatrix} \tag{5.25}$$

$$\text{TM mode: } E^p(z) = \begin{pmatrix} E_+^p \\ E_-^p \end{pmatrix} \quad (5.26)$$

Eq. (5.19) can be extended as:

$$\begin{pmatrix} E_{t+}^s \\ E_{t-}^s \end{pmatrix} - \begin{pmatrix} E_{b+}^s \\ E_{b-}^s \end{pmatrix} = \begin{pmatrix} A_+(TE) \\ A_-(TE) \end{pmatrix} \quad (5.27)$$

$$\begin{pmatrix} E_{t+}^p \\ E_{t-}^p \end{pmatrix} - \begin{pmatrix} E_{b+}^p \\ E_{b-}^p \end{pmatrix} = \begin{pmatrix} A_+(TM) \\ A_-(TM) \end{pmatrix}$$

Eq. (5.27) represents the relation between electric field adjacent to each side of the dipole layer and the source dipole. The remaining problem is how to relate the outside electric field to the electric field next to the dipole layer as show in Figure 5.5. The field adjacent to the dipole layer can be obtained with the transfer matrix method from the outside field  $E_1$  or  $E_2$ , and transfer matrices MA and MB :

$$\begin{pmatrix} b_{11} & b_{12} \\ b_{21} & b_{22} \end{pmatrix} \begin{pmatrix} 0 \\ E_1(\theta) \end{pmatrix} = \begin{pmatrix} E_{b+} \\ E_{b-} \end{pmatrix} \quad (5.28)$$

$$\begin{pmatrix} a_{11} & a_{12} \\ a_{21} & a_{22} \end{pmatrix} \begin{pmatrix} E_2(\theta) \\ 0 \end{pmatrix} = \begin{pmatrix} E_{t+} \\ E_{t-} \end{pmatrix} \quad (5.29)$$

Equations (5.28) and (5.29) apply to both TE and TM polarizations, the polarization notations are omitted; however, transfer matrices are different for these two polarizations. The transfer matrix method can be used to calculate these transfer matrices. From Eqs.(5.27-5.29), we have the following expressions for outside electric fields  $E_1$  and  $E_2$ , respectively:

$$E_1(\theta) = \frac{-a_{21}A_+ + a_{11}A_-}{-b_{22}a_{11} + b_{12}a_{21}} \quad (5.30)$$

$$E_2(\theta) = \frac{-b_{22}A_+ + b_{12}A_-}{-b_{22}a_{11} + b_{12}a_{21}} \quad (5.31)$$

It is easy to obtain Eq. (5.16) and (5.17) from Eqs.(5.30) and (5.31) [51-52].

### 5.3.2 Transfer matrix method

To calculate these transfer matrices, we need to know the refractive index and thickness for each layer. Yeh [51] and Pedrotti *et al.* [52] provide an efficient way to compute the transfer matrix M for a multiplayer structure. Figure 5.7 shows the multilayer structure, we have:

$$\begin{pmatrix} E_{0,+} \\ E_{0,-} \end{pmatrix} = \begin{pmatrix} m_{11} & m_{12} \\ m_{21} & m_{22} \end{pmatrix} \begin{pmatrix} E_{s,+} \\ E_{s,-} \end{pmatrix} \quad (5.32)$$

$$M = D_0^{-1} \left( \prod_{i=1}^N D_i P_i D_i^{-1} \right) D_s \quad (5.33)$$

For TE wave, the matrix D is:

$$D_i = \begin{pmatrix} 1 & 1 \\ n_i \cos \theta_i & -n_i \cos \theta_i \end{pmatrix} \quad (5.34)$$

For TM wave,

$$D_i = \begin{pmatrix} \cos \theta_i & \cos \theta_i \\ n_i & -n_i \end{pmatrix} \quad (5.35)$$

The propagation matrix P<sub>i</sub> is defined as:

$$P_i = \begin{pmatrix} \exp(j\varphi_i) & 0 \\ 0 & \exp(-j\varphi_i) \end{pmatrix} \quad (5.36)$$

and  $\varphi_i$  is given by:

$$\varphi_i = \frac{2\pi n_i d_i}{\lambda} \cos \theta_i \quad (5.37)$$

where  $d_i$  is the thickness, and  $\theta_i$  is the ray angle in layer  $i$ .

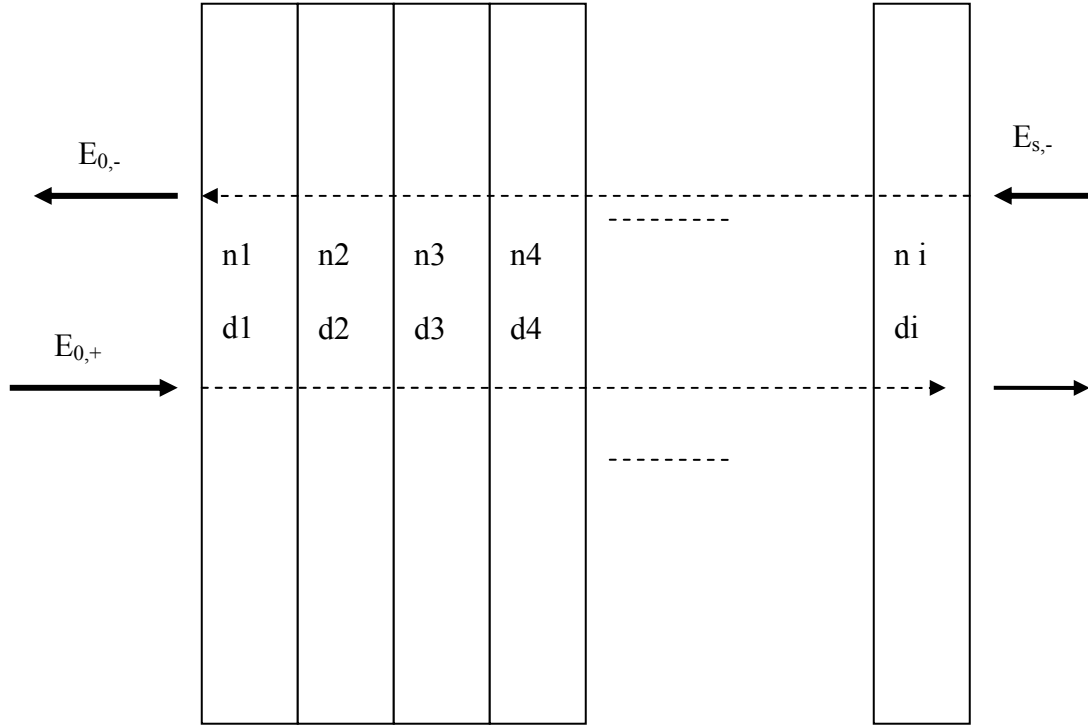


Figure 5.7 Diagram of a multi-layer structure

In conclusion, we outline some guide lines to applying the techniques described above to rigorously model the light extraction efficiency of LED with a micro-cavity. In this type of LED, light emission has a high directionality, i.e., the direction of light is close to on-axis, and there are a few resonant modes in a micro-cavity. As a result, the spontaneous emission from the LED is altered by the micro-cavity. In a typical LED the light emission roughly follows Lambert's law, i.e, the radiant intensity in far field can be approximated by a cosine function of the direction angle ,  $B(\theta)=B_o \cos \theta$ . In this case, there are many rays propagate along the plane of multi-layers of a LED, i.e., in-plane propagation as shown in Figure 5.8. From a guided wave point of view, there are many

guided modes that propagate transversely. This electronic dipole method can not treat these modes without special care [50]. On the other hand, geometrical optics based ray tracing fails to model micro-cavity effects. However, the simulation result with the ray tracing method is very accurate to predict performance of LEDs without a micro-cavity [35].

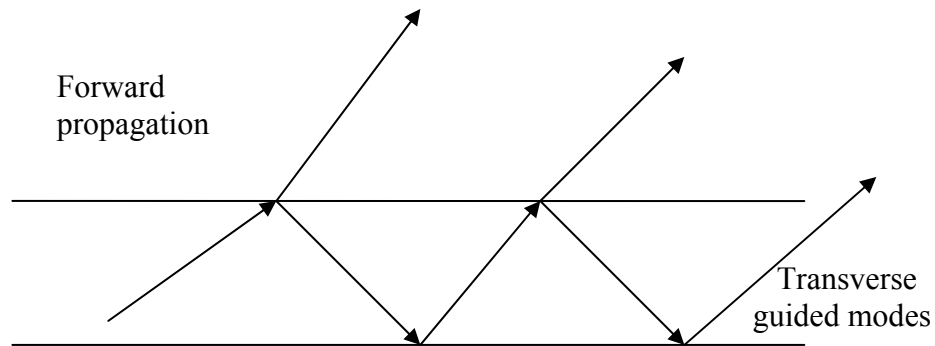


Figure 5.8 Light in-plane propagation

In this chapter, a detailed ray tracing method is described, and a procedure to code a ray tracing program is outlined. The theory of tracing scattered rays at a rough surface is also presented. This geometrical optics based ray tracing can show how ray translation in a uniform medium and ray refraction, reflection and possible scattering at a surface, i.e., an interface at different media. The electronic dipole method for an optical source modeling and a transfer matrix method for light propagation is also outlined. For a regular LED without a micro-cavity, the optical ray tracing can model the light extraction efficiency of the LED with a high degree of accuracy. The electric dipole and transfer matrix method can efficiently model a LED with a micro-cavity.

## CHAPTER 6

### OPTICAL MODELING FOR HIGH BRIGHTNESS LED

#### 6.1 Introduction

In this chapter, guided wave approach is introduced. LED is modeled as a multi-layer waveguide structure. Light emitted from the LED is classified into guided modes and leakage modes. Based on this approach, a rhombic die is shown to be more efficient than regular square die. The back reflector at the bottom of the LED dies effectively doubles the LED die thickness and increases its light extraction efficiency. Replacement of a back reflector with a diffractive reflection grating further improves the light extraction efficiency.

#### 6.2 Guided Wave Approach on LED Modeling

The LED die can be modeled as two types of optical waveguides as shown in Figure 6.1: the first waveguide consists of the single or multiple quantum well (MQW) active region and n-layer and p-layer of the LED. Optical waves are generated in this waveguide structure, which we call an **active waveguide**. The second waveguide structure consists of a sapphire or SiC substrate and medium surrounding its sidewalls, defined as a **passive waveguide**; and its main function is to support some optical waves generated in the active waveguide. The refractive index of a substrate is lower than that of active waveguides.

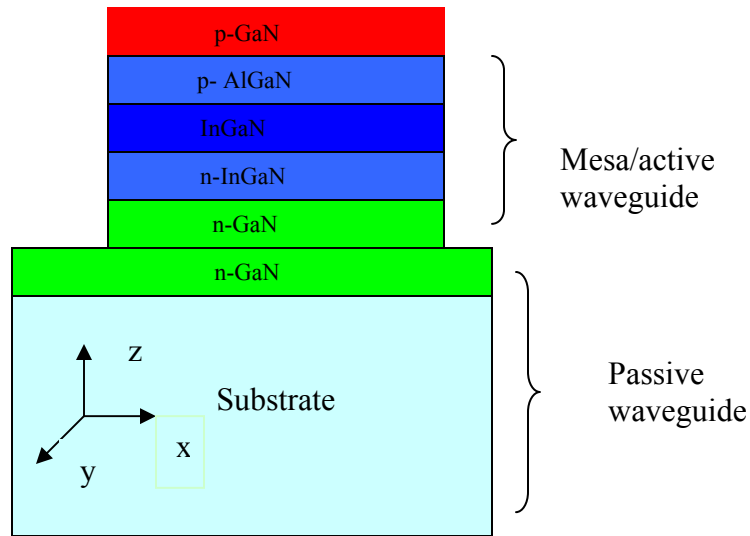


Figure 6.1 Waveguide structure of a GaN LED

In general, the active waveguide consists of several layers of thin films, several microns in thickness, and several hundreds of microns in the lateral dimensions. It can be treated as a slab waveguide. Also, it acts as an optical photon generator. On the other hand, the thickness of the passive waveguide is usually several hundreds of microns, with the same lateral dimension as the active region. Based on the above analysis, it is believed that the passive waveguide will make the main contribution to light extraction from the LED die. The active waveguide will play an important role in light generation and extraction, which is the key factor to improve the brightness of LEDs.

Photons generated through MQW in the active region from electron-hole pair recombination can be modeled as multi-mode optical waves with a certain mode distribution. Among these multi-mode optical waves, longitudinal wave represents those modes propagating along the  $z$  direction, i.e, the direction of layer variation of a LED

structure, and the transverse mode wave propagates along the x and y directions, lateral directions.

In the nitride heterostructure of LEDs, the guiding layer of the active region consists of the InGaN/GaN MQW. The p-GaN, p-AlGaN layer, n-GaN layer, and n-InGaN layer surrounding the active region form the cladding region. This waveguide does absorb blue light because of the high absorption from the InGaN layer.

Since the x, y dimension, the lateral direction, is fairly large relative to the z dimension, the transverse mode of optical waves can be solved using the slab wave guide theory. Because the absorption of InGaN is strong at the blue wavelength region, the transverse modes, which are defined as propagating along the (x y) plane, hardly reach outside the waveguide. As a result, the transverse optical wave almost makes no contribution to the light coupling and extractions.

Actually, the mesa region above the substrate in a LED die is the region of the active waveguide, which is responsible for photon generations and coupling into its surroundings. Alteration of the lateral shape of the mesa results in almost no change to light emission because this part is modeled as a slab waveguide. The passivation layer coated on the mesa will influence the structure of the active waveguide. Since this passivation layer is transparent to blue light, its restriction on the light extraction efficiency comes from the interface TIR, which forces photons to undergo multiple passes through the absorption region of the active region of a LED and decreases the extraction efficiency of the light.

Both the longitudinal modes, which are mainly leakage modes, and transverse modes of photon emissions in the active waveguide region contribute to light coupling

outside the LED die. Longitudinal modes are first considered. The forward propagation of longitudinal modes is coupled out of the active waveguides through a p-pad of an electrode on the top of LEDs. The backward parts of those longitudinal modes go through the sapphire substrate, the passive waveguide, and are then sustained as either a guided wave or leakage mode wave in the passive waveguide. The sapphire is transparent to blue light, and the material property of the medium surrounding the substrate changes the passive guide structures and light extraction efficiency. Most of the longitudinal modes are leakage modes, and their extraction efficiency can be improved by applying a micro-resonant cavity [43].

Because of the refractive index difference for different layers along the z-direction (longitudinal direction), the coupling efficiency of light from the active waveguide to the passive waveguide is restricted by the refractive index difference of n-GaN ( $n=2.42@460\text{ nm}$ ) and the sapphire substrate ( $n=1.78@460\text{ nm}$ ). The critical angle is calculated as  $\theta_c=47.5$  degrees. Beyond this angle, the light from the active waveguide is trapped inside the active guides, which undergoes the process of re-absorption; and parts of the trapped light can escape the active waveguide in the forward direction through the p-pad.

Some of the light transmitted into the passive wave-guide becomes guided modes, and the rest are leakage modes. If angles are all defined in the active region, the angles below which the guided modes occur is

$$\text{Sin}(\theta_s) = (N_{\text{sub}}^2 - N_{\text{sur}}^2)^{0.5} / N_p \quad (6.1)$$

where  $N_{\text{sub}}$  and  $N_{\text{sur}}$  denote the refractive index of the substrate of sapphire and its surrounding medium, respectively.  $N_p$  is the refractive index of the n-layer. If the air is used as the surrounding medium, then  $\theta_s = 37.5$  degrees. In other words, the light inside the n-layer above the substrate with different incident angles between 0 to 37.5 degrees becomes guided modes; that from 37.5 to 47.5 degrees becomes leakage modes in the passive waveguide, respectively. Accordingly, the light with incident angle beyond 47.5 degrees is total internal reflected back to the active waveguide.

Because the refractive index of the n-layer and substrate both are fixed, the coupling efficiency from the active waveguide to the passive waveguide is pretty much unchangeable, i.e., only a light cone defined by the angle of 47.5 degrees can be coupled into the passive waveguide layer.

### **6.2.1 Backward Light Extraction through the Passive Waveguide**

Most of the light coupled into the passive waveguide becomes guided waves, with a half cone angle of 37.5 degrees (assuming air is the cladding layer surrounding to the passive waveguide); and light within a half cone angle from 37.5 to 47.5 degrees belongs to the leakage modes. In other words, about 70% of the light coupled from the active waveguide is guided wave, and the rest of light is leakage wave. The ratio of guided wave to leakage wave can be changed by either alternating the refractive index of the surrounding medium or changing shape of the die, for example, from a standard square die to a non-square die.

Assuming the material of the passive waveguide is transparent to blue light, most of the light coupled into the passive waveguide can be extracted by optimizing

geometry and refractive index matching of the substrate and its surrounding medium, for example, the spherical or dome shaped encapsulation of the LED. This is especially true for flip-chip LED packaging. In standard LED packaging, the die-attached epoxy at the bottom of the substrate is highly absorptive.

First, we study light extraction from guided modes in backward propagation light. In the case of no reflector at the bottom of the substrate, the guided mode wave in the passive waveguide propagates in the waveguide until reaching the bottom of the substrate, and light is absorbed by the layer of a die-attached epoxy. The absorption decreases the light extraction efficiency.

By putting a back reflector at the bottom of the substrate, the guided mode optical wave is reflected back to avoid strong absorption at the bottom of the substrate, and light extraction efficiency is increased. However, the reflector folds back the light path and forces light to re-enter the active waveguide region and is absorbed again by the active layer. The reflected light at the reflector needs to be further diffracted by a grating, and the diffracted light can escape from the passive waveguide before it enters the active region to undergo re-absorption. Also, more energy of the light can be shifted into leakage modes from guided modes by changing the structure of the passive waveguide structure, for example, the refractive index of the surrounding medium and the shape of the waveguide structure.

For leakage modes in backward propagation light, the substrate and the die-attached epoxy play major roles. The highly absorptive die-attached epoxy layer sitting at the bottom of a substrate has little influence on the leakage modes because the light of leakage modes hardly strikes the bottom of the substrate.

To couple the leakage mode as much as possible, the interface between the substrate and its surrounding medium needs to be designed better, for example, tapered sidewalls, or textured surfaces of LEDs can improve light extractions of leakage modes. LEDs with regular geometry can redirect some leakage modes into the active waveguide.

### **6.2.2 Forward Light Extraction from the Active Waveguide Layer**

Because of the reflection at the interface between the n-layer and the sapphire substrate, the backward light gets reflected from this interface and joins the forward emitted light from the active region of a LED. This combined forward light strikes on the semi-transparent contact, the p-pad, where the total internal reflection (TIR) occurs (assuming the refractive index of the transparent contact is about 1.5). About 38% of the forward light with a half angle of 38 degrees, determined by the TIR, can be coupled out through the semi-transparent contact. The TIR occurs again at the interface between transparent contact and a passivation layer on the top of the LED.

By applying the waveguide theory, functions of the active waveguide and passive wave guide can be seen clearly. The different contributions to light extraction from guided modes and leakage modes can be analyzed. The passivation layer and medium surrounding the die are analyzed through the total internal reflection. It is shown that the reflector only influences on these guided modes, has little effect on these leakage modes in the passive waveguide. The couple efficiency of the leakage mode is mainly determined by the interface between a substrate and its cladding layer, i.e., its surrounding medium.

### 6.3 Improve Light Extraction Using a Back Reflector and Thick Substrates

A typical bare LED die consists of p-GaN layer, n-GaN layer, and an active region with AlGaIn and InGaIn. InGaIn has strong absorption at blue wavelength, and both p-GaN layer and n-GaN layer also absorb blue light with relatively small absorption coefficients compared to InGaIn. The semitransparent contact Ni/Au sitting on the top p-GaN layer of the LED die absorbs about 10% light. A Ti/Al contact was deposited on the n-GaN layer after the etch process. The whole device structure is grown on the sapphire substrate. All of these above layers form the absorption region of blue light. The problem is that light generated at the active region has to experience multiple passes and reflections inside these absorption regions before coming out of the LED die, as shown in Figures 6.2 and 6.3

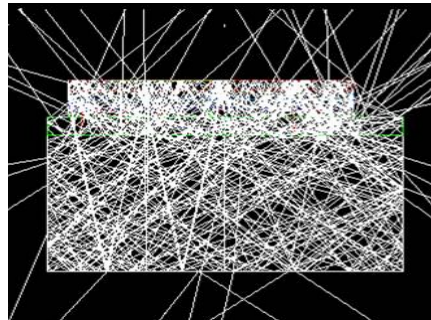


Figure 6.2 Geometrical ray tracing of a LED die.

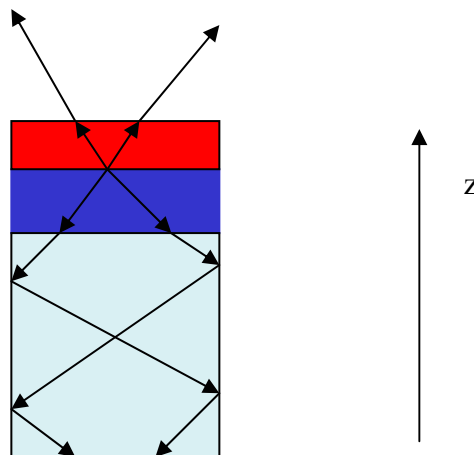


Figure 6.3 Light forward propagation and backward propagation in a LED

At the bottom of the LED substrate, there is a highly absorptive layer of the die-attached epoxy, which absorbs some light propagating toward the LED bottom, especially those guided modes. One way to increase light extraction efficiency is to use a thick substrate. With the thick substrate, more light is able to escape the LED chips through its sidewalls before reaching the bottom of the substrate. On the other hand, the light extraction efficiency of the LED can be increased by coating a metal mirror, such as an aluminum reflector at the bottom of the sapphire substrate, to avoid light absorption by the die-attached epoxy. Another function of the back mirror is that it folds the light path and equivalently doubles the actual thickness of the LED die experienced by backward emissions from the LED active region, which also increases light extraction efficiency. As a result, the light extraction efficiency is increased more than 20% by applying this back reflector. The substrate thickness and mirror reflectivity can be optimized using our model.

#### **6.4 Optimizing LED Die geometries to Increase Light Extraction Efficiency**

Light extraction efficiency can be further improved by modifying of the geometry of a LED die. One example is to change the square die shape into a rhombus with the same die area. This changes the waveguide structure and increases the amount of leakage mode light, and more light comes out of the sidewalls, which reduces the light absorption inside a LED. The LED die can be modeled as a three-dimensional waveguide. It can be further decomposed into two slab waveguides in the  $x$  and  $y$  direction, respectively. Figure 6.4 shows the waveguide structure for a LED. A slab wave guide theory can be used to model this 3-D wave guide [53].

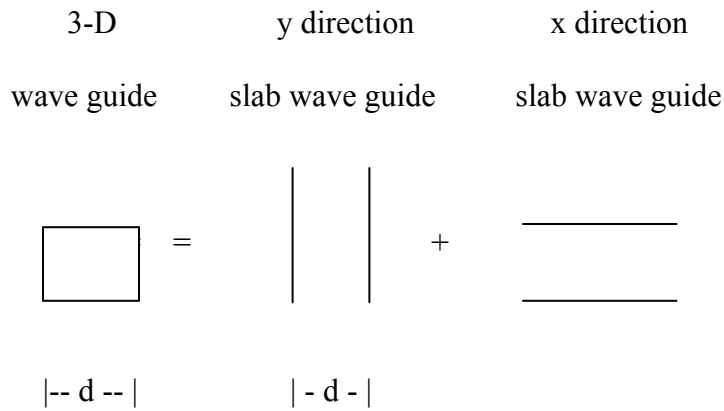


Figure 6.4 Decomposition of 3-D wave guide into slab wave guides

It has been shown that the number of guided modes the slab waveguide can support is proportional to  $d$ , the confined dimension of the waveguide. For the same die area, the confined dimension of a rhombus die,  $h = d (\sin\theta)^{0.5}$ . This reduced dimension of the rhombus waveguide will decrease the number of guided modes and consequently increase the number of leakage modes. It can be shown that, for the same die area, the total sidewall area of a rhombic die is  $1/(\sin\theta)^{0.5}$  times that of a square die as shown in

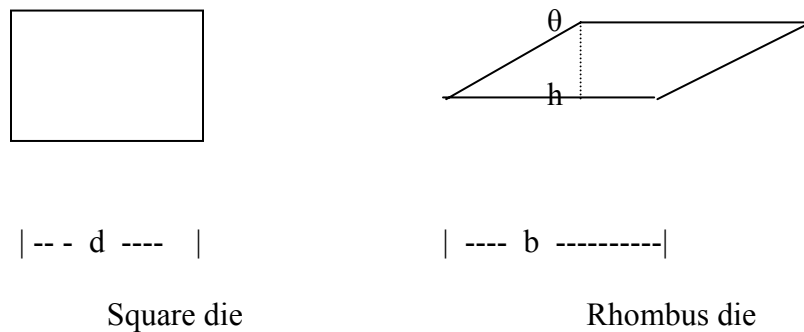


Figure 6.5 Dimension of square die and rhombus die

Figure 6.5. Compared to a regular squared die, the rhombic die has relatively large area of sidewalls. As a result, more light can come out of the sidewalls for a rhombus-shaped

die. This is also confirmed by our optical simulation method. Simulation results are listed in Table 2. A single quantum-well blue LED with a peak wavelength of 460 nm from Ref. 54, is used in this simulation. The refractive index of GaN is 2.42, 2.54 for InGaN and 2.33 for AlGaN ; the absorption coefficient of an InGaN active region is  $1.25 \mu\text{m}^{-1}$  [54]. The numbers inside brackets in the table are normalized to LEE of a squared die.

Table 2. Light extraction efficiency (LEE) for different die shapes of LEDs

Die shape	LEE w/ reflector	Light from top of a die	Light from bottom	Light from side walls	LEE increase w/ reflector
Circular	8.1% [.95]*	38.9%	9.7%	51.4%	24%
Square	8.5% [1]	37.0%	11.1%	51.9%	27%
Hexagon	9.3% [1.09]	34.2%	10.4%	55.4%	31%
Rhombus 1 (45°/135°)	10.3% [1.21]	33.3%	13.0%	53.7%	32%
Rhombus 2 (30°/150°)	10.3% [1.21]	33.8%	14.9%	51.3%	35%

## 6.5 Utilizing Reflection Grating to Increase Light Extraction Efficiency

The back reflector method can improve the light extraction efficiency; however, the reflected light from the aluminum reflector re-enters the absorption region consisting of p-GaN, n-GaN, active layers and a semi-transparent contact, and some of the reflected light will be trapped in this absorption region and experience re-absorption.

To solve this problem, we apply diffractive optics technology and use a reflective grating or other types of diffraction gratings to replace the aluminum reflector. The reflective grating can be fabricated using binary digital optics technology. The light shining on this grating will be diffracted and blazed into directions other than the direction of mirror reflection. As a result, most of the diffractive light will become leakage mode and come out of the sidewalls without entering the absorption region. The

reflective grating can be approximated using a two-level phase grating with a phase of 0 or  $\pi$ ; the period of the grating is  $d$  as shown in Figure 6.6.

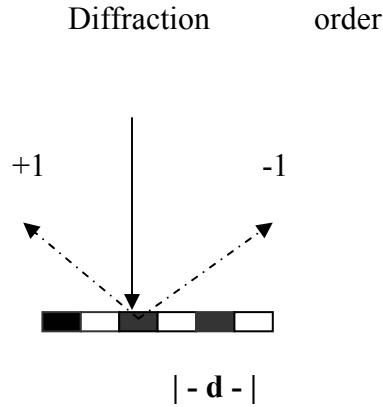


Figure 6.6 Reflective binary phase grating

It can be shown that the diffraction efficiency of zero order will be zero, and even orders of diffraction also disappear [45, 54]. Moreover, the diffraction efficiency for odd orders is

$$\eta = 4 / (n\pi)^2 \quad (6.2)$$

where  $n$  represents the diffraction order. The first-order diffraction efficiency is 40%, which means +1 and -1 orders will account for 80% of the total light, and their diffraction angle can be determined as

$$\sin\theta = \lambda / d \quad (6.3)$$

where  $\lambda$  is the wavelength of light at the grating medium. This grating will diffract incident light into leakage modes, and this diffracted light hits the sidewalls and comes out of the die without re-entering the absorption regions.

The reflective grating can also be implemented using a blazed grating, and the majority of diffracted light can be shifted to high orders other than the zero order. Also, the grating can be either 1-D or 2-D. Figure 6.7 shows a blazed reflection grating. This

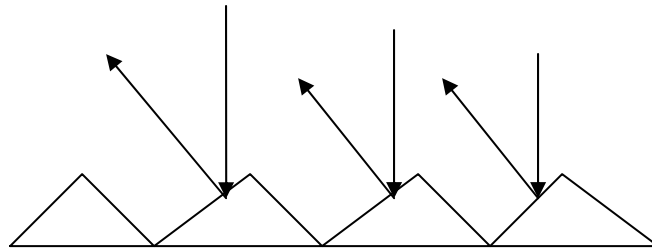
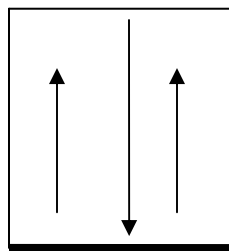


Figure 6.7 Blazed reflections grating

grating can re-direct light away from the on-axis direction. As a result, most of light can be coupled outside from side-walls of a LED as shown in Figure 6.8.



(a)

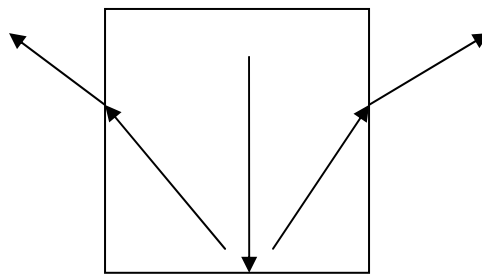


Figure 6.8 LED light coupling: (a) with a back reflector, (b) with a reflection grating

In this chapter, a guide wave approach is used to analyze the light extraction from a LED. Several methods are proposed to improve the light extraction from a LED, which include the LED die shape optimization, a back reflector approach and a diffraction grating application. Since the light extraction efficiency can not be directly verified by experimental results, our simulations can only be calibrated by some analytical results. Published light extraction efficiency of GaN based LEDs is about 10%. Our simulation is in good agreement with these published results [55].

## CHAPTER 7

### OPTICAL MODELING FOR A DUAL WAVELENGTH LED

#### 7.1 Dual Wavelength LED Device Structure

Current white LEDs schemes are either based on a short wavelength LED pumping a longer wavelength phosphor (phosphor converted LED) or discrete red, green and blue chips coupled with light mixing technology (RGB LED). Each of these schemes has particular advantages, however, there are also some disadvantages associated with each as well. The blue LED / YAG:Ce scheme is the most common type of white LED and are the cheapest of the white LED solutions. However, the color rendering quality of the light from a LED/YAG device is typically low due to deficiencies in the power spectrum especially of the red wavelengths. Various phosphors can be employed in similar white LED schemes to produce more red light, however the efficiency of the device is decreased due to the increase in Stokes shift associated with pumping a longer wavelength phosphor. Additionally there is no functionality for dynamic control of the power spectrum for a phosphor converted (PC) LED such as with a RGB LED. The power spectrum of a RGB LED can be controlled by varying the relative intensities of the red, green or blue sources, which allows for two things: dynamic sources and color correction over the lifetime of the device. In addition, RGB LEDs are more expensive than PC LED due to the requirement for more advanced packaging. Another concern for RGB LEDs is proper mixing of the light because the sources must have some finite distances between them which affect the lighting uniformity at the far field of the light source.

To solve these problems, first, new RGB phosphors need to be developed to improve color mixing and performances; second, new LED structure design and improved efficiency to couple light into phosphor should be initiated to overcome these

problems [56,57]. A dual wavelength LED structure, with an emission pair of 400 nm/460 nm or a pair of 460 nm/530 nm, the shorter wavelength  $\lambda_1 \sim 400$  nm or 460 nm emission for efficient pumping of the blue/green phosphor, and the longer wavelength  $\lambda_2 \sim 460$  nm or 530 nm emission matching to the red phosphor, is proposed to improve the color mixing of the solid state lighting. This dual wavelength InGaN LED can be fabricated using a tunnel junction, and three terminals are used to independently electrical control of the emission intensity for each wavelength.

A dual wavelength LED with two emission wavelengths at 470nm and 535 nm is used as a reference design as shown in Figure 7.1 [58]. This LED includes two separate PN junctions, and each junction has an active region of InGaN MQWs. These two sets of different MQWs have different mole fractions of indium in InGaN materials, which dictate two different emission wavelengths. These two electrically independent PN junctions are integrated into a single vertical heterostructure.

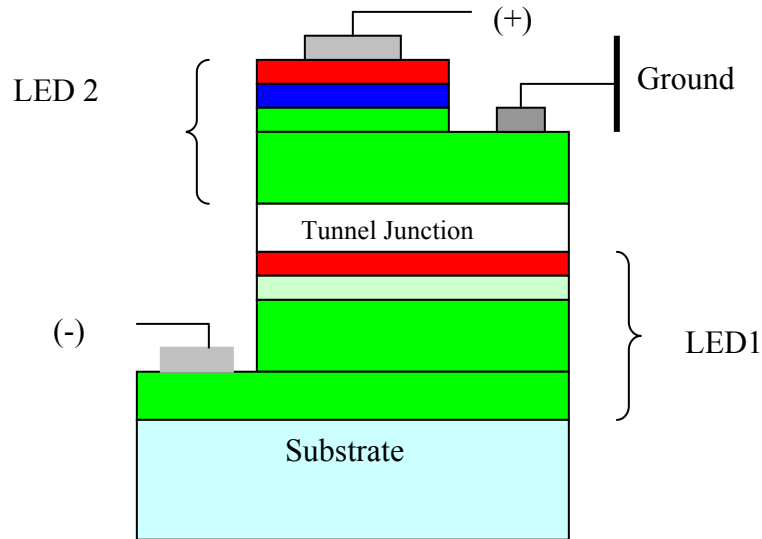


Figure 7.1 Structure of a Dual wavelength LED

This dual wavelength LED was grown by organo-metallic vapor deposition on sapphire substrate as depicted in Figure 7.1. The first PN junction of the LED with a peak emission wavelength about 530 nm, is grown on a n-GaN buffer layer. A 40 nm thick n-InGaN layer is deposited on the top of this buffer layer. Its active region is four In<sub>x</sub>Ga<sub>1-x</sub>N MQW's with GaN barriers, with the well width of 3 nm, the barrier width 5 nm. Followed layers are, a 30 nm thick layer of p-Al<sub>0.07</sub>Ga<sub>0.93</sub>N for electron blocking, and a 100nm thick p-GaN layer.

A p<sup>++</sup>/n<sup>++</sup> GaN tunnel junction (TJ) in this device separates the two PN junctions, and make it three-terminal device. Another function of the TJ is it servers as a lateral current spreading layer for the PN junction underneath. Figure 7.2 shows the detailed configuration of this TJ. A 200 nm thick n-GaN cap layer is grown on the top of this TJ. On the top of the TJ is the second LED, where a similar MQW structure of

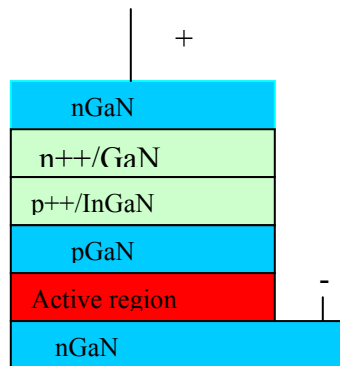


Figure 7.2 A Tunnel junction

In<sub>x</sub>Ga<sub>1-x</sub>N is grown, and the indium component is designed to emit a peak wavelength of 470 nm. The device structure of the second LED is very similar to the first one, except for a heavily doped p-GaN cap layer with 50nm thickness for the electrical contact in the second LED. The P- contact using a thin layer of combinations of Ni and Au on the top of the dual wavelength LED, and the Ni and Au also serve as a current spreading layer to improve the conductivity of p-GaN. Because both Ni and Au absorb some light, the P-

contact is also called a semitransparent P-Pad. To fabricate the electrical contact for the common ground and n-contact, two steps of etch are required. The first etch, for the n-contact, need to reach the n-GaN buffer layer on the top of substrate, and the second etch, for the common ground should reach the n-GaN layer above the TJ.

Finally, a Distributed Bragg Reflection grating (DBR) pairs may be applied to this dual wavelength terminal device to form a micro -resonant cavity as shown in Figure 7.3. The first DBR can be positioned between the n-GaN buffer layer and n-InGaN layer of the bottom LED. The second DBR is just below the p-GaN layer of the top LED. If it works, this proposed micro-cavity may triple the light extraction efficiency [50]. In the meantime, it can shape optical beams from both LEDs to improve the color mixing, which is important to light coupling to phosphors. The technical challenge to design and fabricate DBRs for a dual wavelength LED is that the small refractive index difference (contrast) of materials current available to GaN based LEDs, limits the stop bandwidth of

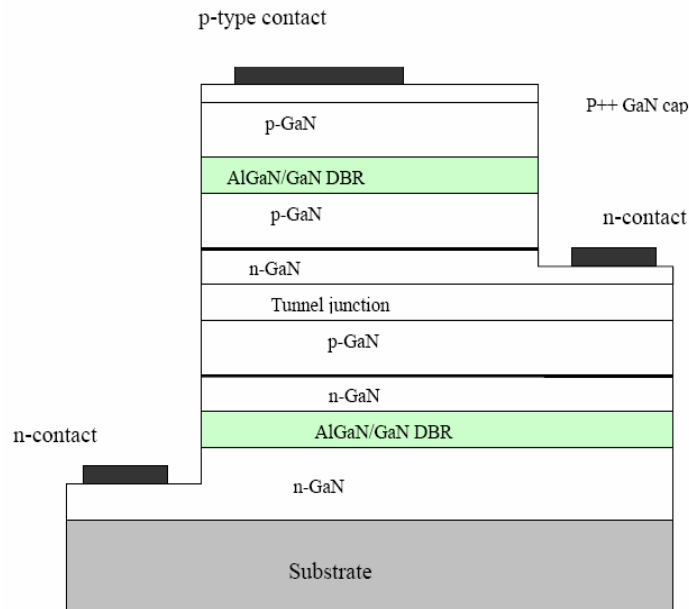


Figure 7.3 A micro-cavity for a Dual wavelength LED

DBRs. As a result, current available DBRs, such as AlGaIn/GaN, fail to cover the broad spectrum of dual wavelength LEDs. So, the alternative to DRB pairs maybe the application a back reflector at the bottom of the sapphire substrate, and light is coupled out from the top of this dual wavelength LED through the semitransparent of p-Pad.

## 7.2 Overview of Tunnel Junction for GaN Based LEDs

Electron tunneling results from a quantum mechanical phenomenon from the wave nature of electrons [59]. When an electron wave is incident with energy less than the energy barrier height, there is a probability that this electron can penetrate this energy barrier, and the penetration depth depends on the barrier height. Figure 7.4 shows a rectangular barrier with potential height of  $V$ , and thickness of  $d$ . For an electron wave with energy  $E_v$ , the tunneling probability is given by[59]:

$$T(E_v) = \left[ 1 + \frac{V^2 \sinh^2(kd)}{4E_v(V - E_v)} \right]^{-1} \quad (7.1)$$

$$k = \sqrt{\frac{2m(V - E_v)}{\hbar^2}}$$

where  $m$  is the effective mass of an electron,  $\hbar$  is the plank constant. The tunnel probability is high for very thin barriers. For arbitrary shape of potential barriers, a numerical solution can be obtained by approximating the potential barrier with multiple sub-potential layers, each sub-potential layer can be treated as a constant potential layer. Equation (7.1) is used to calculate the tunneling probability for each of these constant potential barriers.

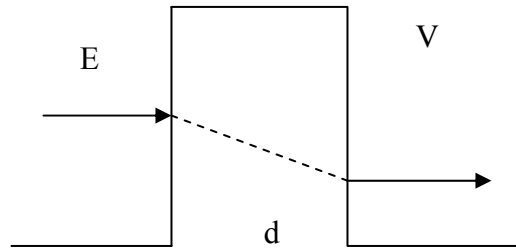


Figure 7.4 Potential barrier for a TJ

In semiconductor materials, carriers can be generated by band to band tunneling when a strong electric field presents, for example, the electric field greater than 10MV/cm [60]. For a reversed biased, heavily doped, thin pn junction, if the electron penetration depth is larger than the depletion width of this pn junction electrons at valence bands at p side can penetrate into conduction bands at n side to become free carriers. This is the so called tunneling junction.

The uses of a tunnel junction (TJ) in III-Nitride LEDs have been demonstrated recently [61]. The reverse biased TJ is to improve the lateral current spreading. With a TJ, n-GaN can be used to replace p-GaN as a top cap layer. Commonly, a so called semi-transparent p-Pad is usually applied on the top of p-GaN to overcome the low conductivity of p-GaN In conventional LEDs. The n-GaN has much higher conductivity, about 100 times, compared to p-GaN , and the reverse biased TJ supplies holes to p-GaN adjacent to the active region through lateral current. As a result, the application of n-GaN top contact layer can improve the current spreading of the LED, and increase light extraction by avoiding using semitransparent contact. Another benefit of using a TJ is the simplification of the LED fabrication process because n-GaN can be used as to implement both the top p-contact and lower n-contact as shown in Figure 7.2.

The TJ usually is fabricated using heavily doped p<sup>++</sup>/n<sup>++</sup> either InGaN/GaN or GaN/GaN bi-layer. One example use an InGaN/GaN bi-layer with layer thicknesses of 15 nm/30nm [62]. The p-type doping Mg level is about  $1 \times 10^{20} \text{ cm}^{-3}$ , and n-type doping Si level is about  $6 \times 10^{19} \text{ cm}^{-3}$  for this tunneling junction. This TJ is incorporated into a resonant cavity LED with violet light emission. The resonant cavity of this LED uses two pairs of DBRs: the top one is a SiO<sub>2</sub>/HfO<sub>2</sub> above the TJ, and the bottom one is an AlGaIn/GaN DBR grown on a GaN buffer layer. A TJ in the second example is fabricated using a GaN/GaN layer with layer thicknesses of 10nm/10 nm. The p<sup>+</sup> GaN layer is doped with  $3 \times 10^{19} \text{ cm}^{-3}$  of Mg; the averaged Si doping level in the n<sup>+</sup> GaN layer is about  $10^{20} \text{ cm}^{-3}$ . A n-GaN is grown on the top of this TJ to replace the conventional p-GaN as a

top contact layer. One disadvantage of the TJ is its large forward voltage, about 1 volt higher than that of a conventional LED because the TJ add a series resistance to the LED. However, the overall optical power of a LED is claimed to double compared to the conventional LED with a top semitransparent p-Pad [61 ].

### **7.3. Distributed Bragg Reflection Grating (DBR) for High Brightness LEDs**

A resonant cavity using a pair of distributed Bragg Reflection gratings (DBR) can be used to improve light extraction efficiency of LEDs by altering the distribution of spontaneous emissions. For GaN based LEDs applications, there are two types of DBRs. Dielectric DBR and semiconductor based DBR. The dielectric DBR using HfO<sub>2</sub>/SiO<sub>2</sub> offers a large bandwidth of reflection about 80 nm because the relative large difference of refractive indexes between HfO<sub>2</sub> and SiO<sub>2</sub> [62]. However, this type of DRB requires more complicated processing. An AlN/GaN based DBR has a medium reflection bandwidth of about 45 nm because the large index of refraction contrast [63]. A in situ grown DRB is an AlGaIn/GaN, and this type DBR is easy to be integrated into a LED structure; however, its limited reflection bandwidth is only about 20 nm [64-66]. The low contrast of refractive indices of AlGaIn/GaN makes the grating a fuzzy DBR. Here, we will focus on the semiconductor based DBRs.

The application of DBR to a single wavelength emitter has been successful. Its application to a dual wavelength remain technical challenge because it is difficult to fabricate a DBR to cover the wide optical spectrum of a dual wavelength device, and it is also difficult to select corresponding resonant modes for both peak wavelengths.

#### **7.3.1 Theory of distributed Bragg reflection grating (DBR)**

Here, we will briefly summarize the concept of a DBR. A DBR structure can be viewed as a periodic structure of layered medium, with two different refractive indices  $n_1$  and  $n_2$ , which is shown in Figure 7.5. A Bloch wave is generated when a plane wave is launched into such a periodic structure. If the Bloch wave falls in forbidden bands, this periodic medium can totally reflect the incident light. By proper engineering refractive indices, a high reflective reflector for a certain selected spectral regions can be realized. For normal incident light into a quarter-wave stack of a DBR, this implies:

$$\begin{aligned}
 kn_1d_1 = kn_2d_2 &= \frac{1}{2}\pi \\
 k &= \frac{2\pi}{\lambda} = \frac{\omega}{c}
 \end{aligned}
 \tag{7.2}$$

where  $\omega$  is the center angular frequency of the reflection band. The reflection bandwidth is given by [51]:

$$\Delta\omega = \omega \frac{4}{\pi} \sin^{-1}\left(\frac{|n_1 - n_2|}{n_1 + n_2}\right) = \omega \frac{2}{\pi} \frac{\Delta n}{n}
 \tag{7.3}$$

with  $n=(n_1+n_2)/2$ . It is the refractive index different that determines the reflection bandwidth, and this reflection bandwidth is very critical for DBR application in high brightness LEDs. The reflectivity of a DBR is another factor to evaluate DBR performance. This reflection also depends on the number of grating periods in a DBR. Next, we are going to show how to determine the reflectivity of a DBR based on the transfer matrix method in details

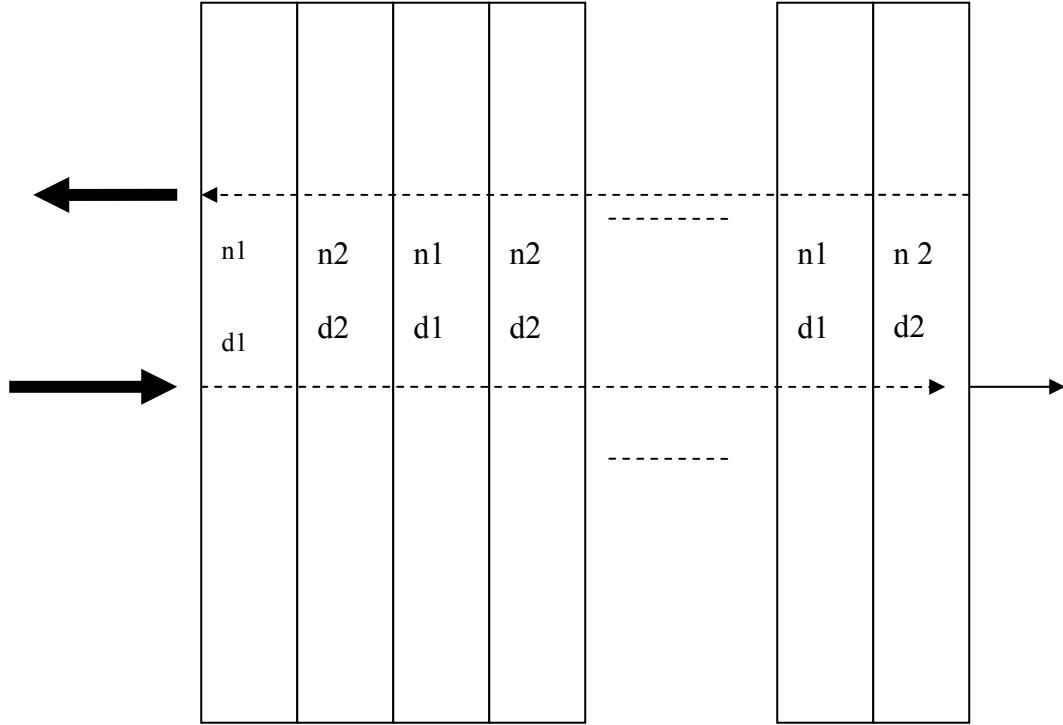


Figure 7.5 A DBR diagram

The theory of DBRs can be easily explained using transfer matrix method, which has been detailed in Chapter 5. The light output and input to this DBR can be related by the following equations for a multilayer structure

$$\begin{pmatrix} E_{0,+} \\ E_{0,-} \end{pmatrix} = \begin{pmatrix} m_{11} & m_{12} \\ m_{21} & m_{22} \end{pmatrix} \begin{pmatrix} E_{s,+} \\ E_{s,-} \end{pmatrix} \quad (5.32)$$

$$M = D_0^{-1} \left( \prod_{i=1}^N D_i P_i D_i^{-1} \right) D_s \quad (5.33)$$

For TE wave, the matrix D is:

$$D_i = \begin{pmatrix} 1 & 1 \\ n_i \cos \theta_i & -n_i \cos \theta_i \end{pmatrix} \quad (5.34)$$

For TM wave,

$$D_i = \begin{pmatrix} \cos \theta_i & \cos \theta_i \\ n_i & -n_i \end{pmatrix} \quad (5.35)$$

The propagation matrix  $P_i$  is defined as:

$$P_i = \begin{pmatrix} \exp(j\varphi_i) & 0 \\ 0 & \exp(-j\varphi_i) \end{pmatrix} \quad (5.36)$$

and  $\varphi_i$  is given by:

$$\varphi_i = \frac{2\pi n_i d_i}{\lambda} \cos \theta_i \quad (5.37)$$

where  $d_i$  is the thickness, and  $\theta_i$  is the ray angle in layer  $i$ . Moreover, the transfer matrix  $M$  for this DBR can be simplified as:

$$M = D_0^{-1} G^N D_s \quad (7.4)$$

where

$$G = (D_1 P_1 D_1^{-1})(D_2 P_2 D_2^{-1}) \quad (7.5)$$

and subscripts 0 and s represent the incident medium and the substrate of the DBR, respectively. For a quarter-wave stack DBR, Eq. (5.37) becomes:

$$\varphi_i = \frac{\pi}{2} \cos \theta_i \quad (7.6)$$

By definition, the reflection coefficient of a DBR is:

$$r(\theta_o) = \left[ \frac{E_{0,-}}{E_{0,+}} \right]_{E_{s,-}=0} = \frac{m_{21}}{m_{11}} \quad (7.7)$$

The reflectivity of a DBR is a function of the refractive indices, the layer thicknesses of the two different materials of the DBR, the number of periods, the incident angles, and the different polarizations. The bandwidth of reflection of a given DBR is determined by the reflective index contrast of this DBR.

### 7.3.2 Optical modeling for AlGaIn/GaN DBR and AlN/GaN DBR

A quarter-wave stack AlGaIn/GaN DBR with 35 quarter-wave pairs is simulated first. To design and simulate a DBR, an accurate estimate of the refractive indices is required. The refractive index of GaN for different wavelengths is calculated based on a method presented in Ref. 51, and the refractive index of  $\text{Al}_{0.34}\text{Ga}_{0.66}\text{N}$  is given by Refs. 67 and 68. Layer thicknesses for AlGaIn and GaN are 41 nm and 38 nm, and refractive index at 390 nm are 2.39 and 2.58, respectively. To show how the incident medium change performance of this DBR, we take two different media, the air and the GaN material. In each of two incident media, a normal incident light is first simulated, and then an incident angle is changed to 5, 10 degrees without altering this DBR structure. For a normal incidence, the DBR performance is independent of polarization states of light; however, the light polarization can affect performances of a DBR when a light incident angle is off the normal. These simulation results are shown in Figure 7.6 through Figure 7.8. For a normal incident, the center of reflection bandwidth is at 390 nm, and the bandwidth is about 15 nm. An incidence with a slanted angle will shift the reflection center to a short wavelength region for the incident medium of GaN.

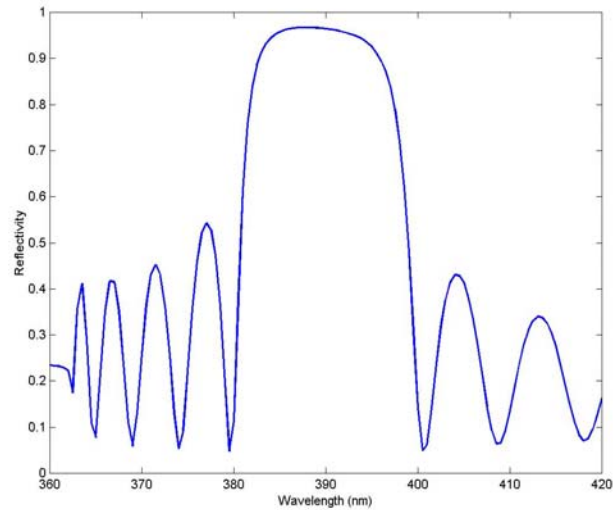


Figure 7.6(a) Reflection of AlGaIn/GaN DBR with normal incident light from air

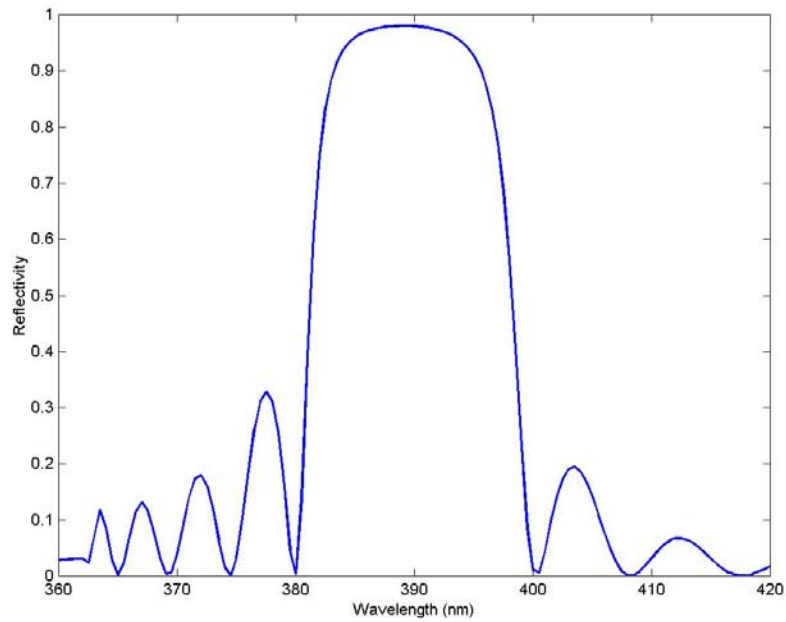


Figure 7.6(b) Reflection of AlGaIn/GaN DBR with normal incident light from GaN

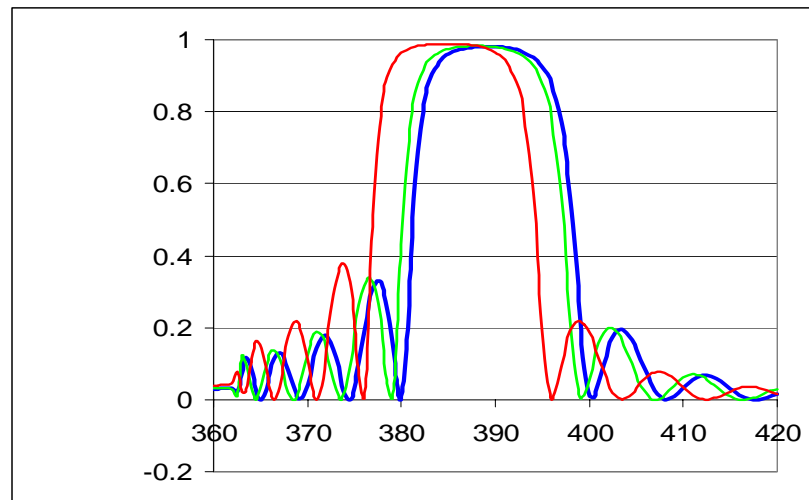


Figure 7.7 Reflections of AlGaIn/GaN DBR with incident light from GaN: the blue curve represents normal incident; the green curve, 5 degree slanted incident; the red curve, 10 degree slanted incident

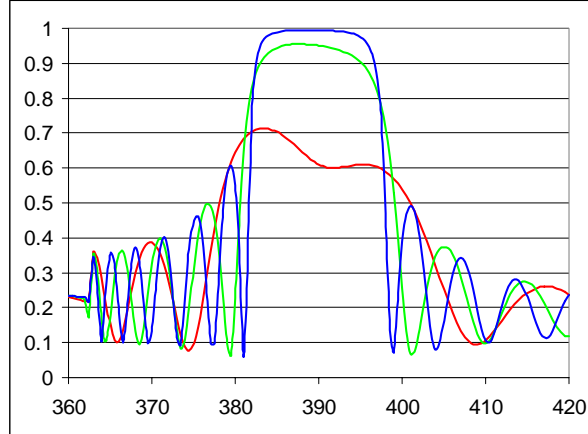


Figure 7.8 DBR reflection versus the number of pairs. Red curve represents 20 pairs; Green curve, 35 pairs ; Blue curve, 50 pairs

We also vary the number of the quarter-wave pairs in the DBR with light incidence from air, the center reflectivity is plotted for different quarter-wave pairs as shown in Figure 7.8. Because the refractive index contrast in an AlGaIn/GaN DBR is small, this type DBR has a limited reflection bandwidth. A DBR with AlN/GaN pairs with large refractive index contrast can increase the reflection bandwidth. To simulate this type DBR, we also need to determine the refractive indices of AlN and GaN. In our simulation, the refractive index of AlN is 2.16, and the refractive index variations versus different wavelengths is only taken into account [63]. Figure 7.9 shows the reflection plot for this DBR.

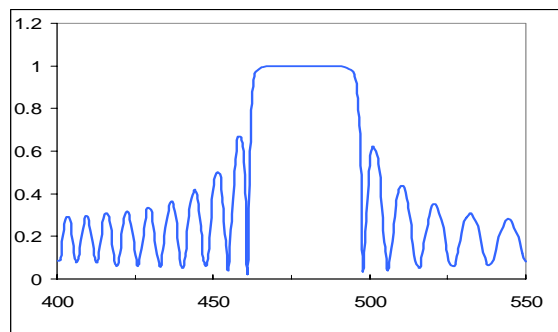


Figure 7.9 Reflection plot for an AlN/GaN DBR

## 7.4 Optical Simulations for A Dual Wavelength LED

To perform optical modeling for a Dual wavelength LED, we first need to design InGaN/GaN MWQs for two emission wavelengths. Detailed electric band structures calculation for MWQs requires many fabrication dependent parameters, which is beyond the scopes of this thesis. Here, the following approximation is used to estimate the peak emission wavelength [59-60]:

$$\lambda_p = \frac{1240}{1.89x + 3.42(1-x) - 3.8x(1-x) + E_{1e} + E_{1h}} nm \quad (7.8)$$

where  $x$  is a low mole fraction of indium of  $\text{In}_x\text{Ga}_{1-x}\text{N}$ .  $E_{1e}$  and  $E_{1h}$  denote the first conduct band level and first valence band level of the corresponding MWQs, respectively. Also, a Gaussian distribution is assumed for the optical emission spectrum:

$$\rho(\lambda) = \frac{1}{\sqrt{2\pi}\sigma} \exp\left[-\frac{(\lambda - \lambda_p)^2}{2\sigma^2}\right] \quad (7.9)$$

The optical spectrum from the dual wavelength LED in Figure 7.1 can be determined using Equation (7.8) and (7.9), which is plotted in Figure 7.10 for MWQs with the well width of 3nm. The  $\text{In}_{0.23}\text{Ga}_{0.77}\text{N}/\text{GaN}$  is used to estimate blue emissions and  $\text{In}_{0.33}\text{Ga}_{0.67}\text{N}/\text{GaN}$  for green emission.

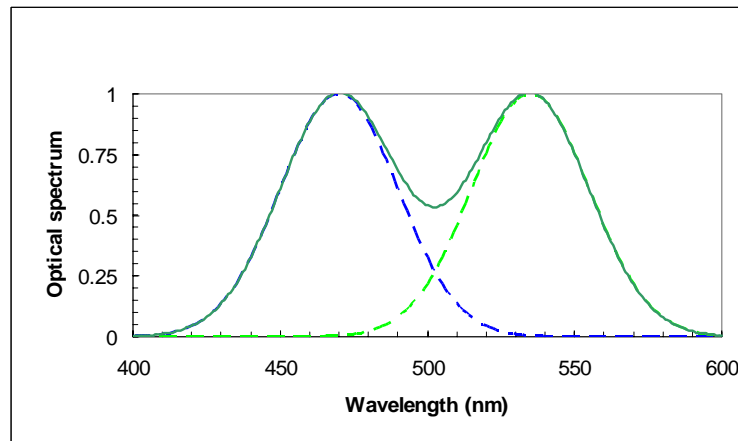


Figure 7.10 Optical spectrum plot for a dual wavelength LED

Refractive indices for bulk materials of GaN, AlGa<sub>x</sub>N, InGa<sub>x</sub>N, and InGa<sub>x</sub>N/GaN MWQs in a Dual wavelength LED are required for optical simulations. First, refractive indices for these bulk semiconductor materials are investigated. Second, an overview of refractive index estimations for InGa<sub>x</sub>N/GaN MWQs is present.

Brunner *et al* have extensively studied the refractive index of Al<sub>x</sub>Ga<sub>1-x</sub>N [67]. They first calculated the refractive index from transmission measurements, and then use the Adachi model [69] and some fitting parameters to interpolate these experimental data. Finally, the refractive index dispersions can be plotted versus different Al<sub>x</sub>Ga<sub>1-x</sub>N. The refractive index is estimated as:

$$n(\lambda)^2 = a(x) \left( \frac{hc}{\lambda E_g} \right)^{-2} \left[ 2 - \left( 1 + \frac{hc}{\lambda E_g} \right)^{1/2} - \left( 1 - \frac{hc}{\lambda E_g} \right)^{1/2} \right] + b(x) \quad (7.10)$$

The energy band gap  $E_g$  for Al<sub>x</sub>Ga<sub>1-x</sub>N can be determined by [60,67]:

$$E_g(x) = 6.13x + 3.42(1-x) + 1.3x(1-x) \quad (7.11)$$

Coefficients  $a(x)$  and  $b(x)$  are from Ref. 67

$$\begin{aligned} a(x) &= 3.17\sqrt{x} + 9.98 \\ b(x) &= -2.20x + 2.66 \end{aligned} \quad (7.12)$$

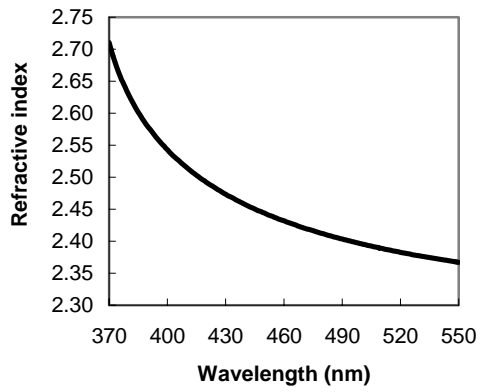
Similarly, the refractive index calculations for In<sub>x</sub>Ga<sub>1-x</sub>N also use Equation (7.10); however, use the following formula to obtain energy band gaps [71]:

$$E_g(x) = 1.9x + 3.4(1-x) + 1.0x(1-x) \quad (7.13)$$

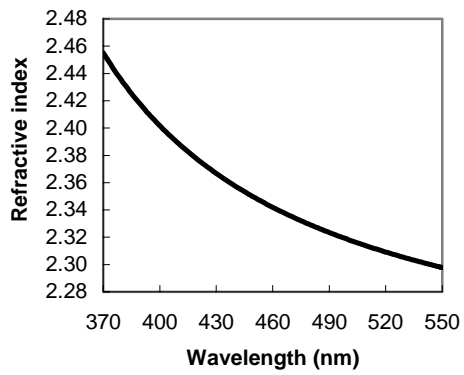
and  $a(x)$ ,  $b(x)$  are given by:

$$\begin{aligned} a(x) &= 53.57x + 9.31(1-x) \\ b(x) &= -9.19x + 3.03(1-x) \end{aligned} \quad (7.14)$$

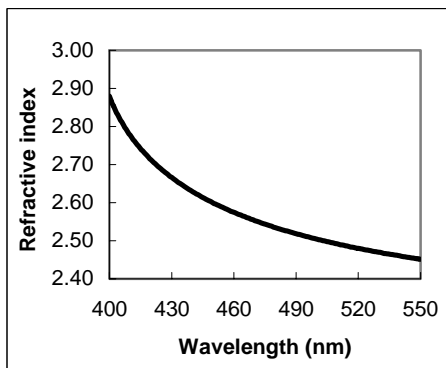
Using Equations (7.10-7.14), refractive indices for GaN, Al<sub>x</sub>Ga<sub>1-x</sub>N and In<sub>x</sub>Ga<sub>1-x</sub>N can be estimated, some results are shown in Figure 7.11.



(a)



(b)



(c)

Figure 7.11 Refractive index plots: (a) GaN, (b)  $\text{Al}_{0.3}\text{Ga}_{0.7}\text{N}$ , and (c)  $\text{In}_{0.1}\text{Ga}_{0.9}\text{N}$

Mandy et al developed a comprehensive model to calculate the complex index of refraction of InGaN/GaN quantum well [70]. The complex dielectric function is calculated the QW, which include both quantum effects and continuum contributions. Moreover, continuum contributions are determined by weighting the InGaN well and GaN barrier continuums above the barrier energy without QW effect. If the complex dielectric function is described as  $\epsilon(\lambda) = \epsilon_1(\lambda) + i\epsilon_2(\lambda)$ , then, the refractive index  $n$  and the extinction coefficient  $\kappa$  can be given by:

$$n(\lambda) = \left( \frac{\left[ \frac{\epsilon_1(\lambda)^2 + \epsilon_2(\lambda)^2}{2} \right]^{1/2} + \epsilon_1(\lambda)^2}{2} \right)^{1/2} \quad (7.15)$$

$$\kappa(\lambda) = \left( \frac{\left[ \frac{\epsilon_1(\lambda)^2 + \epsilon_2(\lambda)^2}{2} \right]^{1/2} - \epsilon_1(\lambda)^2}{2} \right)^{1/2} \quad (7.16)$$

Based on the above equations and detailed numerical calculations for MQW structures, the refractive index and the extinction coefficient were plotted for different In compositions and wavelengths. However, the refractive index for InGaN/GaN MWQs given by this model is below general accepted values. So the refractive index of MWQs is estimated by that of bulk materials. Before starting to do optical simulations, we list refractive indices for AlGaIn InGaIn GaIn, and InGaIn/GaIn MQWs in Table 3.

Table 3 Refractive indices of GaN, InGaIn and AlGaIn for simulations

<b>Wavelength</b>	<b>GaN</b>	<b>AlGaIn</b>	<b>InGaIn (bulk)</b>	<b>InGaIn(MWQ)</b>
<b>470 (nm)</b>	<b>2.42</b>	<b>2.37</b>	<b>2.55</b>	<b>2.79</b>
<b>530 (nm)</b>	<b>2.38</b>	<b>2.33</b>	<b>2.47</b>	<b>2.6</b>

The absorption coefficient is another factor to be considered in the optical simulation. In the InGaN active region of green light emission around 530nm, the absorption coefficients at wavelengths 460 nm and 530 nm are  $1.8 \mu\text{m}^{-1}$  and  $1.6 \mu\text{m}^{-1}$ , respectively; in the active region of blue emission around 460 nm ,  $1.25 \mu\text{m}^{-1}$  and  $1.1 \mu\text{m}^{-1}$ . In other InGaN regions including the TJ in this device, the absorption coefficient of  $0.5 \mu\text{m}^{-1}$  is approximated for both wavelength region, and the absorption coefficient of GaN is taken as  $0.017 \mu\text{m}^{-1}$  for both wavelengths [63,70 ].

#### 7.4.1 Optical simulation results for the 470/530 nm dual wavelength LED

The device structure of this dual wavelength LED is programmed using ASAP optical ray tracing software. Two random light emitters are used to simulate dual wavelength emissions from this LED. More than one millions rays are generated, and a split level 2 as shown in Figure 7.12 is activated to trace these split rays at each interface from different LED layers. A detector enclosing this whole LED is used to collected the light emission coming from this LED as depicted in Figure 7.13. Finally, the total light extraction efficiency is calculated based on these results from optical ray tracing. In the simulation, the polarizations of light are averaged. Emission wavelengths are selected from the optical spectrum of the LED as shown in Figure 7.9.

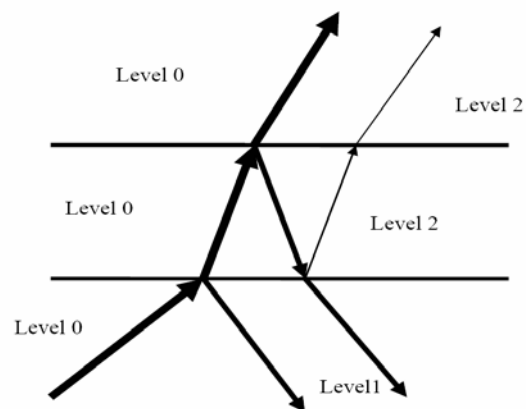


Figure 7.12 Level 2 ray split of optical ray tracing

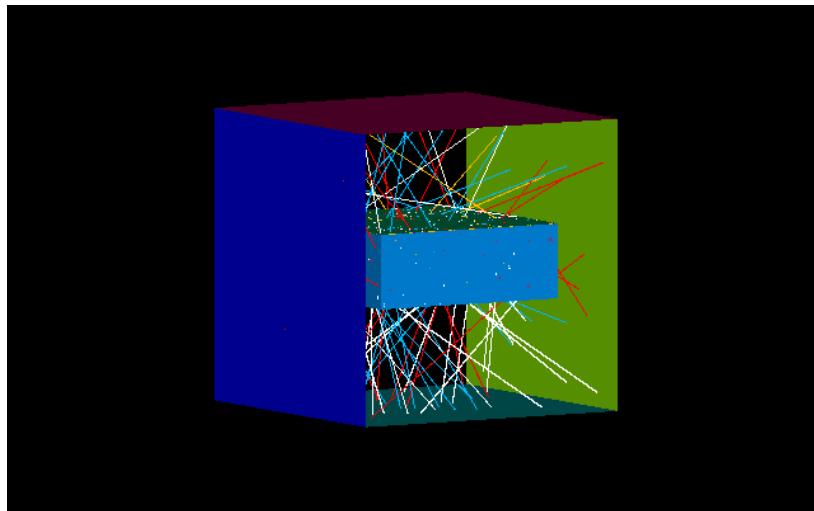


Figure 7.13 Light extraction efficiency collection configuration

A square LED die grown on a  $125\ \mu\text{m}$  thick Sapphire substrate is used in this simulation. The lateral dimension of the bottom LED is  $350\ \text{by}\ 350\ \mu\text{m}$ ; and the bottom LED,  $330\ \text{by}\ 330\ \mu\text{m}$ . The conventional LED package is assumed, i.e., light is mainly emitted in the forward direction. All other parameters of the dual wavelength LED are from Ref. 57, which is detailed in Section 7.1. The die shape irregularity resulting from the die etching for electrical contacts are not considered in this simulation because this part of die only takes a small portion of the entire LED die. Also this irregularity can significantly slow down the ray tracing process. The top LED with a wavelength of  $470\ \text{nm}$  is first simulated. Its total light extraction efficiency is  $5.5\%$ . Figure 7.14 shows the 3-D diagram of the LED, and Figure 7.15 shows a cross section of the LED with some traced rays. Adding a back reflector at the bottom of the substrate does not increase the extraction efficiency of the top LED structure because most of backward emission light is absorbed or trapped into the bottom LED before reaching the substrate. To see how the refractive index and absorption coefficient of the InGaN in an active region affect the

light extraction efficiency, we simulate the extraction efficiency versus index and absorption variation. Results are shown in Figure 7.16 and Figure 7.17. As we can see from these results, refractive index variation by 0.5 can change the light extraction efficiency by about 1%. Since the InGaN refractive index is difficult to be determined at a high accuracy [67], simulations for different refractive index variation is very useful to estimate the total extraction efficiency.

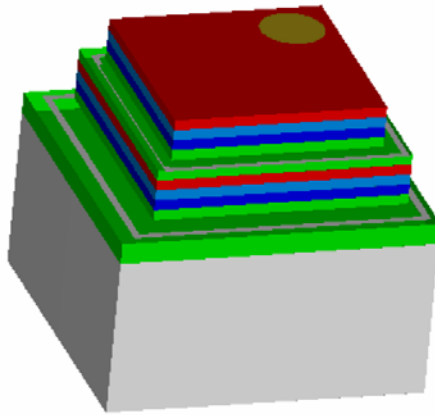


Figure 7.14. 3-D diagram of a dual wavelength LED

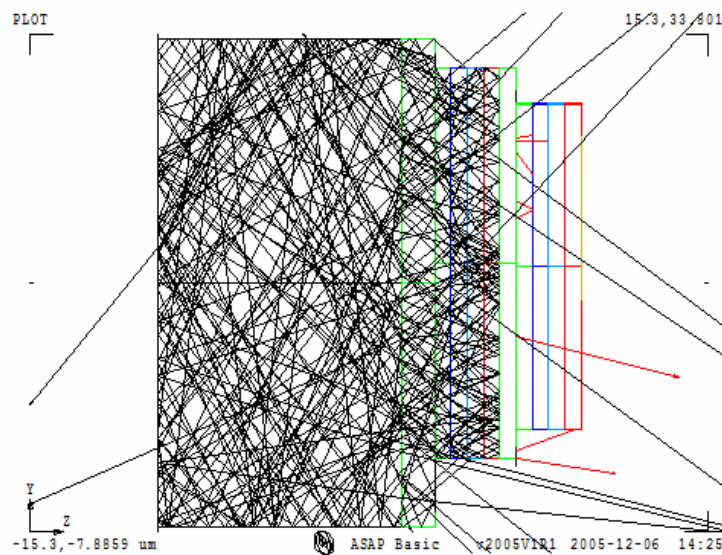


Figure 7.15 2-D plot of ray tracing diagram

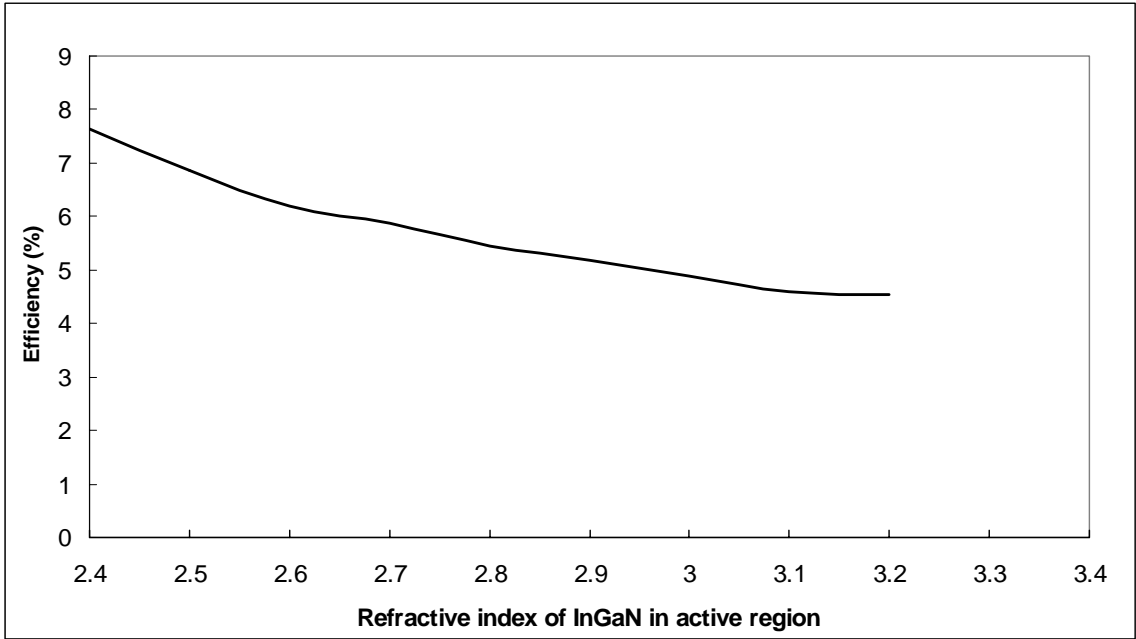


Figure 7.16 Top LED Light extraction efficiency versus the refractive index variation of InGaN active region

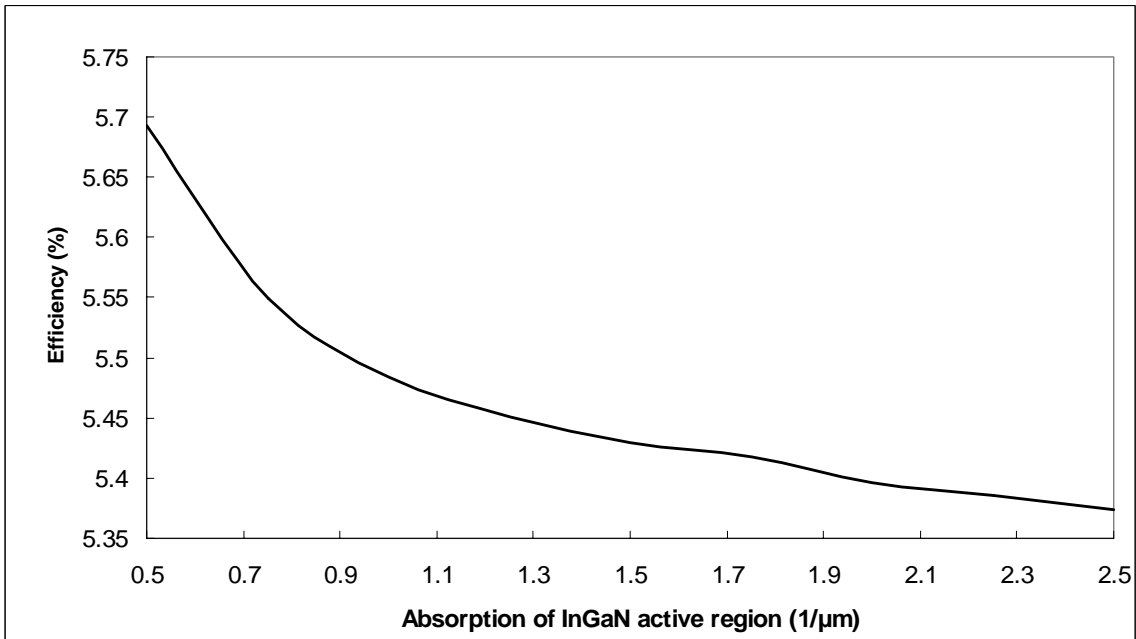


Figure 7.17 Top LED Light extraction efficiency versus the absorption coefficient of InGaN active region

In general, the multilayer LED suture generates micro-cavity interference effects. The incoherent property of geometrical optics prevents ray tracing from taking this interference effects into account. However the reasonable agreement between ray tracing simulation and experimental results for LEDs has been verified [35].

Without detailed simulations for the bottom LED with a peak wavelength of 530 nm, we can estimate its light extraction. Since the bottom LED is sandwiched by the top LED, a TJ and the substrate, the light emissions from this bottom LED will go through two cascaded LED structures before reaching out from the top of this dual wavelength LED. As a result, the light extraction efficiency of the bottom LED is roughly equal to the square of the light extraction efficiency for the top LED. Another reasonable guess can be made about the function of the back reflector. Since the bottom LED is close to the back reflector, it should increase the light extraction efficiency, especially the forward light emission.

All of these reasonable guess about the bottom LED are verified by simulations. The light extraction efficiency of the bottom LED with a back reflector is 0.39%, close to the square of 5.5%, the light extraction efficiency for the top LED with a peak wavelength of 470 nm. The back reflector does increase the light extracted from the top surface of the dual wavelength LED; however, the total light extraction efficiency does not increase so much by adding the back reflector. Most reflected light by the back reflector get absorbed and trapped inside the LED. Similarly, Figure 7.18 shows the light extraction efficiency versus the refractive index of the InGaN active region, and Figure 7.19 for the absorption coefficients variation.

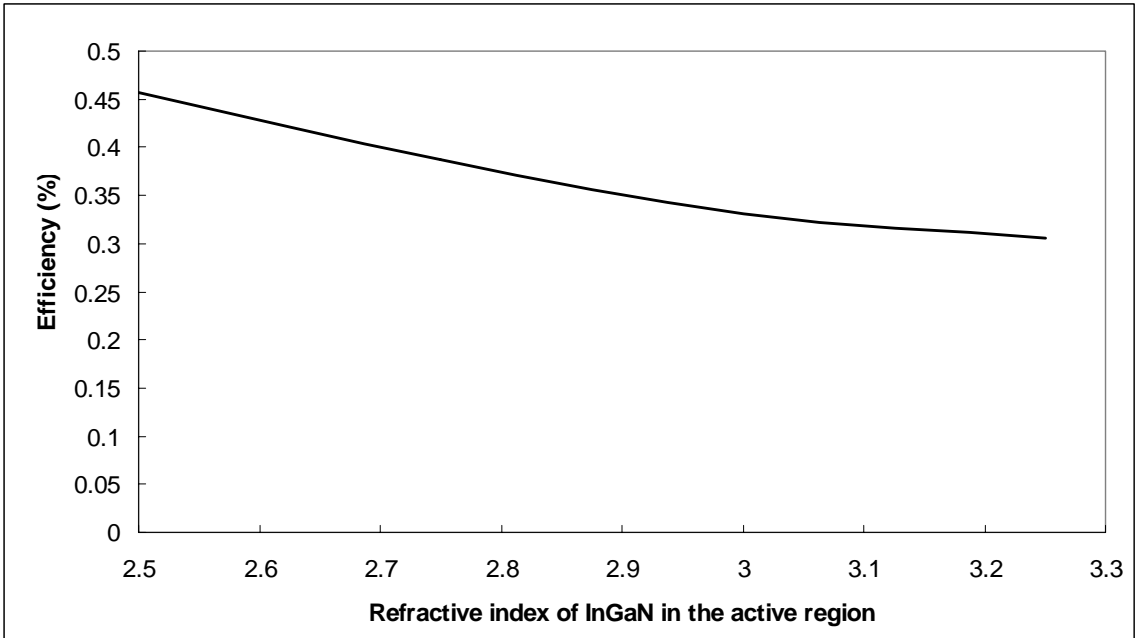


Figure 7.18 Bottom LED Light extraction efficiency versus the refractive index variation of InGaN active region

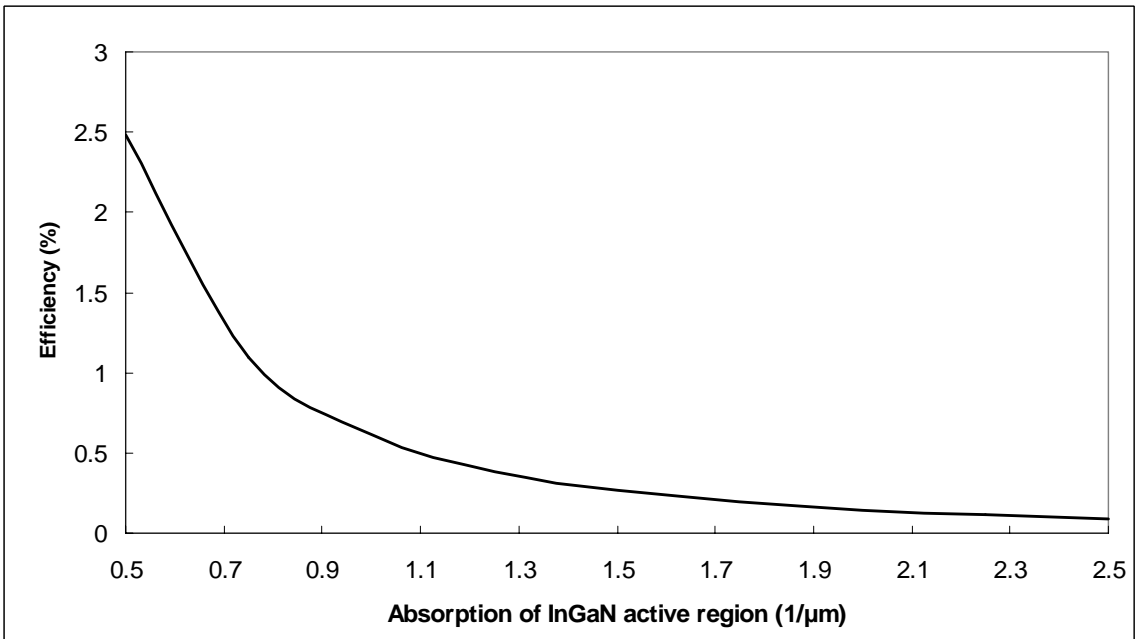


Figure 7.19 Bottom LED Light extraction efficiency versus the absorption coefficient of its InGaN active region

### 7.4.2 Optical simulation results for the 400/460 nm dual wavelength LED

In this dual wavelength LED, a top near UV emitter of 400 nm and a bottom blue emitter of 460 nm are used to efficiently pump the blue and green phosphors. Eq. (7.8) is used to estimate the Indium content in InGaN/GaN MQWs active regions. The  $\text{In}_{0.22}\text{Ga}_{0.78}\text{N}/\text{GaN}$  is used to estimate 460 emissions and  $\text{In}_{0.12}\text{Ga}_{0.88}\text{N}/\text{GaN}$  UV green emissions. Similarly, the optical spectrum is plotted using Eq. (7.9) as shown in Figure 7.20, and the well width is 3nm for both active regions.

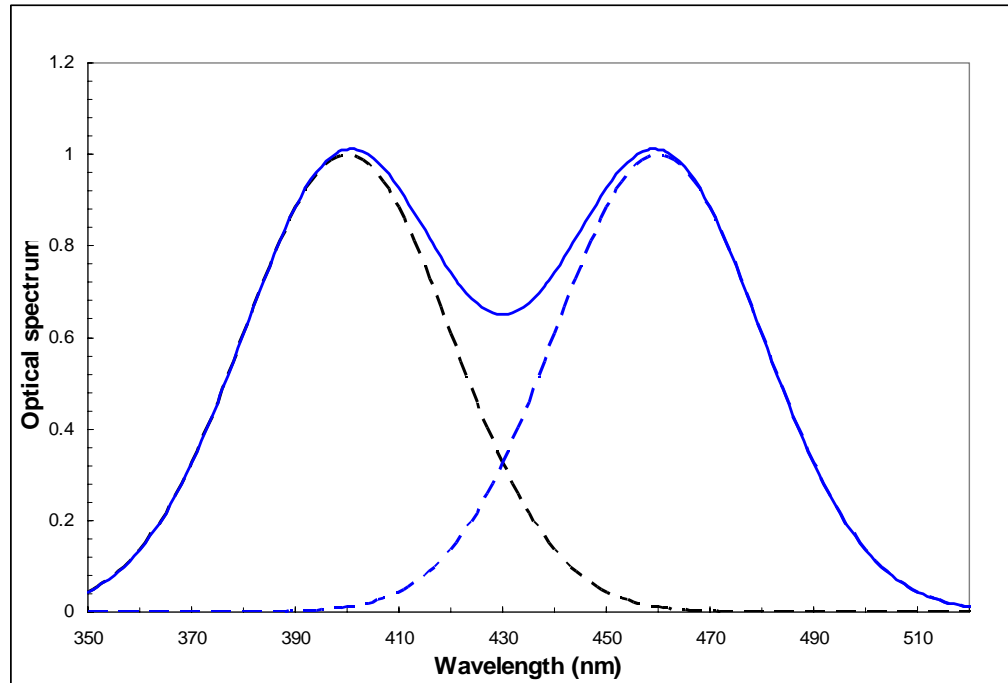


Figure 7.20 Optical spectrum for 400/460 nm emissions

The refractive indices and absorption coefficients for this device simulation are listed in Table 4.

Table 4 Refractive indices and absorption coefficients for optical simulations

	Index @400nm	Absorption @400 nm	Index @ 460 nm	Absorption @ 460 nm
AlGaIn (x=0.07)	2.47	0.017	2.37	0.01
InGaIn (x=0.1)	2.88	0.58	2.55	0.5
GaN	2.54	0.017	2.42	0.017
MQW InGaIn (x=0.12, 400nm )	3.04	0.75	2.58	0.65
MQW InGaIn (x=0.22, 460nm)	3.4	1.44	2.80	1.25

The optical simulation results for the 400/460 nm LED are very similar to those of 470/530 nm in Section 7.4.1. The light extraction efficiency for the top 400 nm emitter is 4.3% and 0.4% for the bottom 460 emitter. The light extraction efficiency versus the refractive index and absorption coefficient of the InGaIn active region follow the similar trend as that of 470/530 nm simulations. Our simulation also shows that adding a reflector between two emitters to reflect 400 nm and transmit 460 nm peak emissions only slightly increase the light extraction efficiency by a fraction of one percent . Because off-normal rays are re-trapped within the LED structure after they are either reflected or transmitted by the reflector inside the LED.

The low light extraction efficiency of the bottom emitter is mainly caused by three more InGaIn layers other than two active regions: one InGaIn layer in the TJ, and two InGaIn layer close to two n-GaN layers in the dual wavelength structure. Our

simulation shows that the light extraction efficiency of the bottom emission reaches 4.5% without absorptions from these extra InGaN layers.

A flip-chip structure is also simulated, and a metal reflector of 80% reflectivity is applied p-GaN layer. The whole LED structure is repositioned with the substrate on the top. A DBR type reflector with 90% reflectivity for 460 nm emissions and 90% transmittance for 400 nm emissions is inserted between 400 nm and 460 nm LEDs. The simulated light extraction efficiencies for 400 nm and 460 nm emissions are 0.97% and 1.09, respectively. Our simulation results show that this flip-chip structure doubles the light extraction efficiency for 460 emissions, which agrees with previous reported results [35]. However, this flip-chip structure reduces the light extraction efficiency of 400 nm emission by four times, and this reduction can be explained that the 400 nm emissions need to pass two cascaded single LED structures with three more InGaN layers in addition to two InGaN MWQs active regions.

## 7.5 Summary

In this chapter, we analyze the device structure of the dual-wavelength LED. The DBRs based on GaN and the refraction indexes of GaN, AlGaN and InGaN have been investigated. The light extraction of this dual-wavelength LED has been simulated using optical ray tracing programs. Two different emission pairs, 400/460nm and 470/530nm are studied. The low light extraction efficiency for the bottom LED presents problem for this dual wavelength LED application to high efficiency lighting application. The back reflector has some effects on the dual wavelength LED. The refractive index variation has a big impact on the light extraction efficiency than the absorption coefficient of the InGaN in the active region. A micro cavity is required to improve the light extraction efficiency of the bottom LED. To design and fabricate this micro-cavity for a dual wavelength LED, new materials with large contrast of refractive index are required to

increase the reflection bandwidth. In general, the reflection bandwidth of a micro-cavity should cover at least 80 nm. Current GaN based III-V materials fail to meet this large reflection bandwidth requirement.

## CHAPTER 8

### CONCLUSIONS AND FUTURE WORK

#### 8.1 Semiconductor Optical Amplifiers and Wavelength Converters

A numerical model of wavelength converters based on cross-gain modulation in semiconductor optical amplifiers is developed. A more accurate gain coefficient model and spatial variations of carrier densities, differential gain, and internal loss across amplifiers are included in this numerical model. To the best of our knowledge, these variations are included in an SOA wavelength converter model for the first time. This is the first time a steady state numerical model with analytic gain coefficients is used to model and identify some unique features and different performances for up-converters and down-converters with short SOAs and long SOAs. The different performances of an up-converter and a down converter of long and short SOA wavelength converters are investigated using our model. Moreover, each physical variable in this model, such as the carrier density, gain coefficient, differential gain, and internal loss, varies within the cavity of the SOA. In the simulated examples, there is about a 3-dB converter efficiency degradation, about a 6 GHz modulation bandwidth increase for the long SOA wavelength up-converter; however, the performance of an up-converter and a down-converter is almost identical for the short SOA wavelength converter. This equal performance feature of the up-converter and down converter using a short SOA is one of the critical factors to evaluate wavelength converters. A long SOA wavelength converter does not have such features even though it can offer large bandwidth. This is the trade-off between the modulation bandwidth and the equal performance of an up-converter and a down-converter. The following results are achieved based on this research works.

- 1) A comprehensive numerical solution to solve SOAs and SOA-based wavelength conversions using FDM is implemented. The carrier density is dynamically adjusted to achieve a stable solution using a convergent factor to monitor coupled differential equations for photons and carrier transportations.

2) A more accurate gain coefficient model and spatial variations of carrier densities, differential gain, and internal loss across amplifiers are incorporated in this numerical model. Differential gains, material loss, and other physical parameters of SOAs are all numerically solved.

3) Detailed large signal and small signal performance for up- and down-conversion of long and short SOAs is simulated. Performance trade-offs between the modulation bandwidth and the equal performance of an up-converter and a down-converter are analyzed. This model can be used to optimize SOA-based wavelength conversions by selecting proper cavity length to meet system requirements on bandwidth and equal performance for up- and down-conversions. This numerical model is experimentally verified.

## **8.2 High Brightness LED and Solid State Lighting**

The light extraction efficiency is one of the critical factors in the design and manufacture of LEDs. The LED die structure and geometry strongly influence its lighting extraction efficiency. The major hurdle in increasing the light extraction efficiency is the total internal reflection (TIR) of light between different materials, which traps a lot of photons inside LED chips, and the high refractive index of most semiconductor materials makes TIR even stronger. As a result, most of LEDs fail to deliver enough light to compete with conventional lightings. The main accomplishments of this research for LEDs and solid state lighting are as follows.

- 1) Light extraction efficiency is increased by increase the thickness of a substrate. The light undergoes more ‘loss’ when propagating at a longer distance, and the lost light is leakage light that escapes from the LED sidewalls. This is proved by optical modeling and optical experiments. A back reflector at the bottom of a substrate folds back the light path and equivalently doubles the effective thickness

of the substrate. The application of a back reflector increases the light extraction accordingly.

- 2) The back reflector is replaced with a reflection grating . Although a back reflector can fold the optical path, the reflected light re-enters the LED die regions, and undergo re-absorptions. To overcome this problem, we proposed a new method, where a reflection /blazed grating is used to shift the major portion of the light into high orders of diffraction, and most light will be escape from sidewalls of LEDs without re-entering the LED regions with absorptions. The reflection grating can be either an amplitude grating or a phase grating, and can be integrated and fabricated in the LEDs manufacturing process.
- 3) The light extraction efficiency can be further improved by altering the geometry of LED structures. We proposed and implemented a rhombus die shape to increase the lighting efficiency . This change of waveguide structure will increase the amount of leakage modes of light so that more light will come out of the LED sidewalls, which significantly reduces the absorption of light inside the LED. The LED die can be modeled as a three-dimensional waveguide. It can be further decomposed into two infinite slab waveguides in the x and y directions, and we use slab waveguide theory to model this 3-D waveguide without applying complicated 3-D wave guide theory. It has been shown that the number of guided modes that the slab waveguide can support is proportional to  $d$ , the confined dimension of the waveguide. For the same die area, the confined dimension of the rhombus die,  $h = d (\sin\theta)^{0.5}$  . This reduced dimension of the rhombus waveguide will decrease the number of guided modes and consequently increase the number of leakage modes. We also can show that, for the same die area, the total sidewall area of a rhombic die is  $1/(\sin\theta)^{0.5}$  times that of a square die. Compared to a regular LED die shape, a rhombus die has a relatively large area of sidewalls. As a result, more light can come out of the sidewalls for a rhombus-shaped die. This is also confirmed by our optical simulation and experimental results.

- 4) A dual-wavelength LED with so called fuzzy Bragg grating is proposed to provide a broad band pump source for phosphors; it can also be used in other applications such as display and bio-sensing. In this dual-wavelength LED structure, two electrical independent InGaN quantum-wells with different indium compositions are grown in a single vertical heterostructure; a p<sup>++</sup>/n<sup>++</sup> GaN tunnel junction is sandwiched between the two InGaN quantum-well active regions to make it a three-terminal device. These different indium compositions correspond to two different emission wavelengths, such as near UV (370-400 nm), or green emission (505-525 nm). We analyzed the device structure of this dual-wavelength LED. The DBRs based on GaN along with refraction index of GaN, AlGaIn and InGaIn have been investigated. The light extraction of this dual-wavelength LED has been given using optical ray tracing programs.

### **8.3 Future Work and New Trends**

To further improve accuracy of optical modeling for SOAs, temperature effect on SOA gain coefficient models needs to be addressed. The rigorously modeling of amplified spontaneous emissions (ASE) still presents challenges, and it is also an open topic with some unsolved theoretical issues. More accurate models for ASE should be developed.

As for LEDs, especially a dual-wavelength LED, new materials with refractive index contrast for broad reflection band are required to design a micro-cavity for this dual-wavelength LEDs. Detailed numerical modeling and experimental verification of refractive index of InGaIn and AlGaIn both bulk material and quantum well type application are important to LEDs modeling. Photon recycling and scattering effects from surface roughness and die shape irregularity resulting from die etching are also important issues to be addressed. Detailed analysis of reflection grating effects on the light extraction efficiency based on the rigorous coupled-wave analysis (RCWA) in another important issue in the optical modeling of LEDs. Other types of LED device structure to

reduce the number of InGaN layers and alternative LED packaging methods, such as flip-chip and substrate removal are critical to improve the light efficiency of LED and solid state lighting.

#### 8.4. Publications and Patents Based on This Research Work

There are four publications on SOAs, and two publications and four issued and pending patents on LEDs:

1. Dong-Xue Wang, John A. Buck, Kevin Brennan and Ian T Ferguson, "A numerical model of wavelength converters based on cross-gain modulation in semiconductor optical amplifiers," *Optical Engineering*. Vol. 45, pp. 024203-1,4, Feb. 2006.
2. Dong-Xue Wang, John A. Buck, Kevin Brennan and Ian T Ferguson, "Numerical simulation of semiconductor optical amplifiers based wavelength converters," *Proc. of SPIE*, vol. 6014, pp. 60140Y1-4, Oct. 2005.
3. Dong-Xue Wang, John A. Buck, Kevin Brennan and Ian T Ferguson, "Small signal analysis of wavelength converters based on cross-gain modulation in semiconductor optical amplifiers" Technical digest, *Frontiers in Optics 2005/Laser science XXI* (Optical Society of America, Washington, DC, 2005) FWH2
4. Dong-Xue Wang, John A. Buck, Kevin Brennan and Ian T Ferguson, "Numerical model of wavelength conversion through cross-gain modulation in semiconductor optical amplifiers," *Applied Optics* (To be published)
5. Dong-Xue Wang, Ian T. Ferguson and John A. Buck, "Optical design and simulation for dual-wavelength LEDs in solid state lighting," *CLEO* (OSA and IEEE) Long Beach, CA. May 2006 (To be published)
6. Dong-Xue Wang, Ian T. Ferguson and John A. Buck, "Optical design and simulation for nano-scale distributed Bragg reflector for high brightness LED," *SPIE Optics & Photonics*, San Deigo, CA Aug. 2006 (To be published)
7. Dong-Xue (Michael) Wang and H. Venugopalan, US patent 6,903,379 B2
8. Dong-Xue (Michael) Wang and H. Venugopalan. International patent application Application No. WO 02/053107)
9. I Eliashevich and Dong-Xue (Michael) Wang, US patent application (Application No.

10/399,635)

10. I. Eliashevich and Dong-Xue (Michael) Wang. International patent application  
(Application No. WO 02/063348)

## REFERENCES

- [1] G. Agrawal, *Fiber –optic Communication Systems*, 2<sup>nd</sup> Edition. New York, NY, Wiley, 1997.
- [2] A. Mecozzi and J. Wiesenfeld, “The roles of semiconductor optical amplifiers in optical networks,” *Opt. & Photon. News*. Vol.12, pp.36-42, Mar. 2001.
- [3] P. Becker, N. Olsson and J. Simpson, *Erbium-Doped Fiber Amplifiers*, San Diego, CA, Academic Press, 1999.
- [4] S. Namiki and Y. Emori, “Ultrabroad-band Raman amplifies pumped and gain equalized By WDM high power laser diode,” *IEEE J. on selected topics in Quantum Electron.*, vol. 7, pp. 3-16, Jan/Feb. 2001.
- [5] L. Spiekman, “8x10 Gb/s DWDM transmission over 240km of standard fiber using a cascade of semiconductor optical amplifiers,” *IEEE Photon. Technol. Lett.*, vol. 12, pp. 1082-1084, Aug. 2000.
- [6] Y. Chen, “Optimizations of operating conditions of semiconductor optical amplifier for single wavelength and WDM applications.” *WWW.JDSU.com*. Access date Oct. 2005
- [7] Y. Sun *et al.* , “ Error-free transmission of 32x2.5 Gbit/s DWDM channels over 125 km using cascaded in-line semiconductor optical amplifiers,” *Electron. Lett.* vol. 35, pp.1863-1865, Oct. 1999.
- [8] H. Kim and S. Chandrasekhar, “Reduction of cross-gain modulation in the semiconductor amplifier by using wavelength modulated signal,” *IEEE Photon. Technol. Lett.*, vol. 12, pp. 1412-1414, Oct. 2000.
- [9] A. Ellis, D. Davies, A. Kelly and W. Pender, “Data driven operation of semiconductor optical amplifier loop mirror at 40Gbits/s,” *Electron. Lett.*, vol.31, pp. 1245-1247, 1995
- [10] B. Li, X. Chu and K. Shoraby, “ Routing and wavelength assignment vs. wavelength converter placement in all-optical networks,” *IEEE opt. comm.* pp.522-528, Aug. 2003
- [11] D. Marcuse, “Computer Model of an injection laser amplifier,” *IEEE J. Quantum Electron.*, vol. 19, pp. 63-73, Jan. 1983.
- [12] K. Obermann, S. Kindt, D. Breuer and K. Petermann, “Performance analysis of wavelength converters based on cross-gain modulation in semiconductor optical amplifiers,” *J. of Lightwave Technol.*, vol. 16, pp. 78-85, 1998.

- [13] M. O'Mahony, "Semiconductor laser optical amplifiers for use in future fiber systems," *J. of Lightwave Technol.*, vol. 6, pp. 531-544, Apr. 1988.
- [14] D. Davis, "Small-signal analysis of wavelength conversion in semiconductor laser amplifiers via gain saturation," *IEEE Photon. Technol. Lett.*, vol. 7, pp. 617-619, June, 1995.
- [15] Antonio Mecozzi, "Small-signal theory of wavelength converters based on cross gain modulation in semiconductor optical amplifiers," *IEEE Photon. Technol. Lett.*, vol. 8, pp. 1471-1473, Nov., 1996.
- [16] M. Nielsen, D. Blumenthal and J. Mørk, "A transfer function approach to the small signal response of saturated semiconductor optical amplifiers," *J. of Lightwave Technol.*, vol. 18, pp. 2151-2156, Dec. 2000.
- [17] T. Duruhuus, B. Mikkelsen, C. Joergensen, S. Danielsen, and K. Stubkjaer, "All optical wavelength conversion by semiconductor optical amplifiers," *J. of Lightwave Technol.*, vol. 14, pp. 942-954, June 1996.
- [18] T. Duruhuus, B. Mikkelsen and K. Stubkjaer, "Detailed dynamic model for semiconductor optical amplifier and their crosstalk and intermodulation distortion," *J. of Lightwave Technol.*, vol. 10, pp. 1056-1064, Aug. 1992.
- [19] I. Valiente, J. Simon, and M. Ligne, "Theoretical analysis of semiconductor optical amplifier wavelength shifter," *Electron. Lett.*, vol. 29, pp.502-503, March 1993.
- [20] D. Lürßen, R. Ram, A. Hohl-AbiChedid, E. Claucen Jr. and J. Hudings, "Thermal profiling: locating the onset of gain saturation in semiconductor optical amplifiers," *IEEE Photon. Technol. Lett.*, vol. 16, pp. 1625-1627, Jul., 2004.
- [21] T. Lee, C. Burrus, J. Copeland, A. Dentai and D. Marcuse, "Short-cavity InGaAsP injection lasers: Dependence of mode spectra and single-longitudinal-mode power on cavity length," *IEEE J. Quantum Electron.*, vol. QE-18 p.1101, Jul. 1982.
- [22] M. Adams, J. Collins and I. Henning, "Analysis of semiconductor laser optical amplifiers," *IEE Proc.* vol. 132, pp.58-63. Feb. 1985.
- [23] J. Simon, "Semiconductor laser amplifier for single mode optical fiber communications," *J. Opt. Comm.* Vol. 4. pp. 51-62, 1983.
- [24] L. Gillner, "Comparative study of some traveling-wave semiconductor laser amplifier models," *IEE Proc.* vol. 139, pp.339-347. Oct.. 1992.
- [25] M. Connelly, "Wideband semiconductor optical amplifier steady-state numerical model," *IEEE J. Quantum Electron.*, vol. 37, pp. 439-447, Mar. 2001.

- [26] P. Bhattacharya, *Semiconductor Optoelectronic Devices*. 2<sup>nd</sup> Edition, Upper Saddle River, NJ, Prentice Hall, 1997.
- [27] D. Marcuse, *Principles of Quantum Electronics*. New York, Academic, 1980
- [28] J. Simon, P. Doussiere, L. Pophillat and B. Fernier, "Gain and noise characteristics of a 1.5  $\mu\text{m}$  near-traveling-wave semiconductor laser amplifier," *Electron. Lett.*, vol. 25, pp. 434-436, 1989
- [29] J. Wiesenfeld, B. Glance, J. Perino and A. Gnauk, "Wavelength conversion at 10Gb/s using a semiconductor optical amplifier," *IEEE Photon. Tech. Lett.* vol.5, pp.1300-1303, 1993.
- [30] A. Ellis, A. Kelly, D. Nasset, D. Pitcher, D. Moodie and R. Kashyap, "Error free 100 Gbit/s wavelength conversion using grating assisted cross-gain modulation in a 2mm long semiconductor amplifier," *Electron. Lett.*, vol. 34, pp. 1958-1959, 1998.
- [31] A. Yariv, *Opt Electron*. New York, HWR International, 1985.
- [32] G. Agrawal and I. Habbab, "Effect of four-wave mixing on multichannel amplification in semiconductor laser amplifiers," *IEEE J. Quantum Electron.*, vol. 25, pp. 501-505, 1990.
- [33] K-H Lee, K-H Park and W.-Y. Choi, "Measurement of the carrier lifetime and linewidth enhancement factor of semiconductor optical amplifiers using their optical modulation responses," *Opt. Eng.*, vol. 43, pp. 2715-2718, 2004.
- [34] P. Doussiere, P. Garabedian, C Graver, D. Bonnevie, T. Fillion, E. Derouin, M. Monnot, J. Provost, D. Leclere, and M. Klenk, "1.55  $\mu\text{m}$  polarization independent semiconductor optical amplifier with 25 dB fiber-to-fiber gain," *IEEE Photon Technol. Lett.*, vol 6, pp. 170-172, 1994.
- [35] D. Streigerwald, J. Bhat, D. Collins, R. Fletcher, M. Holcomb, M. Ludowise, P. Martin and S. rudaz, "Illumination with solid state lighting technology," *IEEE J. on Selected Topics in Quantum Electron.*, vol. 8, pp. 310-320, April 2002.
- [36] R. Muller-Mach, G. Mueller, M. krames and T. Trottier, "High-power phosphor converted Light-Emitting Diodes based on III-Nitrides," *IEEE J. on Selected Topics in Quantum Electron.*, vol. 8, pp. 339-345, April 2002.
- [37] J. Han and A. Nurmikko, "Advances in AlGaInN blue and ultraviolet light emitters," *IEEE J. on Selected Topics in Quantum Electron.*, vol. 8, pp. 289-297, April 2002.
- [38] T. Mukai, "Recent progress in group-III Nitride Light-Emitting Diodes," *IEEE J. on Selected Topics in Quantum Electron.*, vol. 8, pp. 264-270, April 2002.

- [39] S. Nakamura, M. Fasol, *The blue laser diode-GaN based light emitters and lasers*, Berlin, Springer, 1997.
- [40] I. Ferguson, M. Schurman and I. Eliashevich, "Recent developments in the growth of GaN-based compound semiconductors," *J. of the Korean Phys. Soc.*, vol. 39, pp. S433-S441, Dec. 2001.
- [41] S. Lukacs, F. Long, C. Tran and I. Ferguson, "Investigation of disorder in InGaN light-emitting diodes," *Proc. SPIE*, vol. 3938, pp. 105-112, Jan. 2000.
- [42] X. Cao and S. Arthur, "High-power and reliable operation of vertical Lighting Emitting diodes on bulk GaN," *Appl. Phys. Letts.*, vol. 85, pp. 3971-3973, Nov. 2004.
- [43] P. Royo, R. Stanley and M. Ilegems, "Analytical calculation of the extraction efficiency of microcavity Light-Emitting Diodes for display and fiber coupling applications," *IEEE J. on Selected Topics in Quantum Electron.*, vol. 8, pp. 207-218, April 2002.
- [44] R. Windisch, C. Rومان, B. Dutta, A. Knobloch, G. Borghs, G. Dohler and P. Heremans, "Light-extraction mechanisms in high-efficiency surface-textured Light-Emitting Diodes," *IEEE J. on Selected Topics in Quantum Electron.*, vol. 8, pp. 248-255, April 2002.
- [45] J. Goodman, *Introduction to Fourier optics*, 2<sup>nd</sup> Edition, New York, McGraw-Hill, 1996.
- [46] W. Smith, *Modern Optical Engineering*, 2nd edition, New York, McGraw-Hill, 1990.
- [47] J. Loomis, *Optical design lecture note*, University of Dayton, Dayton, OH 1995.
- [48] J. Stover, *Optical Scattering: Measurement and analysis*, 2<sup>nd</sup> edition, Washington SPIE, 1995.
- [49] Breault research Org. Inc. Scattering, *ASAP technical guide*, Tucson AZ, 2004.
- [50] H. Benisty, R. Stanley, and M. Mayer, "Method of source terms for dipole emission modification in modes of arbitrary planar structures," *J. Opt. Soc. Am A*, vol 15, pp. 1192-1201, May 1998.
- [51]. P. Yeh, *Optical waves in layered media*. New York, Wiley, 1988.
- [52]. F. Pedrotti, L. Pedrotti, *Introduction to Optics*, New Jersey, Prentice-Hall, 1993.

- [53] K. Okamoto, *Fundamentals of optical waveguides*. San Diego, CA, Academic Press. 2000.
- [54] D. Wang, H. Venugopalan. US patent 6,903,379.
- [55] S. Lee, "Analysis of InGaN high brightness light-emitting diodes," *Jpn. J. Appl. Phys.*, vol. 37, pp. 5990-5993, Nov. 1998.
- [56] I. Ferguson, US patent 6,366,018.
- [57] I. Ferguson, US patent 6,404,125.
- [58] I. Ozden, E. Makarona and A. Nurmikko, "A dual-wavelength indium gallium nitride quantum well light emitting diode," *Appl. Phys. Letts.*, vol. 79, pp. 2532-2534, Oct. 2001.
- [59] K. Brennan, *The physics of semiconductors*, New York, Cambridge press, 1999.
- [60] J. Piprek, *Semiconductor Optoelectronic Devices, Introduction to physics and simulation*. San Diego, CA, Academic Press, 2003.
- [61] S. Jeon, Y. Song, H. Jang, G. Yang, S. Hwang and S. Son "Lateral current spreading in GaN-based light-emitting diodes utilizing tunnel contact junctions," *Appl. Phys. Letts.*, vol. 78, pp. 3265-3267, May 2001.
- [62] M. Diage, Y. He, H. Zhou, E. Makarona, A. Nurmikko, J. Han, K. Waldrip, J. Figiel, T. Takeuchi and M. Krames "Vertical violet light emitting diode incorporating an aluminum gallium nitride distributed Bragg mirror and a tunnel junction," *Appl. Phys. Letts.*, vol. 79, pp. 3720-3722, Nov. 2001.
- [63] H. Ng, T. Moustakas, S. Chu, "High reflectivity and bandwidth AlN/GaN distributed Bragg reflectors grown by molecular-beam epitaxy," *Appl. Phys. Letts.*, vol. 76, pp. 2818-2820, May 2000.
- [64] N. Nakada, M. Nakaji, H. Ishikawa, T. Egawa, M. Umeno and T. Jimbo, "Improved characteristics of InGaN multiple-quantum-well light-emitting diode by GaN/AlGaIn distributed Bragg reflector grown on sapphire," *Appl. Phys. Letts.*, vol. 76, pp. 1804-1806, Apr. 2000.
- [65] T. Someya and Y. Arakawa, "Highly reflective GaN/Al<sub>0.34</sub>Ga<sub>0.66</sub>N quarter-wave reflectors grown by metal organic chemical vapor deposition," *Appl. Phys. Letts.* vol. 73, pp. 3653-3655, Dec. 1998.
- [66] R. Langer, A. Barski, J. Simon, N. Pelekanos, O. Konovalov, R. Andre and L. Dang, "High-reflectivity GaN/GaAlN Bragg mirrors at blue/green wavelengths grown by molecular beam epitaxy," *Appl. Phys. Letts.*, vol. 74, pp. 3610-3612, June. 1999.

- [67] D. Brunner, H. Angerer, E. Bustarret, F. Freudenberg, R. Hopler, R. Dimitrov, O. Ambacher and M. Stutzmann, "Optical constants of epitaxial AlGa<sub>x</sub>N films and their temperature dependence," *J. Appl. Phys.*, vol. 82, pp. 5090-5096, Nov. 1997.
- [68] G. Laws, E. Larkins and I. Harrison, "Improved refractive index formulas for the Al<sub>x</sub>Ga<sub>1-x</sub>N and In<sub>y</sub>Ga<sub>1-y</sub>N alloys," *J. Appl. Phys.*, vol. 89, pp. 1108-1115, Jan. 2001.
- [69] A. Adachi, *Physical properties of III-V semiconductor compounds*, New York, Wiley, 1992.
- [70] T. Peng and J. Piprek, "Refractive index of AlGaInN alloys," *Electron Lett.*, vol 32, pp.2285-2286, Nov. 1996.
- [71] M. Leung, A. Djuricic and E. Li, "Refractive index of InGa<sub>x</sub>N/GaN quantum well," *J. Appl. Phys.*, vol. 84, pp. 6312-6317, Dec. 1998.